Star Formation

Kohji Tomisaka
National Astronomical Observatory Japan

version 0.5: August 5, 2001
version 1.0: August 30, 2001

Contents

1 Introduction **3**
- 1.1 Interstellar Matter . . . 3
- 1.2 Case Study — Taurus Molecular Clouds . . . 4
- 1.3 T-Tauri Stars . . . 6
- 1.4 Spectral Energy Distribution . . . 6
- 1.5 Protostars . . . 10
  - 1.5.1 B335 . . . 10
  - 1.5.2 L1551 IRS 5 . . . 14
- 1.6 L 1544: Pre-protostellar Cores . . . 17
- 1.7 Magnetic Fields . . . 17
  - 1.7.1 Cores with Protostars . . . 21
- 1.8 Density Distribution . . . 22
- 1.9 Mass Spectrum . . . 25

2 Physical Background **27**
- 2.1 Basic Equations of Hydrodynamics . . . 27
- 2.2 The Poisson Equation of the Self-Gravity . . . 27
- 2.3 Free-fall Time . . . 28
  - 2.3.1 Accretion Rate . . . 30
- 2.4 Gravitational Instability . . . 31
  - 2.4.1 Sound Wave . . . 32
- 2.5 Jeans Instability . . . 32
- 2.6 Gravitational Instability of Thin Disk . . . 34
- 2.7 Super- and Subsonic Flow . . . 35
  - 2.7.1 Flow in the Laval Nozzle . . . 35
  - 2.7.2 Steady State Flow under an Influence of External Fields . . . 36
  - 2.7.3 Stellar Wind — Parker Wind Theory . . . 38

3 Galactic Scale Star Formation **43**
- 3.1 Schmidt Law . . . 43
  - 3.1.1 Global Star Formation . . . 43
  - 3.1.2 Local Star Formation Rate . . . 44
- 3.2 Gravitational Instability of Rotating Thin Disk . . . 45
  - 3.2.1 Tightly Wound Spirals . . . 47
  - 3.2.2 Toomre's Q Value . . . 48
- 3.3 Spiral Structure . . . 49
- 3.4 Density Wave Theory . . . 50

3.5 Galactic Shock 53

4 Local Star Formation Process **59**
4.1 Hydrostatic Balance 59
4.1.1 Bonnor-Ebert Mass 60
4.1.2 Equilibria of Cylindrical Cloud 60
4.2 Virial Analysis 61
4.2.1 Magnatohydrostatic Clouds 62
4.3 Evolution of Cloud/Cloud Cores 64
4.3.1 Subcritical Cloud vs Supercritical Cloud 64
4.3.2 Protostellar Evolution of Supercritical Clouds 69
4.4 Accretion Rate 70

A Basic Equation of Fluid Dynamics **75**
A.1 What is fluid? 75
A.2 Equation of Motion 75
A.3 Lagrangian and Euler Equation 75
A.4 Continuity Equation 76
A.5 Energy Equation 77
A.5.1 Polytropic Relation 77
A.5.2 Energy Equation from the First Law of Theromodynamics 77
A.6 Shock Wave 78
A.6.1 Rankine-Hugoniot Relation 78

Chapter 1

Introduction

1.1 Interstellar Matter

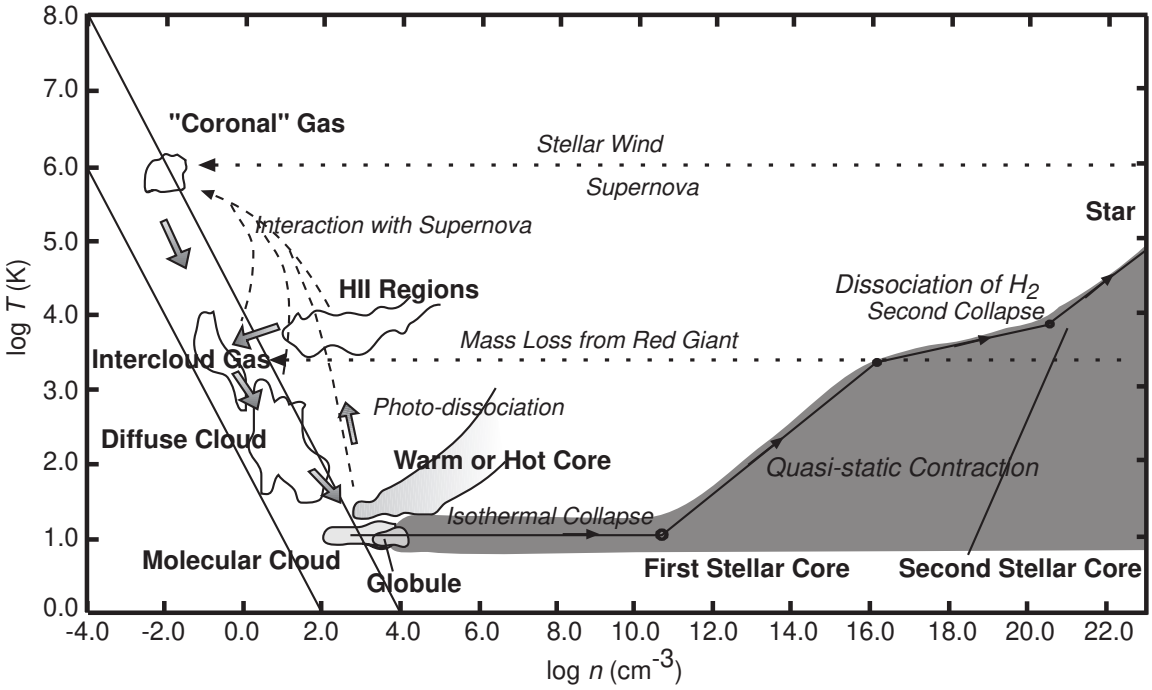

Figure 1.1: Multiphases of the interstellar medium. The temperature and number density of gaseous objects in the interstellar medium are summarized. Originally made by Myers (1978), reconstructed by Saigo (2000).

Figure 1.1 shows the temperature and number density of gaseous objects in our Galaxy. Cold interstellar medium forms molecular clouds ($T \sim 10$K) and diffuse clouds ($T \sim 100$K). Warm interstellar medium $10^3\mathrm{K} \lesssim T \lesssim 10^4\mathrm{K}$ are thought to be pervasive (wide-spread). HII regions are ionized by the Ly continuum photons from the early-type stars. There are coronal (hot but tenuous) gases with $T \sim 10^6$ K in the Galaxy, which are heated by the shock fronts of supernova remnants. Pressures of these gases are in the range of $10^2\mathrm{K\,cm^{-3}} \lesssim p \lesssim 10^4\mathrm{K\,cm^{-3}}$, except for the HII regions. This may suggest that the gases are in a pressure equilibrium.

In this figure, a theoretical path from the molecular cloud core to the star is also shown. We will see the evolution more closely in Chapter 4.

Globally, the molecular form of Hydrogen is much abundant inside the Solar circle, while the atomic hydrogen is more abundant than molecular H_2 in the outer galaxy. In Figure 1.2 (left), the radial distributions of molecular and atomic gas are shown. The right panel shows the distributions for four typical external galaxies (M51, M101, NGC6946, and IC342). This indicates these distributions are similar with each other. HI is distributed uniformly, while H_2 density increases greatly reaching the galaxy center. In other words, only in the region where the total (HI+H_2) density exceeds some critical value, H_2 molecules are distributed.

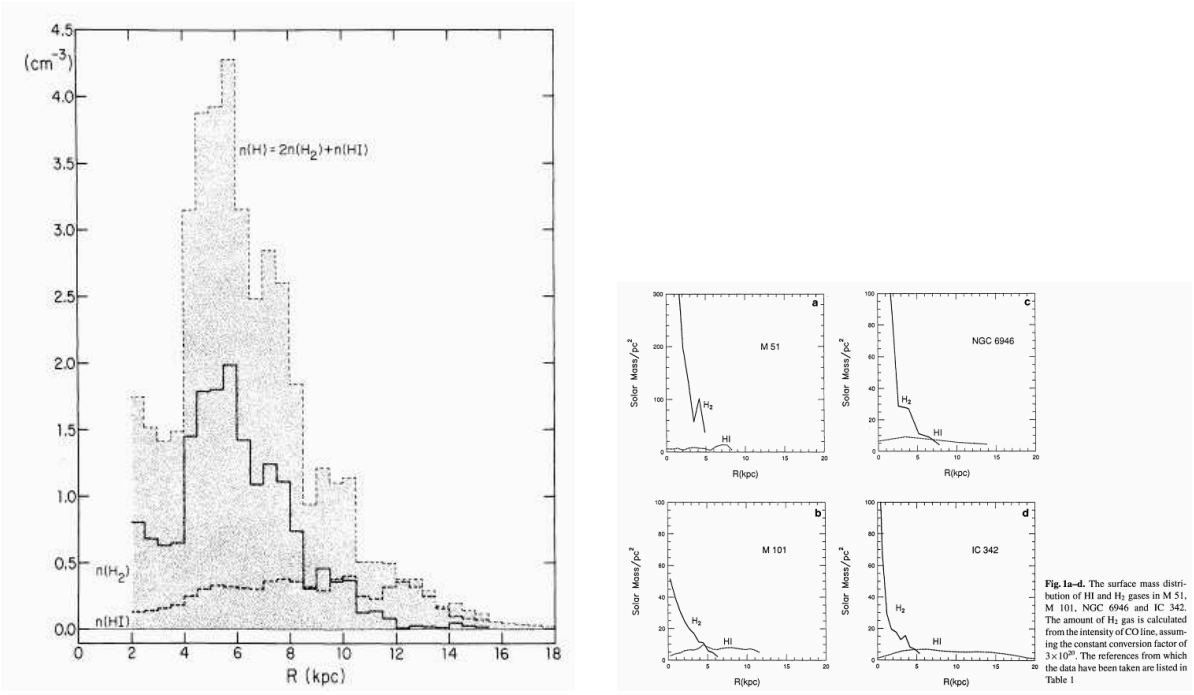

Figure 1.2: Radial distribution of H_2 and HI gas density. (Left:) our galaxy. Converting from CO antenna temperature to H_2 column deity, $n(\mathrm{CO})/n(\mathrm{H_2}) = 6 \times 10^{-5}$ is assumed. Taken from Gordon & Burton (1976). (Right:) Radial distribution of H_2 and HI gas for external galaxies. The conversion factor is assumed constant $X(\mathrm{H_2/CO}) = 3 \times 10^{20} \mathrm{H_2/K\,km\,s^{-1}}$. Taken from Honma et al (1995).

1.2 Case Study — Taurus Molecular Clouds

Figure 1.3 (left) shows the ^{13}CO total column density map of the Taurus molecular cloud (Mizuno et al 1995) whose distance is 140 pc far from the Sun. Since ^{13}CO contains ^{13}C, a rare isotope of C, the abundance of ^{13}CO is much smaller than that of ^{12}CO. Owing to the low abundance, the emission lines of ^{13}CO are relatively optically thiner than that of ^{12}CO. Using ^{13}CO line, we can see deep inside of the molecular cloud. The distributions of T-Tauri stars and ^{13}CO column density coincide with each other. Since T-Tauri stars are young pre-main-sequence stars with $M \sim 1M_\odot$, which are in the Kelvin contraction stage and do not reach the main sequence Hydrogen burning stage, it is shown that stars are newly formed in molecular clouds.

Since ^{18}O is much more rare isotope (^{18}O/^{16}O $\ll^{13}$ C/^{12}C), the distribution of much higher-

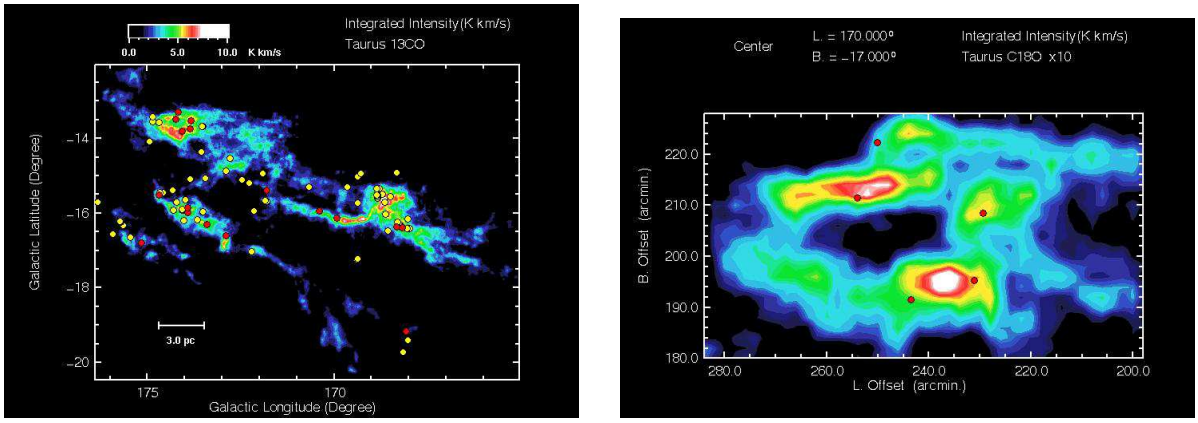

Figure 1.3: (*Left*) ^{13}CO total column density map of the Taurus molecular cloud (Mizuno et al 1995). Taken from their home page with a url of http://www.a.phys.nagoya-u.ac.jp/nanten/taurus.html (in Japanese). T Tauri stars, which are thought to be pre-main-sequence stars in the Kelvin contraction stage, are indicated by bright spots. (*Right*) C^{18}O map of Heiles cloud 2 region in the Taurus molecular cloud (Onishi et al. 1996). This shows clearly that the cloud is composed of a number of high-density regions.

density gases is explored using C^{18}O lines. Figure 1.3 (right) shows C^{18}O map of Heiles cloud 2 in the Taurus molecular cloud by Onishi et al (1996). This shows us that there are many molecular cloud cores which have much higher density than the average. Many of these molecular cloud cores are associated with IRAS sources and T-Tauri stars. It is shown that star formation occurs in the molecular cloud cores in the molecular cloud. They found 40 such cores in the Taurus molecular cloud. Typical size of the core is ~ 0.1 pc and the average density of the core is as large as $\sim 10^4 \mathrm{cm}^{-3}$. The mass of the C^{18}O cores is estimated as $\sim 1 - 80 M_\odot$.

H^{13}CO$^+$ ions are excited only after the density is much higher than the density at which CO molecule is excited. H^{13}CO$^+$ ions are used to explore the region with higher density than that observed by C^{18}O. Figure 1.4 shows the map of cores observed by H^{13}CO$^+$ ions. The cores shown in the lower panels are accompanied with infrared sources. The energy source of the stellar IR radiation is thought to be maintained by the accretion energy. That is, since the gravitational potential energy at the surface of a protostar with a radius r_* and a mass M_* is equal to $\Phi \simeq -GM_*/r_*$, the kinetic energy of the gas accreting on the stellar surface is approximately equal to $\sim GM_*/r_*$. The energy inflow rate owing to the accretion is $(\sim GM_*/r_*) \times A(c_s^3/G)$, where $\dot{M} = A(c_s^3/G)$ is the mass accretion rate. In the upper panels, the cores without IR sources are shown. This core does not show accretion but collapse. That is, before a proto**star** is formed, the core itself contract owing to the gravity.

In Figure 1.4, H^{13}CO$^+$ total column density maps of the C^{18}O cores are shown. Cores in the lower panels have associated IRAS sources, while the cores in the upper panels have no IRAS sources. Since the IRAS sources are thought to be protostars or objects in later stage, the core seems to evolve from that without an IRAS sources to that with an IRAS source. From this, the core with an IRAS source is called **protostellar core**, which means that the cores contain protostars. On the other hand, the core without IRAS source is called pre-protostellar core or, in short, **pre-stellar core**.

Figure 1.4 shows that the prestellar cores are less dense and more extended than the protostellar core. This seems to suggest the density distribution around the density peak changes between before and after the protostar formation.

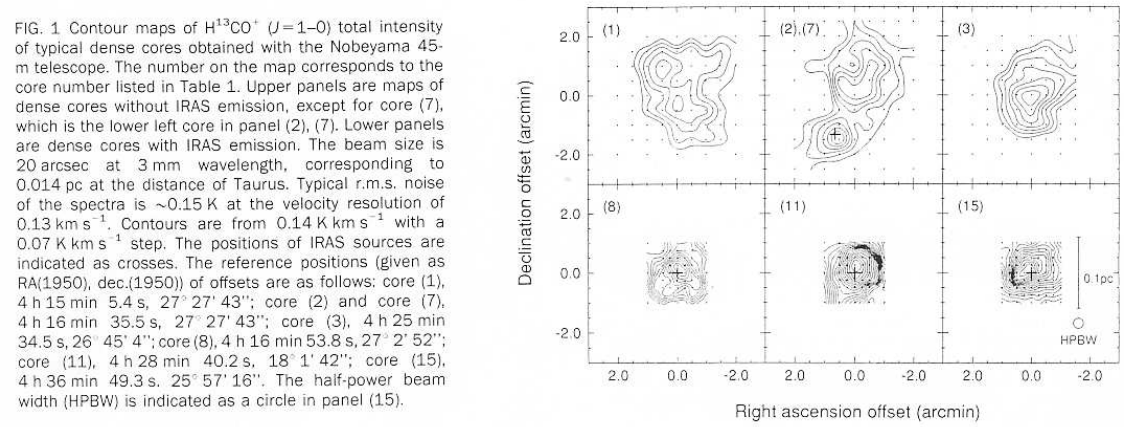

Figure 1.4: Pre-protostellar vs protostellar cores ($H^{13}CO^+$ map). Upper panel shows the $C^{18}O$ cores without associated IRAS sources. Lower panel shows the cores with IRAS sources. Taken from Fig.1 of Mizuno et al. (1994)

1.3 T-Tauri Stars

T-Tauri stars are observationally late-type stars with strong emission-lines and irregular light variations associated with dark or bright nebulosities. T-Tauri stars are thought to be low-mass pre-main-sequence stars, which are younger than the main-sequence stars. Since these stars are connecting between protostars and main-sequence stars, they attract attention today. More massive counterparts are Herbig Ae-Be stars. They are doing the Kelvin contraction in which the own gravitational energy released as it contracts gradually is the energy source of the luminosity. Many emission lines are found in the spectra of T-Tauri stars. WTTS (Weak Emission T-Tauri Stars) and CTTS (Classical T-Tauri Stars) are classified by the equivalent widths of emission lines. That is, the objects with an EW of Hα emission $<$ 1nm = 1A is usually termed a WTTS. Figure 1.5 is the HR diagram ($T_{\rm eff} - L_{\rm bol}$) of T-Tauri stars in Taurus-Auriga region (Kenyon & Hartman 1995). WTTSs distribute near the main-sequence and CTTSs A number of theoretical evolutional tracks for pre-main-sequence stars with $M \sim 0.1M_\odot - 2.5M_\odot$ are shown in a solid line, while the isochorones for ages of 10^5yr, 10^6yr, 10^7yr are plotted in a dashed line. Vertical evolutional paths are the Hayashi convective track. Since D=^{2}H has a much lower critical temperature (and density) for a fusion nuclear reaction to make He than ^{1}H, Deuterium begins to burn before reaching the zero-age-main sequence. This occurs near the isochrone for the age of 10^5yr and some activities related to the ignition of Deuterium seem to make the central star visible (Stahler 1983).

1.4 Spectral Energy Distribution

A tool to know the process of star formation is provided by the spectral energy distribution (SED) mainly in the near- and mid-infrared light. T-Tauri stars and protostars have typical respective SEDs. IR SEDs of T-Tauri stars were classified into three as Class I, Class II, and Class III, from a standpoint of relative importance of the radiation from a dust disk to the stellar black-body radiation. Today, the classification is extended to the protostars, which is precedence of T-Tauri stars, and they are called Class 0 objects. (Unfortunately, there is no zero in Roman numerals.) In Figure 1.6, typical SEDs and models of emission regions are shown.

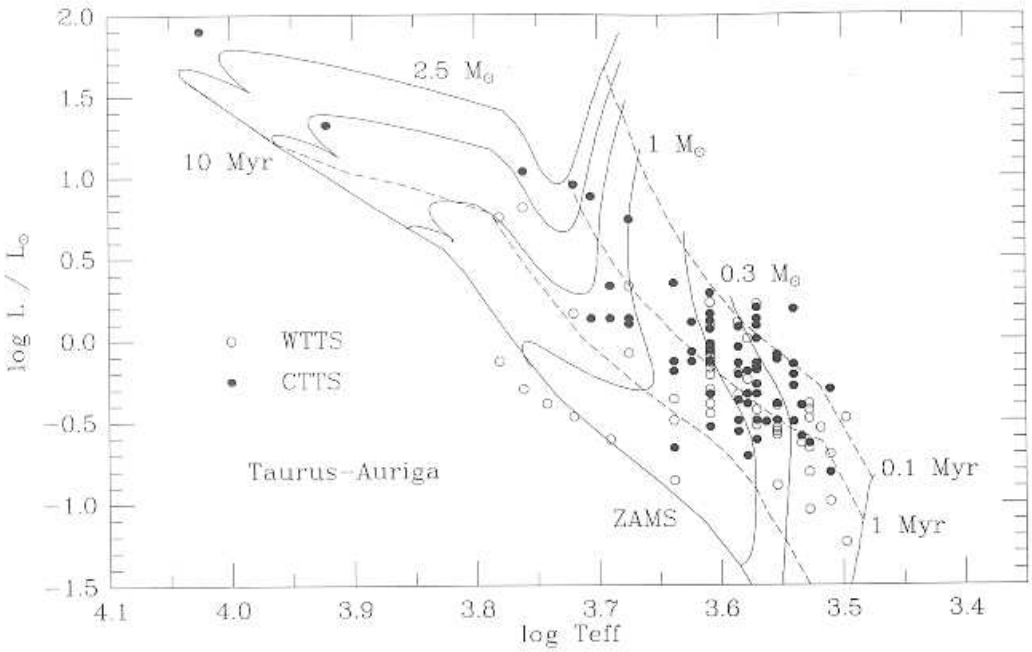

Fig. 1.2. HR diagram positions of young stars lying within the Taurus–Auriga molecular cloud complex (Figure 1.1). For comparison, theoretical evolutionary tracks for pre-main-sequence stars of masses 2.5, 2.0, 1.5, 1.0, 0.5, 0.3, and 0.1 $M_\odot$ are shown. The dashed lines are isochrones for ages of 10^5, 10^6, and 10^7 yr (0.1, 1, and 10 Myr), with the hydrogen-fusion 'zero-age main sequence' or ZAMS shown as the lowest line running from upper left to lower right. The open circles refer to weak-emission T Tauri stars (WTTS; see text), while the filled circles denote the positions of the classical T Tauri stars (CTTS). Stellar properties taken from Kenyon & Hartmann (1995); evolutionary tracks are from D'Antona & Mazzitelli (1994).

Figure 1.5: HR diagram of T-Tauri stars. Many emission lines are found in the spectra of T-Tauri stars. WTTS (Weak Emission T-Tauri Stars) and CTTS (Classical T-Tauri Stars) are classified by the equivalent widths of emission lines. That is, the objects with an EW of Hα emission $<$ 1nm is usually termed a WTTS. Taken from Fig.1.2 of Hartmann (1998).

1. Class III is well fitted by a black-body spectrum, which shows the energy mainly comes from a central star. This SED is observed in the weak-line T-Tauri stars. Although T-Tauri stars show emission lines of such as Hydrogen Balmar sequence, The weak-line T-Tauri stars do not show prominent emission lines, which indicates the amount of gas just outside the star (this seems to be supplied by the accretion process) is small. In this stage, a disk has been disappeared or extremely less-massive disk is still alive.

2. Class II SED is fitted by a black-body with a single temperature plus excess IR emission. This shows that there is a dust disk around a pre-main sequence star and it is heated by the radiation from the central star. The width of the spectrum of the disk component is much wider than that expected from a single-temperature black-body radiation. Thus the disk has a temperature gradient which decreases with increasing the distance from the central star. In this stage, the dust disk is more massive than that of Class III sources. Classical T-Tauri stars have such SEDs.

3. In Class I SED, the mid infrared radiation which seems to come from the dust envelope is predominant over the stellar black-body radiation. Since the stellar black-body radiation seems to escape at least partially from the dust envelope, a relatively large solid angle is expected for a region where the dust envelope does not intervene.

4. Class 0 SED seems to be emitted by isothermal dust with $\sim$ 30K. The protostar seems to be completely covered by gas and dust and is obscured by the large optical depth in the dust envelope. No contribution can be reached from the stellar-black body radiation.

The reason why the emission from the disk becomes wide in the spectral range is understood (Fig.1.7) as follows: Temperature of the disk is determined by a balance of heating and cooling. Assuming the disk is geometrically thin but optically thick, the cooling per unit area is given by the equation of the black-body Planck radiation. Therefore the temperature is determined by the heating predominantly by viscous heating and extra heating by the radiation from the central star. The flux density emitted by the disk is given by

$$\nu F_\nu \sim \int \nu \pi B_\nu [T(r)] 2\pi r dr \sim r(T \text{ or } \nu)^2 \nu B_\nu. \tag{1.1}$$

Assuming the radial distribution of temperature as

$$T = T_0 \left(\frac{R}{R_0} \right)^{-q}, \tag{1.2}$$

($q = 3/4$ for the standard accretion disk) and taking notice that each temperature in the disk radiates at a characteristic frequency $\nu \propto T$ (the Wien's law for black-body radiation)

$$\nu F_\nu \sim r^2 \nu B_\nu \propto \nu^4 T^{-2/q} \propto \nu^{4-2/q}, \tag{1.3}$$

where we used the fact that the peak value of $B_\nu \propto \nu^3$. Therefore, it is shown that

$$\nu F_\nu \propto \nu^n; \qquad n = 4 - \frac{2}{q}. \tag{1.4}$$

As shown in the previous section, we have no young **stellar** objects found by IR before a protostar is formed. These kind of objects (pre-protostellar core) are often called Class -1. The classification was originally based on the SED and did not exactly mean an evolution sequence. However, today YSOs are considered to evolve as the sequence of the classes: Class -1 $\rightarrow$ Class 0 $\rightarrow$ Class I $\rightarrow$ Class II $\rightarrow$ Class III $\rightarrow$ main-sequence star.

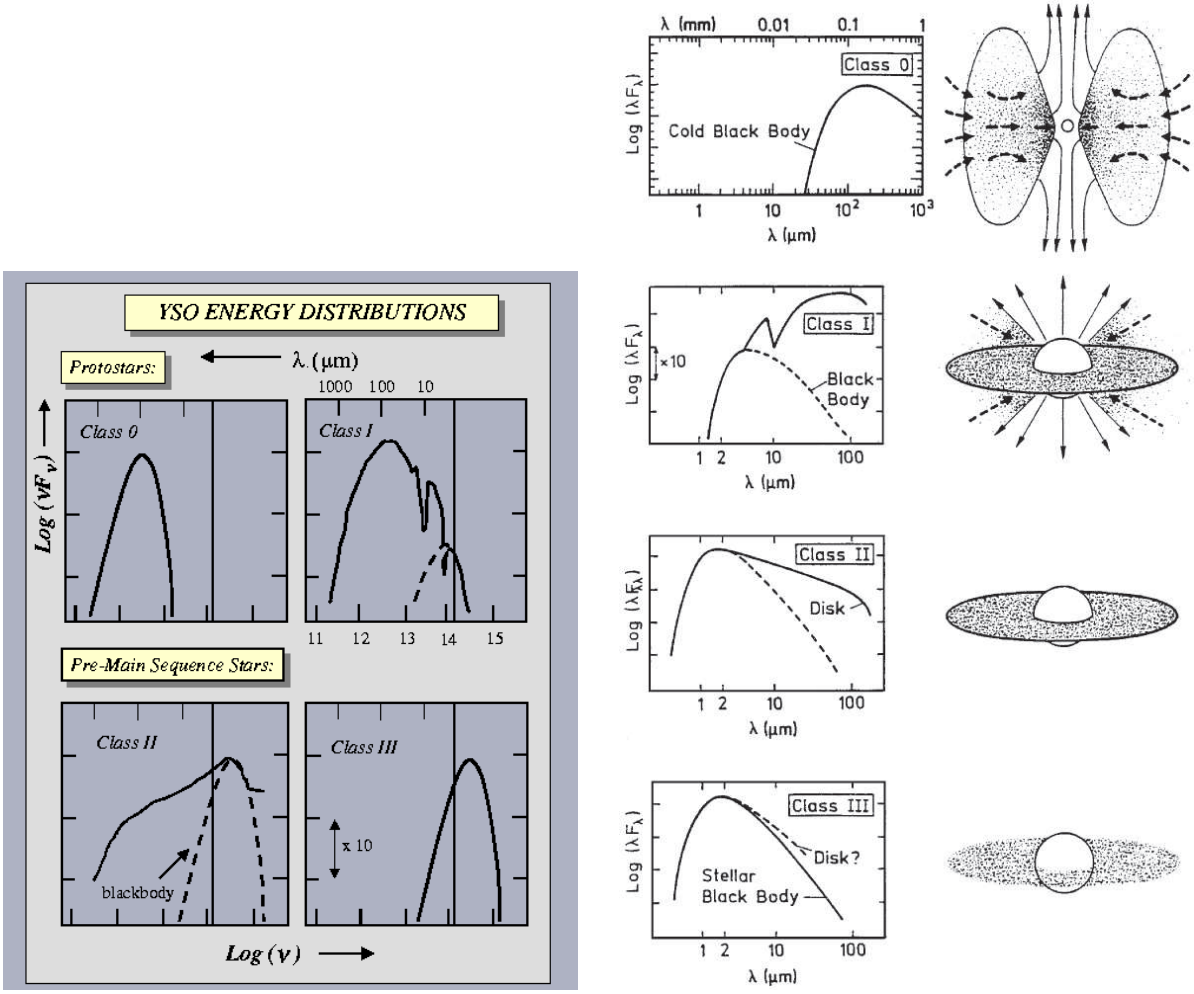

Figure 1.6: Spectral Energy Distribution (SED) of young stellar objects (YSOs) and their models. (*Left*:) $\nu - \nu F_\nu$ plot taken from Lada (1999). (*Right*:) $\lambda - \lambda F_\lambda$ plot taken from André (1994)

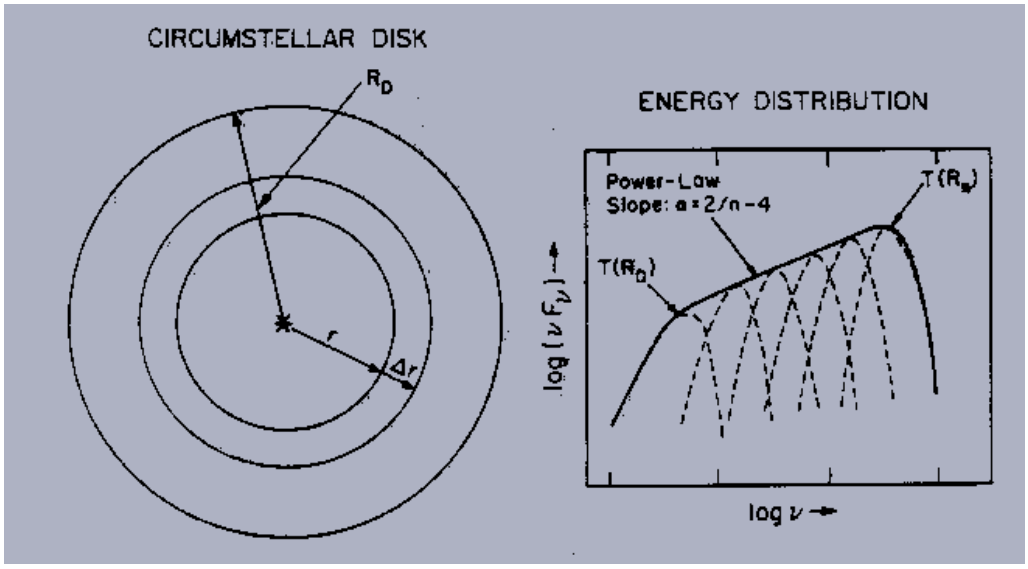

Figure 1.7: Explanation for the spectral index of the emission from a geometrically thin but optically thick disk. Taken from Fig.16 of Lada (1999).

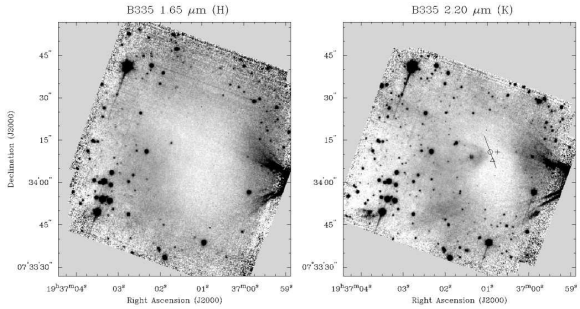

Figure 1.8: Near infrared images of B335, which is Class 0 source.

1.5 Protostars

1.5.1 B335

B335 is a dark cloud (Fig.1.8) with a distance of $D \simeq 250$pc. Inside the dark cloud, a Class 0 IR source is found. The object is famous for the discovery of gas infall motion. In Figure 1.9, the line profiles of CS $J = 2 - 1$ line emissions are shown (Zhou et al. 1993). The relative position of the profiles correspond to the position of the beam. (9,9) represents the offset of (9",9") from the center. At the center (0,0), the spectrum shows two peaks and the blue-shifted peak is brighter than the red-shifted one. This is believed to be a sign of gas infall motion. The blue-red asymmetry is explained as follow:

1. Considering a spherical symmetric inflow of gas, whose inflow velocity v_r increases with reaching the center (a decreasing function of r)

2. Considering a gas element at $\mathbf{r}$ moving at a speed of $v_r(\mathbf{r}) < 0$, the velocity projected on a line-of-sight is equal to

$$v_{\rm line-of-sight} = v_{\rm systemic} + v_r \cos\theta, \tag{1.5}$$

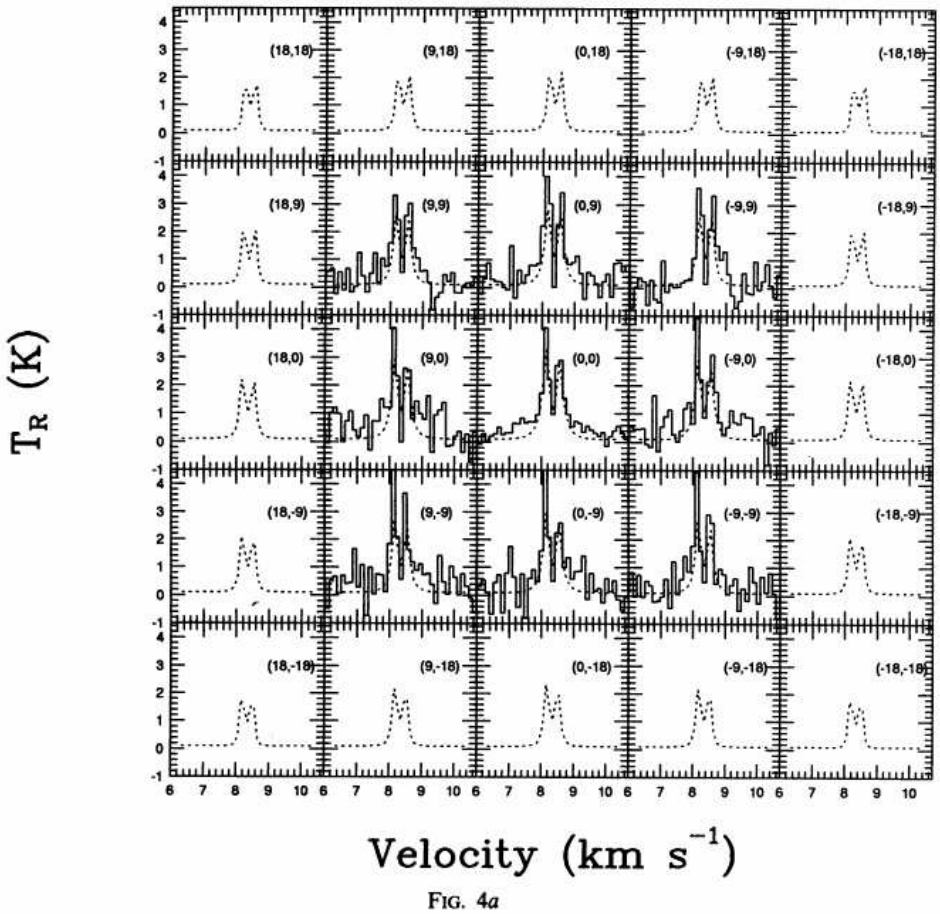

Figure 1.9: Line profile of CS $J = 2 - 1$ line radio emission. Model spectra illustrated in a dashed line (Zhou 1995) are overlaid on to the observed spectra in a solid line (Zhoug et al 1993).

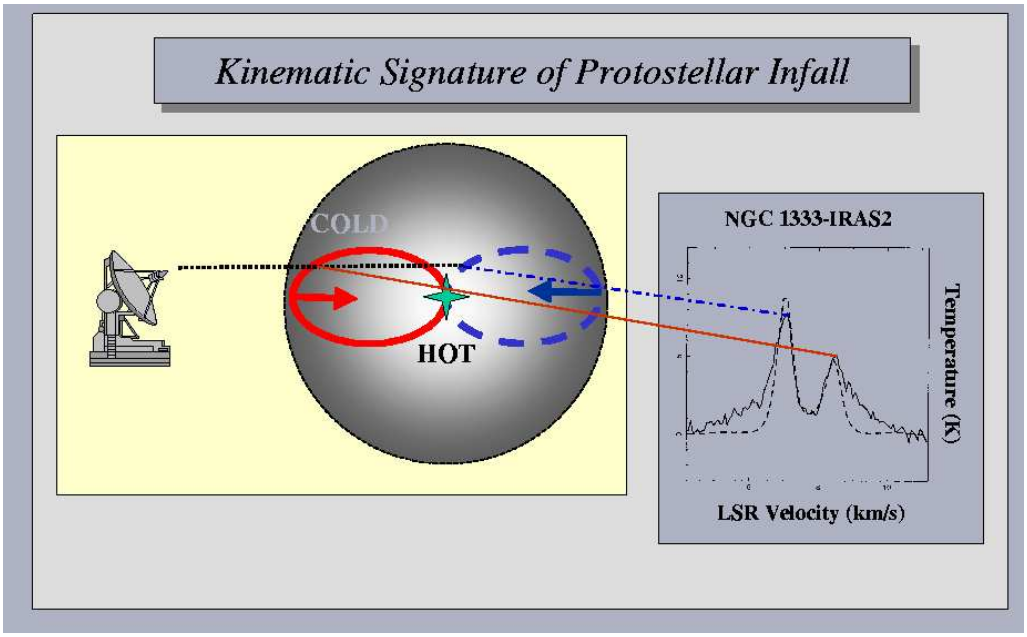

Figure 1.10: Explanation of blue-red asymmetry when we observe a spherical symmetric inflow motion. An isovelocity curve for the red-shifted gas is plotted in a solid line. That for the blue-shifted gas is plotted in a dashed line. Taken from Fig.14 of Lada (1999).

where $v_{\rm systemic}$ represents the systemic velocity of the cloud (line-of-sight velocity of the cloud center) and θ is the angle between the line-of-sight and the position vector of the gas element. The isovector lines, the line which connect the positions whose procession/recession velocities are the same, become like an ellipse shown in Fig.??.

3. An isovelocity curve for the red-shifted gas is plotted in a solid line. That for the blue-shifted gas is plotted in a dashed line. If the gas is optically thin, the blue-shifted and red-shifted gases contribute equally to the observed spectrum and the blue- and red-shifted peaks of the emission line should be the same.

4. In the case that the gas has a finite optical depth, for the red-shifted emission line a cold gas in the fore side absorbs effectively the emission coming from the hot interior. On the other hand, for the blue-shifted emission line, the emission made by the hot interior gas escapes from the cloud without absorbed by the cold gas (there is no cold blue-shifted gas).

5. As a result, the blue peak of the emission line becomes more prominent than that of the read-shifted emission. This is the explanation of the blue-red asymmetry.

In Figure 1.9, model spectra calculated with the Soblev approximation (Zhou 1995) are shown. These show the blue-red asymmetry (the blue line > the red line).

Many bipolar molecular outflows are found in star forming regions. B335 is also an outflow source. In Figure 1.11, distributions of high density gases traced by the $C^{18}O$ and $H^{13}CO^+$ lines are shown as well as the bipolar outflow whose outline is indicated by a shadow (Hirano et al 1988). Comparing left and right panels, it is shown that the distribution of $C^{18}O$ gas is more extended than that of $H^{13}CO^+$, which traces higher-density gas. And the distribution of the $H^{13}CO^+$ is more compact and the projected surface density seems to show the the actual distribution is spherical. And the

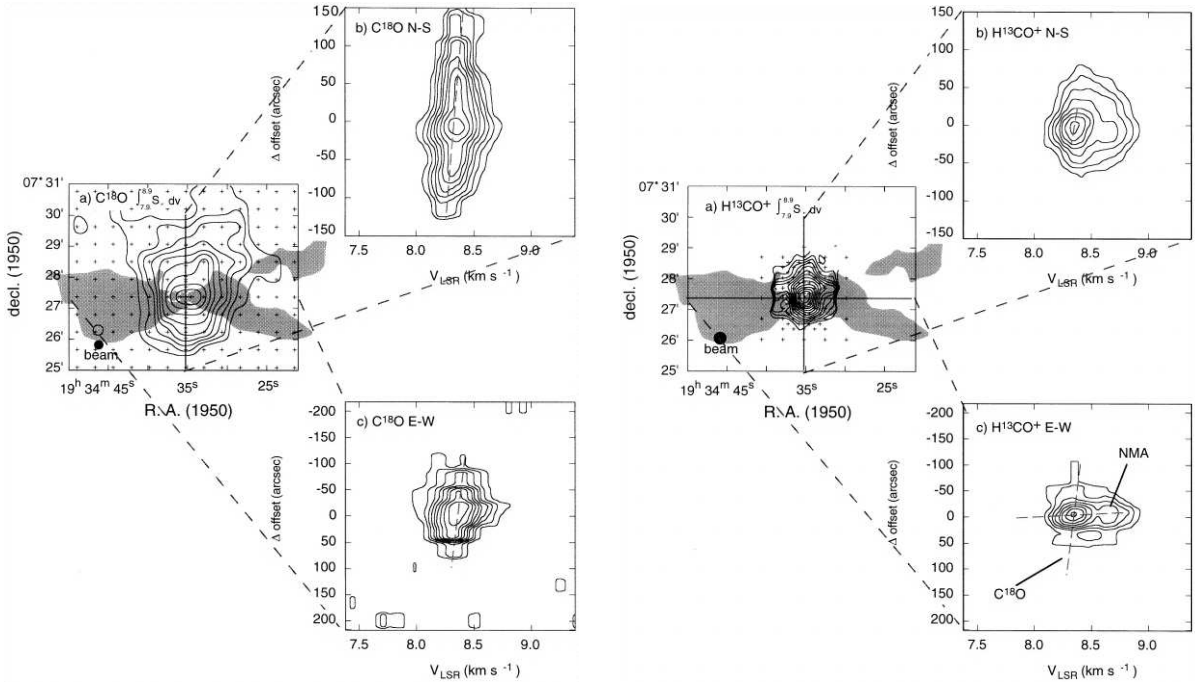

Figure 1.11: $C^{18}O$ total column density map (left) and $H^{13}CO^+$ channel map (right) of B335 along with the position-velocity maps along the major and minor axes. Taken from Fig.3 of Saito et al (1999).

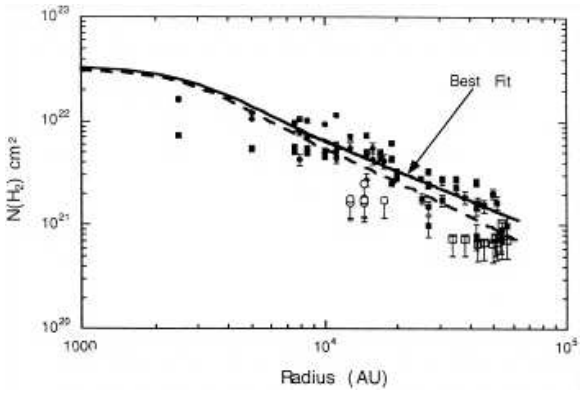

Figure 1.12: Column density distribution $N_{\rm H}(r)$ derived from the $H^{13}CO^+$ and $C^{18}O$ data taken by the Nobeyama 45 m telescope. Taken from Fig.9 of Saito et al (1999).

molecular outflow seems to be ejected in the direction of the minor axis of the high-density gas. It may suggest that (1) a molecular outflow is focused or collimated by the effect of density distribution or that (2) collimation is made by the magnetic fields which run preferentially perpendicularly to the gas disk. This gas disk is observed by these high density tracers.

Combining the $C^{18}O$ and $H^{13}CO^+$ distributions, the surface density distribution along the major axis is obtained by Saito et al (1999). From the lower panel of Figure **??**, the column density distribution is well fitted in the range from 7000 to 42,000 AU in radius,

$$\Sigma(r) = 6.3 \times 10^{21} cm^{-2} \left(\frac{r}{10^4 \mathrm{AU}} \right)^{-0.95}, \tag{1.6}$$

where they omitted the data of $r \lesssim 7000$ since the beam size is not be negligible. Similar power-law density distributions are found by the far IR thermal dust emission.

1.5.2 L1551 IRS 5

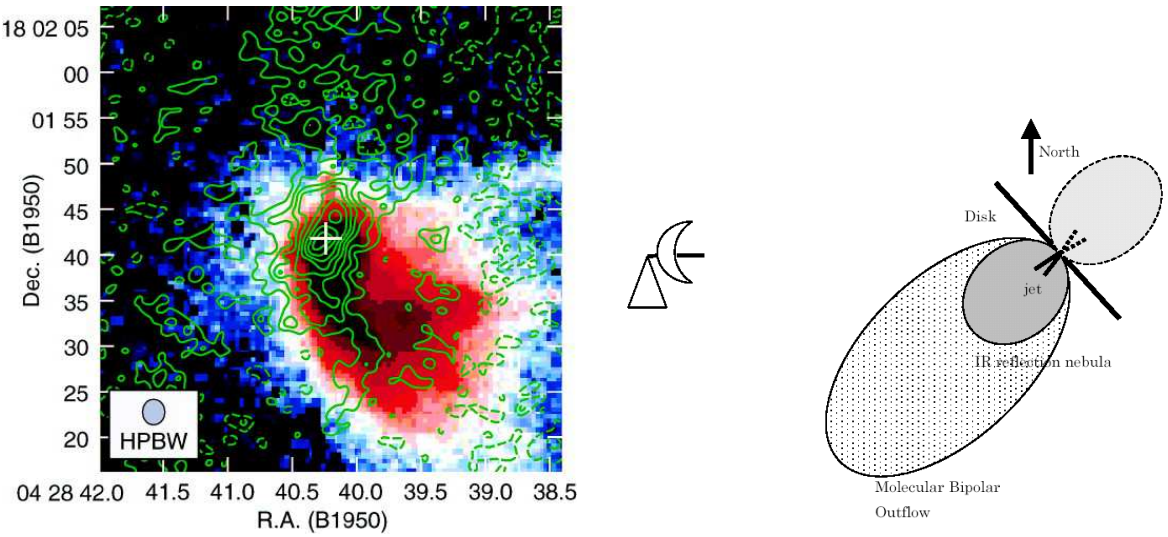

Figure 1.13: (*Left*:) ^{13}CO column density distribution. The contour lines represent the distribution of ^{13}CO column density. 2.2 μm infra-red reflection nebula is shown in grey scale which was observed by Hoddap (1994). (*Right*:) Schematic view of L1551 IRS5 region.

L 1551 IRS 5 is one of the most well studied objects. This has an infra-red emission nebulosity (Fig.1.13). It is believed that there is a hole perpendicular to the high-density disk and the emission from the central star escapes through the hole and irradiate the nebulosity. In this sense this is a reflection nebula. L 1551 IRS 5 has an elongated structure of dense gas similar to that observed in B335. The gas is extending in the direction from north-west to south-east [Fig.1.13 (left)]. Since the opposite side of the nebulosity is not observed, the opposite side of nebulosity seems to be located beyond the high-density disk and be obscured by the disk. This is possible if we see the south surface of the high-density disk as in Figure 1.13 (right).

Infall Motion

The inflow motion is measured. Figure 1.14 shows the isovelocity contours measured by the ^{13}CO $J = 1-0$ observation (Ohashi et al 1996). It should be noticed that the isovelocity lines run parallelly

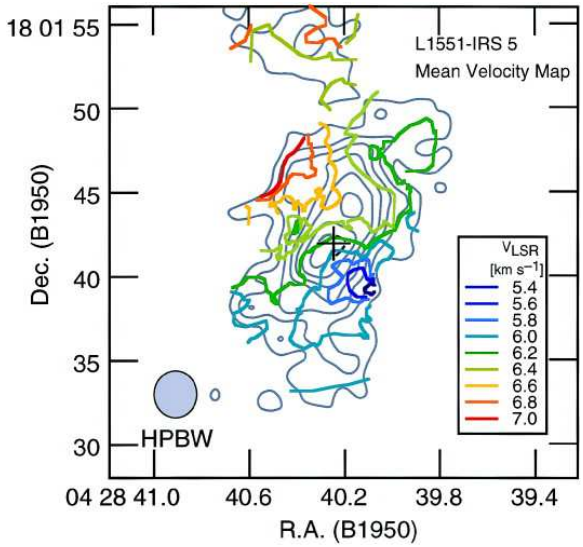

Figure 1.14: (Left) Isovelocity contours measured by the ^{13}CO $J = 1 - 0$ line. It should be noticed that the isovelocity lines run parallelly to the major axis. The north-eastern side shows a red-shift and the south-western side shows a blue-shift.

to the major axis. The north-eastern side shows a red-shift and the south-western side shows a blue-shift. Considering the configuration of the gas disk shown in Fig.1.13 (right), this pattern of isovelocity contours indicates not outflow but inflow. That is, the north-east side is a near side of the disk and the south-west side is a far side. Since a red-shifted motion is observed in the near side and a blue-shifted motion is observed in the far side, it should be concluded that the gas disk of the L1551 IRS5 is now infalling.

Optical Jet

HST found two optical jets emanating from L1551 IRS5. This has been observed by SUBARU telescope jet emission is dominated by [FeII] lines in the J- and H-bands. The jet extents to the south-western direction and disappears at $\sim$ 10" $\simeq$ 1400AU from the IRS5. The width-to-length ratio is very small $\lesssim 1/10$ or less, while the bipolar molecular outflow shows a less collimated flow. As for the origin of the two jets, these two jets might be ejected from a single source. However, since there are at least two radio continuum sources in IRS5 within the mutual separation of $\sim$ 0."5 [see Fig.1.15 (right)], these jets seem to be ejected from the two sources independently.

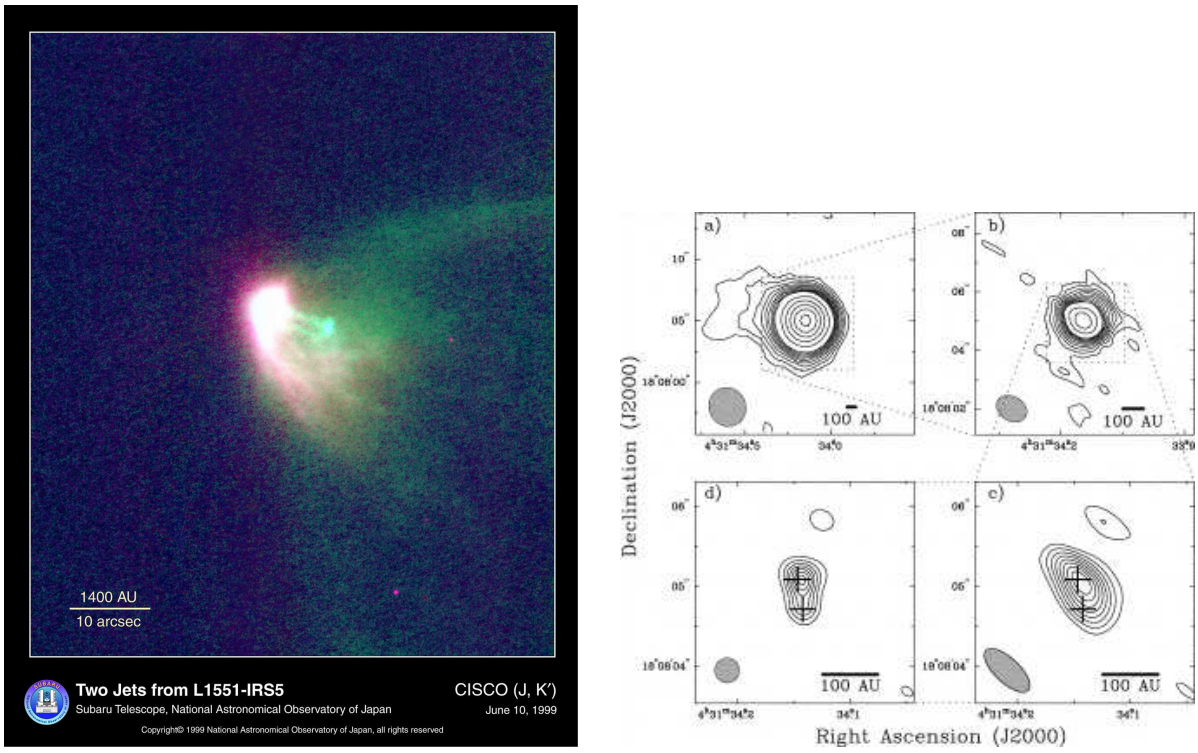

Figure 1.15: (Left:) Infrared image (J- and K-band) of the IR reflection nebula around L1551 IRS5 by SUBARU telescope. Taken from Fig.1 of Itoh et al. (2000). (A jpeg file is available from the following url: `http://SubaruTelescope.org/Science/press_release/9908/L1551.jpg`). (Right:) Central 100 AU region map of L1551 IRS5. This is taken by the $\lambda = 2.7$cm radio continuum observation. Deconvolved map (lower-left) shows clearly that IRS5 consists of two sources. Taken from Looney et al. (1997).

Although the lengths of these jets are restricted to 10", Herbig-Haro jets, which are much larger than the jets in L1551 IRS5, have been found. HH30 has a $\sim$ 500 AU-scale jet whose emission is mainly from the shock-excited emission lines. One of the largest one is HH111, which is a member of the Orion star forming region and whose distance is as large as $D \sim 400$pc, and a jet with a length of $\sim$ 4pc is observed. Source of HH111 system is thought to consist of at least binary stars or possibly triple stars [Reipurth et al (1999)]. Star A, which coincides with a $\lambda = 3.6cm$ radio continuum source (VLA 1), shows an elongation in the VLA map whose direction is parallel to the axis of the jet. Therefore, star A is considered to be a source of the jet. Since the VLA map of star A shows another elongated structure perpendicular to the jet axis, star A may be a binary composed by two outflow sources.

1.6 L 1544: Pre-protostellar Cores

L1544 is known as a pre-protostellar core (Taffala et al 1998). That shows an infall motion but this contains no IR protostars In Figure 1.17(*left*) CCS total column density map is shown, which shows an elongated structure. Ohashi et al (1999) have found both rotation and infall motion in the cloud. PV diagram along the minor axis shows the infall motion. That along the major axis indicates a rotational motion, which is shown by a velocity gradient. Due to a finite size of the beam, a contraction motion is also shown in the PV diagram of the major axis.

1.7 Magnetic Fields

Directions of B-Field are studied by (1) measuring the polarization of light which is suffered from interstellar absorption; in this case the direction of magnetic field is parallel to the polarization vector. However, the polarization measurement in the near IR wavelength limited to the region with low gas density, because background stars suffer severe absorption and becomes hard to observe if we want to measure the polarization of the high-density region. More direct method is (2) measuring the linear polarization of the thermal emission from dust in the mm wavelengths; in this case the direction of magnetic field is perpendicular to the polarization vector. The absorption does not have a severe effect in this mm wavelength.

Prestellar Core

Figure 1.18 illustrates the polarization maps of three prestellar cores (L1544, L183, and L43) done in the 850 μm band by JCMT-SCUBA. In L1544 and L183 the mean magnetic fields are at an angle of 30 deg to the minor axes of the cores. L43 is not a simple object; there is a T Tauri star located in the second core which extends to south-western side of the core (an edge of this core is seen near the western SCUBA frame boundary). And a molecular outflow from the source seems to affect the core. The magnetic field as well as the gas are swept by the molecular outflow. L43 seems an exception. The fact that the mean magnetic fields are parallel to the minor axis of the gas distribution seems the gas contracts preferentially in the direction parallel to the magnetic fields.

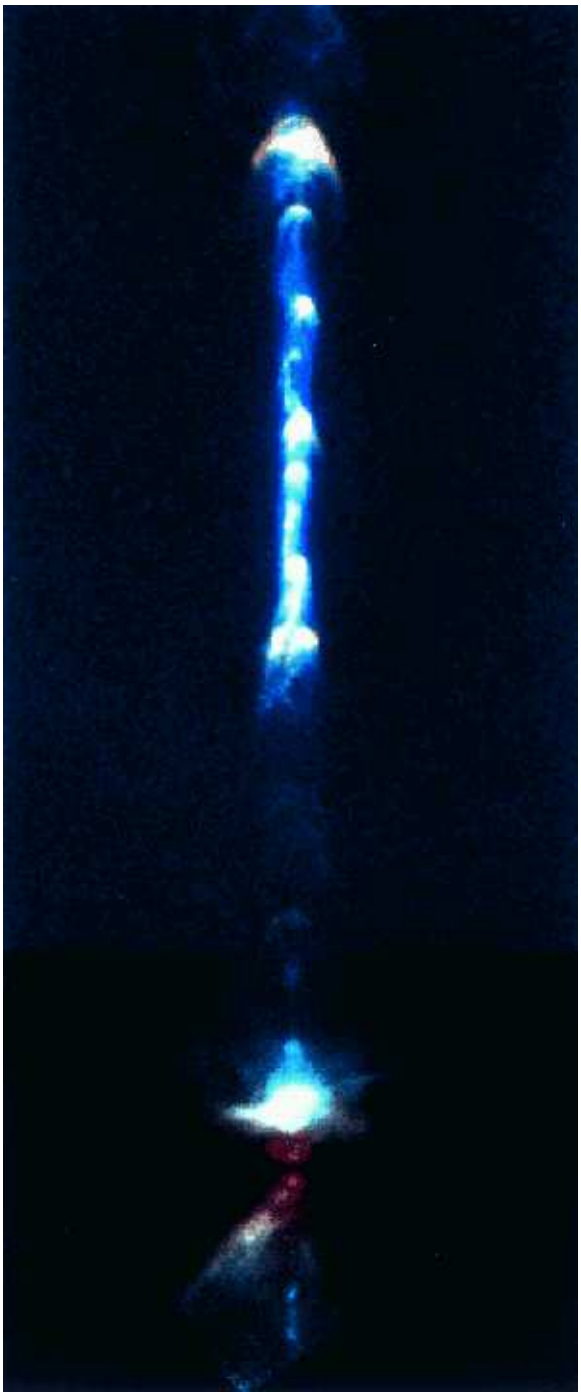

Figure 1.16: A mosaic image of HH 111 based on HST NICMOS images (bottom) and WFPC2 images (top). Taken from Fig.1 of Reipurth et al (1999).

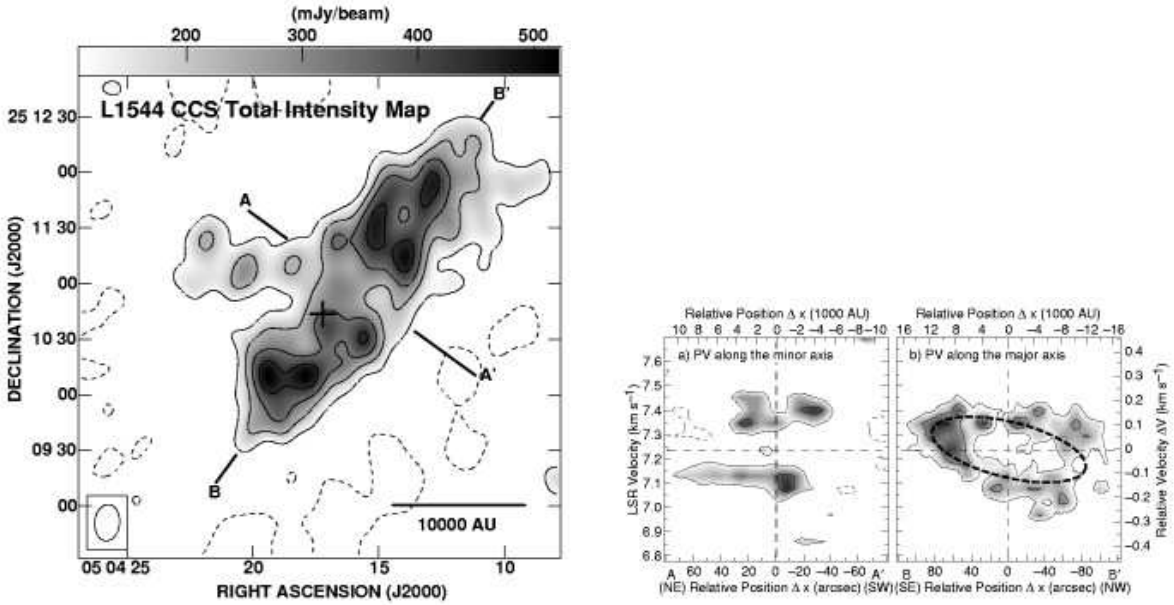

Figure 1.17: CCS image of prestellar core L1544. (*Left*:) Total intensity map. (*right*:) PV diagrams along the minor axis (left) and along the major axis (right).

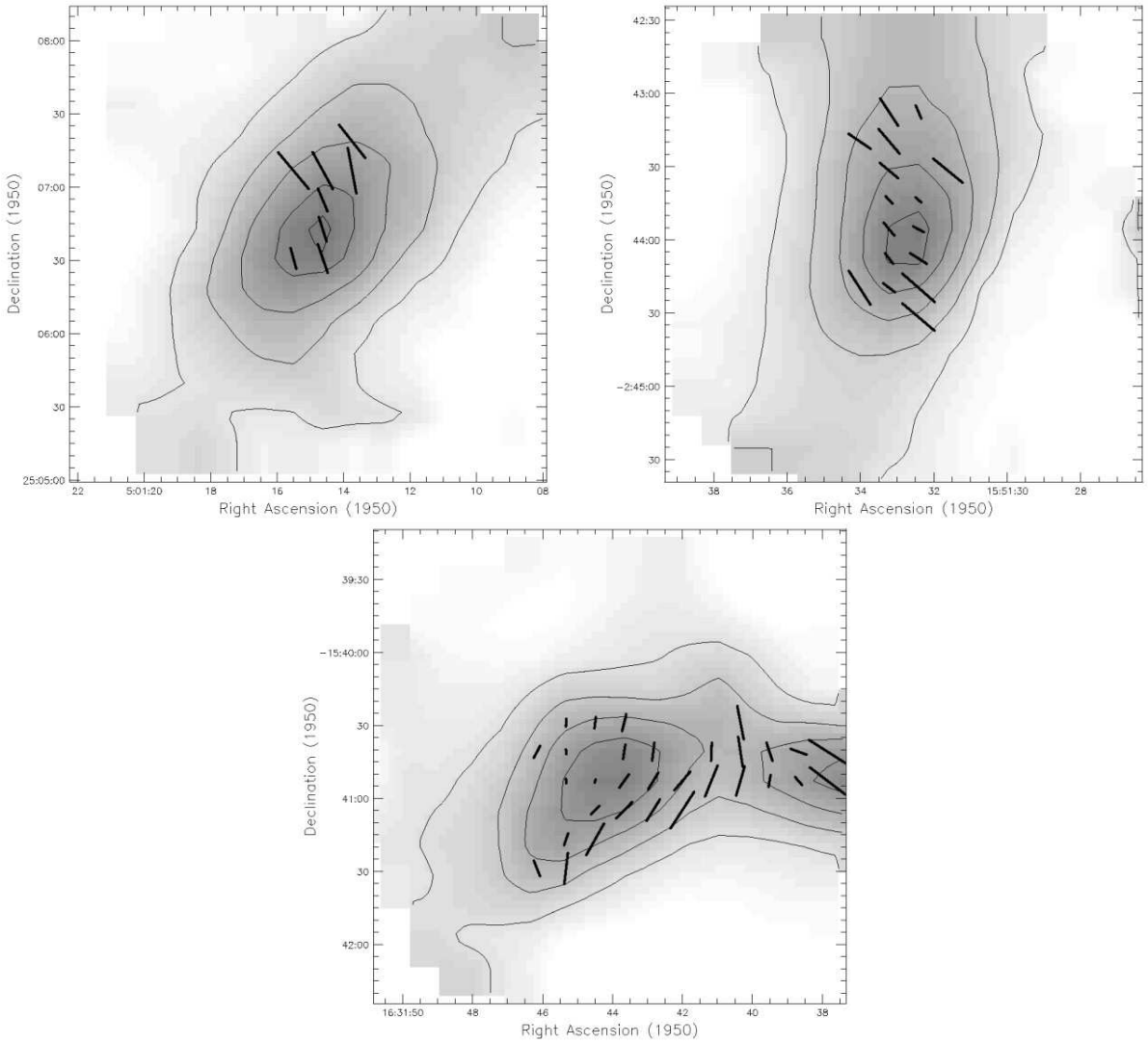

Figure 1.18: Directions of B-Field are shown from the linear polarization observation of 850 μm thermal emission from dust by JCMT-SCUBA. L 1544 and L183, the magnetic field and the minor axis of the molecular gas distribution coincide with each other within $\sim$ 30deg. Taken from Ward-Thompson et al (2000).

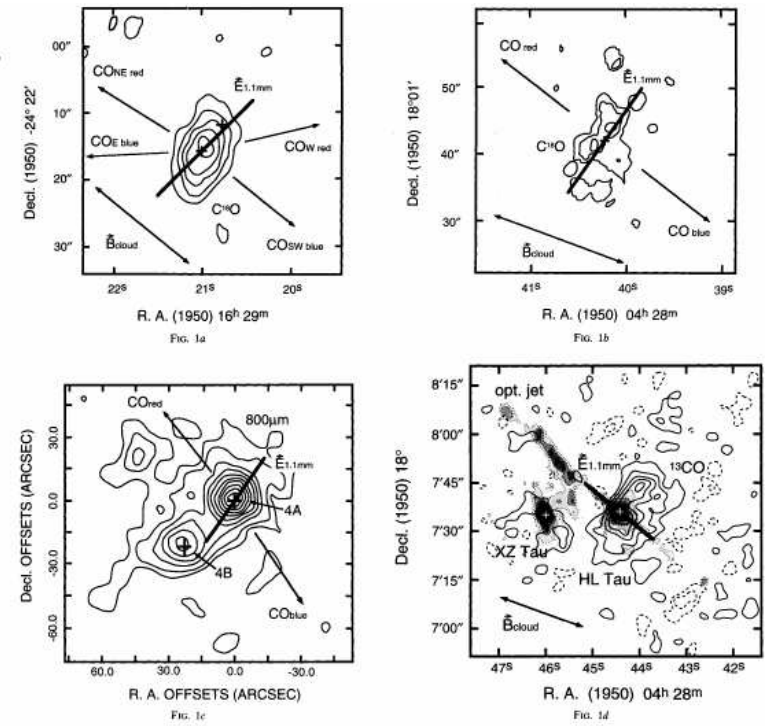

FIG. 1a FIG. 1b FIG. 1c FIG. 1d

FIG. 1.—(*a*) IRAS 16293−2422: Geometrical relationship among the electric vector of the 1.1 mm continuum polarization (19″ beam), the embedding cloud magnetic field from optical or near-infrared polarimetry, the envelope/disk structure of gas or dust, and the directions of blue/red lobes of high-velocity CO outflows (this work; Vrba et al. 1976; Tamura 1988; Mundy et al. 1990; Mizuno et al. 1990). Note that the direction of the envelope/disk magnetic field inferred from the 1 mm polarization is perpendicular to the electric vector. (*b*) Same as (*a*) except for L1551 IRS 5 (this work; Vrba et al. 1976; Sargent et al. 1988; Snell et al. 1980). (*c*) Same as (*a*) except for NGC 1333 IRAS 4A (this work; Sandell et al. 1991; Sandell & Aspin 1933). (*d*) Same as (*a*) except for HL Tau. The optical jet is also shown (this work; Hayashi et al. 1993; Vrba et al. 1976; Mundt, Ray, & Bührke 1988).

Figure 1.19: Polarization of the radio continuum λ = 1mm, λ = 0.8mm. IRAS 16293-2422 (upper-left), L1551 IRS5 (upper-right), NGC1333 IRAS 4A (lower-left), and HL Tau (lower-right). Taken from Tamura et al (1995).

1.7.1 Cores with Protostars

B-field at the position of protostars and T-Tauri stars are measured for IRAS 16293-2422, L1551 IRS5, NGC1333 IRAS 4A, and HL Tau (Tamura et al. 1995). Although HL Tau is a T-Tauri star, it has a gas disk. Thus this is Class I source. The others are believed to be in protostellar phase (Class 0 sources). It is known that IRAS 16293-2422, L1551 IRS5, and HL Tau have disks with the radii of 1500-4000 AU from radio observations of molecular lines. Further, near infrared observations have shown that these objects have 300-1000 AU dust disks. Figure 1.19 shows the E-vector of polarized light. If this is the dust thermal radiation, the direction of B-fields is perpendicular to the polarization E-vector. Figure shows the B-fields run almost perpendicular to the elongation of the gas disk. Global directions of B-field outside the gas disk and the direction of CO outflows are also shown in the figure by arrows. It is noteworthy that the directions of local B-fields, global B-fields, and outflows coincide with each other within $\sim$ 30 deg.

1.8 Density Distribution

Motte & André (2001) made 1.3 mm continuum mapping survey of the embedded young stellar objects (YSOs) in the Taurus molecular cloud. Their maps include several isolated Bok globules, as well as protostellar objects in the Perseus cluster. For the protostellar envelopes mapped in Taurus, the results are roughly consistent with the predictions of the self-similar inside-out collapse model of Shu and collaborators. The envelopes observed in Bok globules are also qualitatively consistent with these predictions, providing the effects of magnetic pressure are included in the model. By contrast, the envelopes of Class 0 protostars in Perseus have finite radii $\lesssim$10000 AU and are a factor of 3 to 12 denser than is predicted by the standard model.

Another method to measure the density distribution is to use the near IR extinction. From $(H-K)$ colors of background stars, the local value of A_V in a dark cloud can be obtained using a standard reddening law,

$$A_V = 15.87E(H-K) \tag{1.7}$$

if the intrinsic colors of background stars are known. We can convert the extinction to the column density assuming the gas/dust ratio is constant

$$N(\mathrm{H}+\mathrm{H_2}) = 2\times 10^{21}\mathrm{cm}^{-2}\mathrm{mag}^{-1}A_V. \tag{1.8}$$

This is a standard method to obtain the local column density of the dark cloud using the near IR photometry.

See Figure 1.20. If the density distribution is expressed as

$$\rho(r) = \rho_0\left(\frac{r}{r_0}\right)^{-\alpha}, \tag{1.9}$$

where r is a physical distance from the center. The column density for the projected distance of the line-of-sight from the center of the cloud is given

$$N_\rho(p) = 2\int_0^{(R^2-p^2)^{1/2}} \rho\left[(s^2+p^2)^{1/2}\right] ds, \tag{1.10}$$

where R represents the outer radius of the cloud. Using equation (1.8), this yields A_V distribution

$$A_V(p) = 10^{-23}\rho_0 r_0^\alpha \int_0^{(R^2-p^2)^{1/2}} (s^2+p^2)^{-\alpha/2} ds. \tag{1.11}$$

If background stars are uniformly distributed, the number of stars with $A_V|_{\rm obs}$ is proportional to the area which satisfies $A_V|_{\rm obs} = A_V(p)$. That is, if we plot $A_V(p)$ against $2\pi p dp$, this gives the number distribution of background stars with A_V. Figure 1.22 shows the result of L977 dark cloud by Alves et al (1998).

Recently, Alves et al (2001) derived directly the radial distribution of N_H by comparing the $N_H(p)$ model distribution for B68. They obtained a distribution is well fitted by the Bonner-Ebert sphere in which a hydrostatic balance between the self-gravity and the pressure force is achieved (lower panels of Fig.1.22).

In this fields, we should pay attention to the density distribution in cylindrical clouds. As seen in the Taurus molecular cloud, there are may filamentary structures in a molecular cloud. In §4.1, we will give the distribution for a hydrostatic spherical symmetric and cylindrical cloud. The former is proportional to $\rho \propto r^{-2}$ and the latter is $\rho \propto r^{-4}$. Therefore, the distribution $\rho \propto r^{-4}$ was expected for cylindrical cloud. From near IR extinctions observation (Alves et al 1998), even if a cloud is

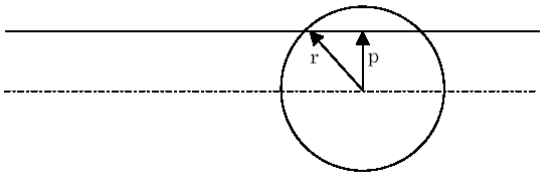

Figure 1.20: Schematic view to explain an A_V distribution.

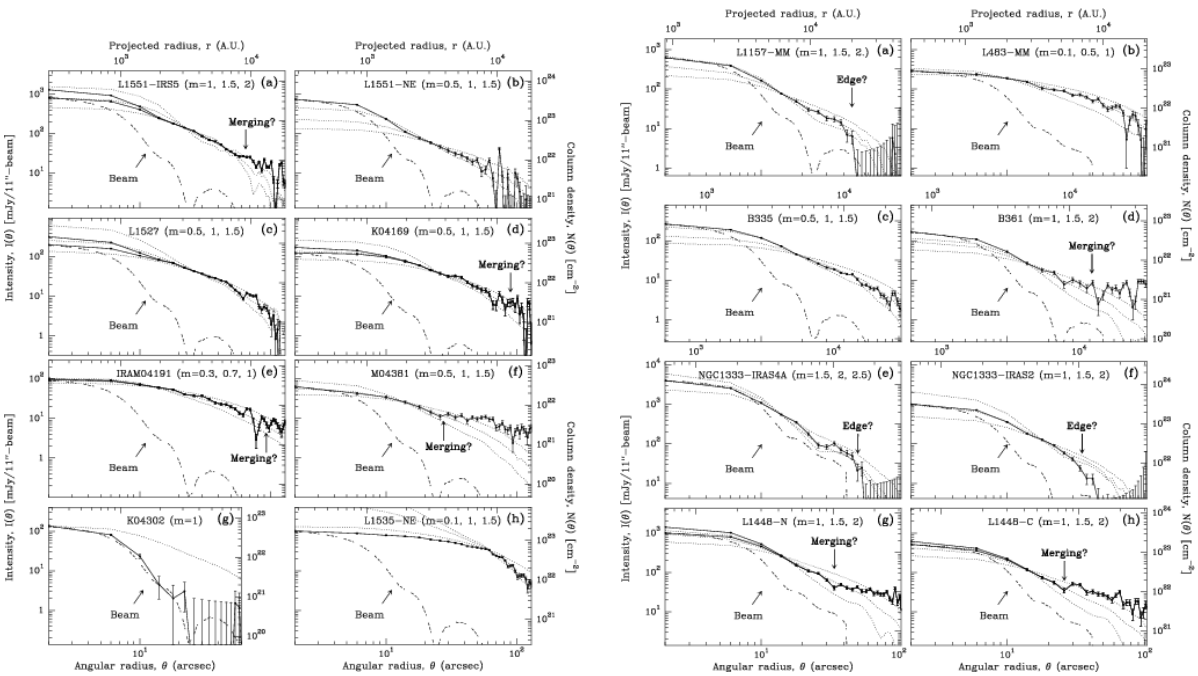

Figure 1.21: (*Left*:) Radial intensity profiles of the environment of 7 embedded YSOs (a-g) and 1 starless core (h). (*Right*:) Same as left panel but for 4 isolated globules (a-d) and 4 Perseus protostars (e-h). Taken from Motte & Andre (2001).

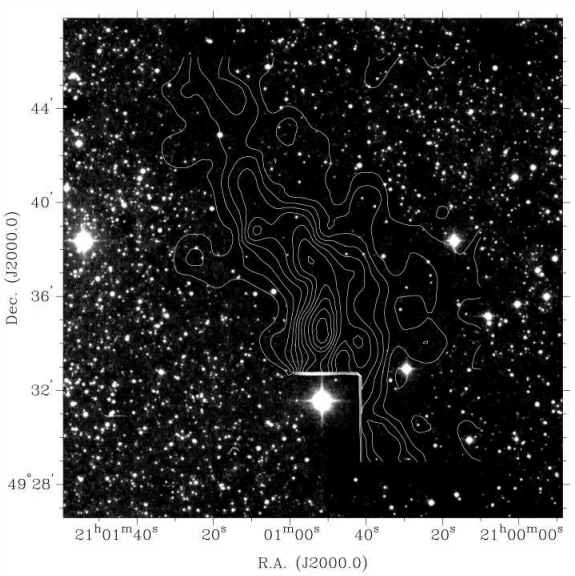

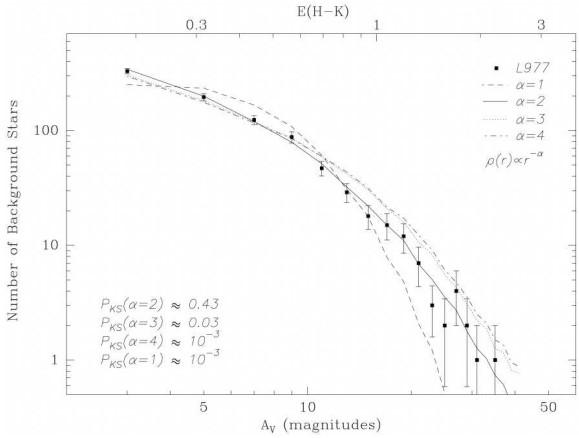

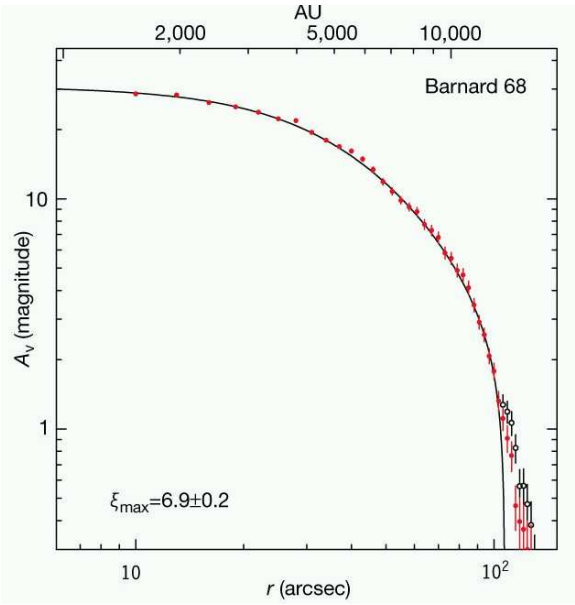

Figure 1.22: Density distribution of L977 (top) and B68 (bottom) dark clouds. (Top-left:) L977 dark cloud dust extinction map derived from the infrared (H-K) observations. (Top-right:) Observed frequency distribution of extinction measurements for L977 and the predictions from clouds models with density structures $\rho(r) \propto r^{-\alpha}$ having $\alpha = 1$ (dashed line), 2 (solid line), 3 (dotted line), and 4 (dash-dotted line). (Bottom-left:) B68 images (false color images made from B, V, and I images (top), and B, I, and K images (bottom)). (Bottom-right:) Spatial distribution of the column density,

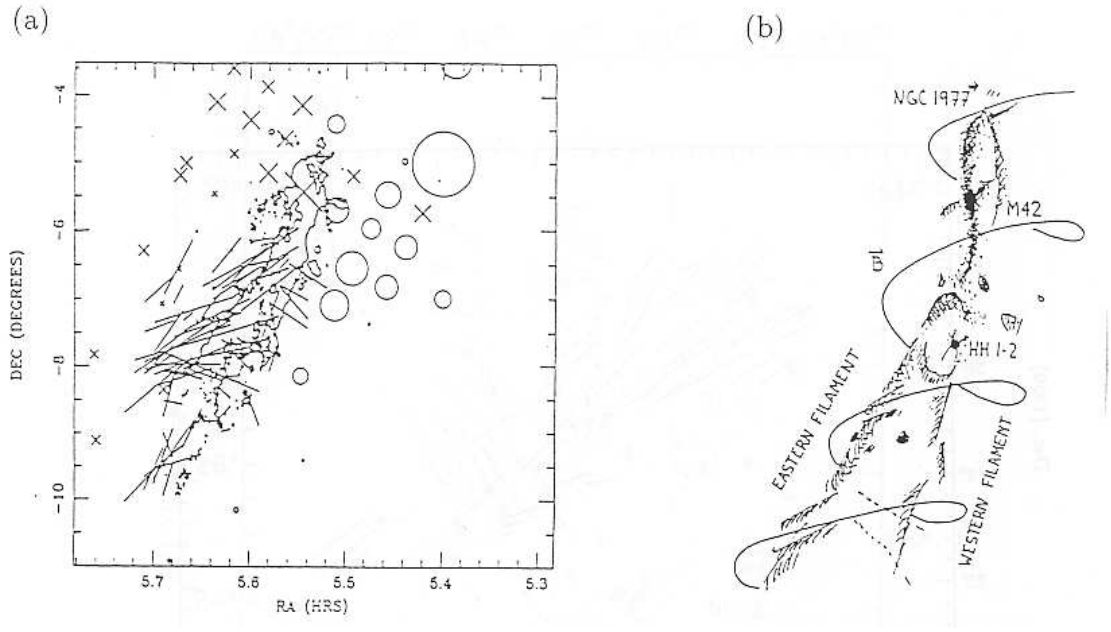

Figure 1.23: A structure of magnetic fields in the L1641 region. Polarization of light from embedded stars (Vrba et al. 1988) is shown by a bar. The direction of B-fields in the line-of-sight is observed using the HI Zeeman splitting, which is shown by a circle and cross (Heiles 1989).

rather elongated [Fig.1.22 (top-left)], the power of the density distribution is equal to not -4 but $\simeq -2$. Fiege, & Pudritz (2001) proposed an idea that a toroidal component of the magnetic field, B_ϕ, plays an important role in the hydrostatic balance of the cylindrical cloud (Fig.1.23).

1.9 Mass Spectrum

We have seen that a molecular cloud consists in many molecular cloud cores. For many years, there are attempts to determine the mass spectrum of the cores.

From a radio molecular line survey, a mass of each cloud core is determined. Plotting a histogram number of cores against the mass, we have found that a mass spectrum can be fitted by a power law as

$$\frac{dN}{dM} = M^{-n} \tag{1.12}$$

where dN/dM represents the number of cores per unit mass interval. Many observation indicate that $n \sim -1.5$.

Figure 1.24 (Motte et al 2001) shows the cumulative mass spectrum ($N(>M)$ vs. M) of the 70 starless condensations identified in NGC 2068/2071. The mass spectrum for the 30 condensations of the NGC 2068 sub-region is very similar in shape. The best-fit power-law is $N(>M) \propto M^{n+1} \propto M^{-1.1}$ above $M \gtrsim 0.8 M_\odot$. That is, $n = -2.1$. This power derived from the dust thermal emission is different from that derived by the radio molecular emission lines. The reason of the difference is not clear. However, the power $n+1 = -1.1$ which is close to the Salpeter IMF, $N(>M) \propto M^{-1.35}$ seems meaningful.

Paper	n	Region	Mass range
Loren (1989)	-1.1	ρ Oph	$10M_\odot \lesssim M \lesssim 300M_\odot$
Stutzki & Guesten (1990)	-1.7 ± 0.15	M17 SW	a few $M_\odot \lesssim M \lesssim$ a few $10^3 M_\odot$
Lada et al (1991)	-1.6	L1630	$M \gtrsim 20M_\odot$
Nozawa et al (1991)	-1.7	ρ Oph North	$3M_\odot \lesssim M \lesssim 160M_\odot$
Tatematsu et al. (1993)	-1.6 ± 0.3	Orion A	$M \gtrsim 50M_\odot$
Dobashi et al (1996)	-1.6	Cygnus	$M \gtrsim 100M_\odot$
Onish et al (1996)	-0.9 ± 0.2	Taurus	$3M_\odot \lesssim M \lesssim 80M_\odot$
Kramer et al.(1998)	$-1.6 \sim -1.8$	L1457 etc*	$10^{-4}M_\odot \lesssim M \lesssim 10^4 M_\odot$
Heithausen et al (2000)	-1.84	MCLD123.5+24.9,Polaris Flare	$M_J \lesssim M \lesssim 10M_\odot$

* MCLD126.6+24.5, NGC 1499 SW, Orion B South, S140, M17 SW, and NGC 7538

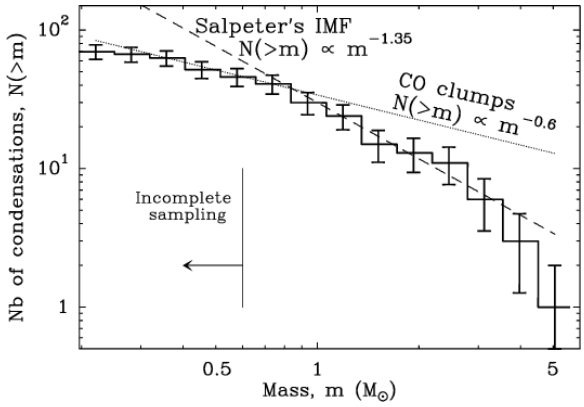

Figure 1.24: Cumulative mass distribution of the 70 pre-stellar condensations of NGC 2068/2071. The dotted and dashed lines are power-laws corresponding to the mass spectrum of CO clumps (Kramer et al. 1996) and to the IMF of Salpeter (1955), respectively. Taken from Fig.3 of Motte et al (2001).

Chapter 2

Physical Background

2.1 Basic Equations of Hydrodynamics

The basic equation of hydrodynamics are (1) the continuity equation of the density [equation (A.11)],

$$\frac{\partial \rho}{\partial t} + \mathrm{div}(\rho \mathbf{v}) = 0, \tag{2.1}$$

(2) the equation of motion [equation (A.7)]

$$\rho \left[\frac{\partial \mathbf{v}}{\partial t} + (\mathbf{v} \cdot \nabla)\, \mathbf{v} \right] = -\nabla p + \rho \mathbf{g}, \tag{2.2}$$

and (3) the equation of energy [equation (A.18)]

$$\frac{\partial \epsilon}{\partial t} + \mathrm{div}(\epsilon + p)\mathbf{v} = \rho \mathbf{v} \cdot \mathbf{g}. \tag{2.3}$$

Occasionally barotropic relation $p = P(\rho)$ substitutes the energy equation (2.3). Especially polytropic relation $p = K\rho^{\Gamma}$ is often used on behalf of the energy equation. In the case that the gas is isothermal or isentropic, the polytropic relations of

$$p = c_{is}^2 \rho \quad \text{(isothermal)} \tag{2.4}$$

and

$$p = c_s^2 \rho^{\gamma} \quad \text{(isentropic)} \tag{2.5}$$

are substitution to equation (2.3). [We can replace equation (2.3) with equations (2.4) and (2.5).]

2.2 The Poisson Equation of the Self-Gravity

In this section, we will show the basic equation describing how the gravity works. First, compare the gravity and the static electric force. Consider the electric field formed by a point charge Q at a distance r from the point source as

$$E = \frac{1}{4\pi\epsilon_0} \frac{Q}{r^2}, \tag{2.6}$$

where ϵ_0 is the electric permittivity of the vacuum. On the other hand, the gravitational acceleration by the point mass of M at the distance r from the point mass is written down as

$$g = -G \frac{M}{r^2}, \tag{2.7}$$

where $G = 6.67 \times 10^{-8}\mathrm{kg}^{-1}\,\mathrm{m}^3\,\mathrm{s}^{-2}$ is the gravitational constant. Comparing these two, replacing Q with M and at the same time $1/4\pi\epsilon_0$ to $-G$ these equations (2.6) and (2.7) are identical with each other.

The Gauss theorem for electrostatic field as

$$\mathrm{div}\,\mathbf{E} = \frac{\rho_e}{\epsilon_0}, \tag{2.8}$$

and another expression using the electrostatic potential ϕ_e as

$$\nabla^2\phi_e = -\frac{\rho_e}{\epsilon_0}, \tag{2.9}$$

lead to the equations for the gravity as

$$\mathrm{div}\,\mathbf{g} = -4\pi G\rho, \tag{2.10}$$

and

$$\nabla^2\phi = 4\pi G\rho, \tag{2.11}$$

where ρ_e and ρ represent the electric charge density and the mass density. Equation (2.11) is called the Poisson equation for the gravitational potential and describes how the potential ϕ is determined from the mass density distribution ρ.

Problem

Consider a spherical symmetric density distribution. Using the Poisson equation, obtain the potential (ϕ) and the gravitational acceleration (g) for a density distribution shown below.

$$\rho\begin{cases} = \rho_0 & \text{for } r < R \\ = 0 & \text{for } r \geq R \end{cases}$$

Hint: The Poisson equation (2.11) for the spherical symmetry is

$$\frac{1}{r^2}\frac{\partial}{\partial r}\left(r^2\frac{\partial\phi}{\partial r}\right) = 4\pi G\rho.$$

2.3 Free-fall Time

If the pressure force can be neglected in the equation of motion (A.1), the gravitational one remains. Assuming the spherical symmetry, consider the gravity $g_r(r)$ at the position of radial distance from the center being equal to r. Using the Gauss' theorem, g_r is related to the mass inside of r, which is expressed by the equation

$$M_r = \int_0^r \rho 4\pi r^2 dr, \tag{2.12}$$

and g_r is written as

$$g_r(r) = -\frac{GM_r}{r^2}. \tag{2.13}$$

This leads to the equation motion for a cold gas under the control of the self-gravity is written

$$\frac{d^2r}{dt^2} = -\frac{GM_r}{r^2}. \tag{2.14}$$

Analyzing the equation is straightforward, multiplying dr/dt gives

$$\frac{dv^2/2}{dt} = +\frac{d}{dt}\left(\frac{GM_r}{r}\right), \tag{2.15}$$

which leads to the conservation of mechanical energy as

$$\frac{1}{2}\left(\frac{dr}{dt}\right)^2 - \frac{GM_r}{r} = E, \tag{2.16}$$

in which E represents the total energy of the pressureless gas element and it is fixed from the initial condition. If the gas is static initially at the distance R, the energy is negative as

$$E = -\frac{GM_r(R)}{R}, \tag{2.17}$$

because at $t = 0$, $r = R$ and $dr/dt = 0$.

The solutions of equation (2.16) are well known as follows:

1. the case of negative energy $E < 0$. Considering the case that the gas sphere is inflowing $v < 0$, equation (2.16) becomes

$$\frac{dr}{dt} = -\left[2GM_r(R)\right]^{1/2}\left(\frac{1}{r} - \frac{1}{R}\right)^{1/2}, \tag{2.18}$$

where we assumed initially $dr/dt = 0$ at $r = R$. Using a parameter $\eta(t)$, the radius of the gas element at some epoch t is written

$$r = R\cos^2\eta. \tag{2.19}$$

In this case, equation (2.18) reduces to

$$\cos^2\eta\frac{d\eta}{dt} = \left(\frac{GM_r(R)}{2R^3}\right)^{1/2}. \tag{2.20}$$

This gives us the expression of t as

$$t = \left(\frac{R^3}{2GM_r(R)}\right)^{1/2}\left(\eta + \frac{\sin 2\eta}{2}\right). \tag{2.21}$$

This corresponds to the closed universe in the cosmic expansion ($\Omega_0 < 1$).

2. if the energy is equal to zero, the solution of equation (2.16) is written as

$$\left(r^{3/2} - R^{3/2}\right)^{2/3} = \left(\frac{9GM_r(R)}{2}\right)^{1/3} t^{2/3}, \tag{2.22}$$

where $R = r(t = 0)$.

[**Problem**] solve equation (2.16) and obtain (2.22).

3. If $E > 0$, the expansion law is given by

$$t = \left(\frac{R^2}{2E}\right)^{1/2}\left(\frac{\dot{R}^2 R}{2GM_r(R)}\right)^{-1}\left(\frac{\sinh 2\eta}{2} - \eta\right) \tag{2.23}$$

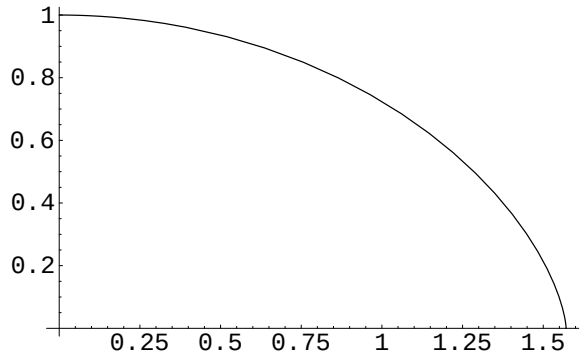

Figure 2.1: Free-fall. x-axis and y-axis represent $\cos^2\eta$ and $\eta + \sin 2\eta/2$.

and

$$x = \left(\frac{E}{GM_r(R)}\right) r = \sinh^2\eta, \tag{2.24}$$

where E represents the total enerygy

$$E = \frac{\dot{R}^2}{2} - \frac{GM_r(R)}{R} > 0. \tag{2.25}$$

[**Problem**] solve equation (2.16) and obtain equations (2.23) and (2.24).

In the present case, at $t = 0$, since $dr/dt = 0$ the energy is negative. Equation (2.19) shows us r becomes equal to zero (the gas collapses) if $\eta = \pi/2$ as well as $\eta = 0$ at $t = 0$. Equation (2.21) indicates it occurs at the epoch of

$$\begin{aligned} t = t_{\rm ff} &= \left(\frac{R^3}{2GM_r(R)}\right)^{1/2} \frac{\pi}{2}, \\ &= \left(\frac{3\pi}{32G\bar{\rho}}\right)^{1/2}, \end{aligned} \tag{2.26}$$

where $\bar{\rho}$ represents the average density inside of r, that is $M_r/(4\pi r^3/3)$. This is called "**free-fall time**' of the gas. This gives the time-scale for the gas with density $\bar{\rho}$ to collapse. In the actual interstellar space, the gas pressure is not negligible. However, $t_{\rm ff}$ gives a typical time-scale for a gas cloud to collapse and to form stars in it.

2.3.1 Accretion Rate

Equation 2.26 indicates that the gas shell with a large $\bar{\rho}$ reaches the center earlier than that with a small $\bar{\rho}$. Imediately, this means a spherical cloud with a uniform density ρ_0 contracts uniformly and all the mass reaches the center at $t = t_{\rm ff} = (3\pi/32G\rho_0)^{1/2}$. In this case, the mass accretion rate to a central source becomes infinity. In contrast, consider a cloud whose density gradually decreases outwardly. In this case, the outer mass shell has smaller $\bar{\rho}$ than the inner mass shell. Therefore even when the inner mass shell collapses and reaches the center, the outer mass shell are contracting and does not reach the center. This gives a smaller mass accretion rate than a uniform cloud. If the gas pressure is neglected, the accretion rate is determined by the initial spatial distribution of the density. We will compare the accretion rate derived here with results of hydrodynamical calculation in §4.4

2.4 Gravitational Instability

Here, we will study a typical size where the self-gravity play an important role and form density inhomogeneities — the Jean wavelength.

Linear Analysis

Consider a uniform gas with density ρ_0 and pressure p_0 without motion $\mathbf{u}_0 = 0$. In this uniform gas distribution, we assume small perturbations. As a result, the distributions of the density, the pressure and the velocity are perturbed from the uniform ones as

$$\rho = \rho_0 + \delta\rho, \tag{2.27}$$

$$p = p_0 + \delta p, \tag{2.28}$$

and

$$\mathbf{u} = \mathbf{u}_0 + \delta\mathbf{u} = \delta\mathbf{u}, \tag{2.29}$$

where the amplitudes of perturbations are assumed much small, that is, $|\delta\rho|/\rho_0 \ll 1$, $|\delta p|/p_0 \ll 1$ and $|\delta\mathbf{u}|/c_s \ll 1$. We assume the variables changes only in the x-direction. In this case the basic equations for isothermal gas are

$$\frac{\partial\rho}{\partial t} + \frac{\partial\rho u}{\partial x} = 0, \tag{2.30}$$

$$\rho\left(\frac{\partial u}{\partial t} + u\frac{\partial u}{\partial x}\right) = -\frac{\partial p}{\partial x} + \rho g_x, \tag{2.31}$$

and

$$p = c_{is}^2\rho, \tag{2.32}$$

where u and g_x represent the x-component of the velocity and that of the gravity, respectively.

Using equations (2.27), (2.28), and (2.29), equation (2.30) becomes

$$\frac{\partial\rho_0 + \delta\rho}{\partial t} + \frac{\partial(\rho_0 + \delta\rho)(u_0 + \delta u)}{\partial x} = 0. \tag{2.33}$$

Noticing that the amplitudes of variables with and without δ are completely different, two equations are obtained from equation(2.33) as

$$\frac{\partial\rho_0}{\partial t} + \frac{\partial\rho_0 u_0}{\partial x} = 0, \tag{2.34}$$

$$\frac{\partial\delta\rho}{\partial t} + \frac{\partial\rho_0\delta u + \delta\rho u_0}{\partial x} = 0, \tag{2.35}$$

where the above is the equation for unperturbed state and the lower describes the relation between the quantities with δ. Equation (2.34) is automatically satisfied by the assumption of uniform distribution. In equation (2.35) the last term is equal to zero. Equation of motion

$$(\rho_0 + \delta\rho)\left(\frac{\partial u_0 + \delta u}{\partial t} + (u_0 + \delta u)\frac{\partial u_0 + \delta u}{\partial x}\right) = -\frac{\partial p_0 + \delta p}{\partial x} + (\rho_0 + \delta\rho)\frac{\partial\phi_0 + \delta\phi}{\partial x}, \tag{2.36}$$

gives the relationship between the terms containing only **one** variable with δ as follows:

$$\rho_0\frac{\partial\delta u}{\partial t} = -\frac{\partial\delta p}{\partial x} - \rho_0\frac{\partial\delta\phi}{\partial x}. \tag{2.37}$$

The perturbations of pressure and density are related with each other as follows: for the isothermal gas

$$\frac{\delta p}{\delta \rho} = \left(\frac{\partial p}{\partial \rho}\right)_T = \frac{p_0}{\rho_0} = c_{is}^2, \tag{2.38}$$

and for isentropic gas

$$\frac{\delta p}{\delta \rho} = \left(\frac{\partial p}{\partial \rho}\right)_{\rm ad} = \gamma \frac{p_0}{\rho_0} = c_s^2. \tag{2.39}$$

2.4.1 Sound Wave

If the self-gravity is ignorable, equations(2.35)

$$\frac{\partial \delta\rho}{\partial t} + \rho_0 \frac{\partial \delta u}{\partial x} = 0, \tag{2.40}$$

and equations(2.37)

$$\rho_0 \frac{\partial \delta u}{\partial t} = -c_{is}^2 \frac{\partial \delta\rho}{\partial x}, \tag{2.41}$$

where we assumed the gas is isothermal. These two equations describe the propagation and growth of perturbations. If the gas acts adiabatically, replace c_{is} with c_s.

Making $\frac{\partial}{\partial x}\times$(2.40) and $\frac{\partial}{\partial t}\times$(2.41) vanishes $\delta\rho$ and we obtain

$$\frac{\partial^2 \delta u}{\partial t^2} - c_{is}^2 \frac{\partial^2 \delta u}{\partial x^2} = 0. \tag{2.42}$$

Since this leads to

$$\frac{\partial \delta u}{\partial t} - c_{is} \frac{\partial \delta u}{\partial x} = 0, \tag{2.43}$$

$$\frac{\partial \delta u}{\partial t} + c_{is} \frac{\partial \delta u}{\partial x} = 0, \tag{2.44}$$

equation (2.42) has a solution that a wave propagates with a phase velocity of $\pm c_s$. Since the displacement ($\propto \delta u$) is parallel to the propagation direction x, and the restoring force comes from the pressure, this seems **the sound wave**.

Problem

Interstellar gas contains mainly Hydrogen and Helium, whose number ratio is approximately 10:1. Obtain the value of average molecular weight for the fully ionized interstellar gas with temperature $T = 10^4$K (components are ionized H^+ (HII) and He^{+2} (HeIII) and electron e^{-1}). How about the molecular gas ($T = 10$K) containing molecular H_2, neutral He (HeI) and no electron.

2.5 Jeans Instability

Sound wave seems to be modified in the medium where the self-gravity is important. Beside the continuity equation (2.35)

$$\frac{\partial \delta\rho}{\partial t} + \rho_0 \frac{\partial \delta u}{\partial x} = 0, \tag{2.45}$$

and the equation of motion (2.37)

$$\rho_0 \frac{\partial \delta u}{\partial t} = -c_{is}^2 \frac{\partial \delta\rho}{\partial x} - \rho_0 \frac{\partial \delta\phi}{\partial x}, \tag{2.46}$$

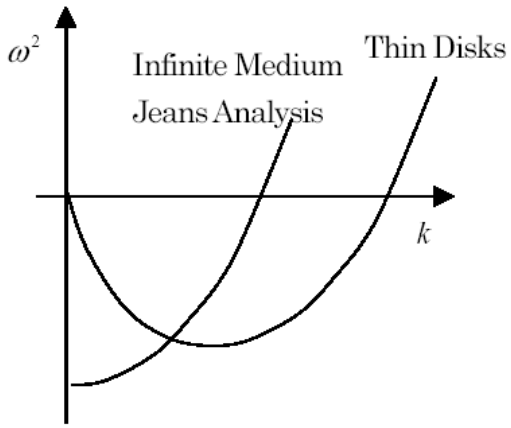

Figure 2.2: Dispersion Relation

the linearized Poisson equation

$$\frac{\partial^2 \delta\phi}{\partial x^2} = 4\pi G \delta\rho, \tag{2.47}$$

should be included. $\frac{\partial}{\partial x}\times$eq.(2.46) gives

$$\rho_0 \left(\frac{\partial^2 \delta u}{\partial x \partial t} \right) = -c_{is}^2 \frac{\partial^2 \delta\rho}{\partial x^2} - 4\pi G \rho_0 \delta\rho. \tag{2.48}$$

where we used equation (2.47) to eliminate $\delta\phi$. This yields

$$\frac{\partial^2 \delta\rho}{\partial t^2} = c_{is}^2 \frac{\partial^2 \delta\rho}{\partial x^2} + 4\pi G \rho_0 \delta\rho. \tag{2.49}$$

where we used $\frac{\partial}{\partial t}\times$eq(2.45).

This is the equation which characterizes the growth of density perturbation owing to the self-gravity. Here we consider the perturbation are expressed by the linear combination of plane waves as

$$\delta\rho(x,t) = \sum A(\omega,k) \exp(i\omega t - ikx), \tag{2.50}$$

where k and ω represent the wavenumber and the angular frequency of the wave. Picking up a plane wave and putting into equation (2.49), we obtain **the dispersion relation** for the gravitational instability as

$$\omega^2 = c_{is}^2 k^2 - 4\pi G \rho_0. \tag{2.51}$$

Reducing the density to zero, the equation gives us the same dispersion relation as that of sound wave as $\omega/k = c_{is}$. For short waves ($k \gg k_J = (4\pi G\rho_0)^{1/2}/c_{is}$), since $\omega^2 > 0$ the wave is ordinary oscillatory wave. Increasing the wavelength (decreasing the wavenumber), ω^2 becomes negative for $k < k_J = (4\pi G\rho_0)^{1/2}/c_{is}$. For negative ω^2, ω can be written $\omega = \pm i\alpha$ using a positive real α. In this case, since $\exp(i\omega t) = \exp(\mp\alpha t)$, the wave which has $\omega = -i\alpha$ increases its amplitude exponentially. This means that even if there are density inhomogeneities only with small amplitudes, they grow in a time scale of $1/\alpha$ and form the density inhomogeneities with large amplitudes.

The critical wavenumber

$$k_J = (4\pi G\rho_0)^{1/2}/c_{is} \tag{2.52}$$

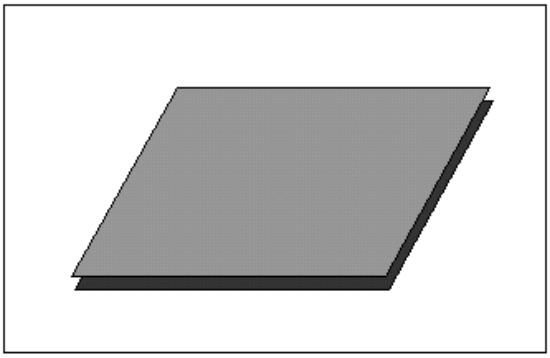

Figure 2.3: Thin disk.

corresponds to the wavelength

$$\lambda_J = \frac{2\pi}{k_J} = \left(\frac{\pi c_{is}^2}{G\rho_0}\right)^{1/2}, \tag{2.53}$$

which is called the Jeans wavelength. Ignoring a numerical factor of the order of unity, it is shown that the Jeans wavelength is approximately equal to the free-fall time scale (eq.2.26) times the sound speed. The short wave with $\lambda \ll \lambda_J$ does not suffer from the self-gravity. For such a scale, the analysis we did in the preceding section is valid.

Typical values in molecular clouds, such as $c_{is} = 200\mathrm{m\,s^{-1}}$, $\rho_0 = 2 \times 10^{-20}\mathrm{g\,cm^{-3}}$, give us the Jeans wavelength as $\lambda_J = 1.7 \times 10^{18}\mathrm{cm} = 0.56\mathrm{pc}$. The mass contained in a sphere with a radius $r = \lambda_J/2$ is often called Jeans mass, which gives a typical mass scale above which the gas collapses. Typical value of the Jeans mass is as follows

$$M_J \simeq \frac{4\pi}{3}\rho_0\left(\frac{\lambda_J}{2}\right)^3 = \frac{\pi}{6}\left(\frac{\pi}{G\rho_0}\right)^{3/2} c_{is}^3\rho_0. \tag{2.54}$$

Using again the above typical values in the molecular clouds, $c_{is} = 200\mathrm{m\,s^{-1}}$, $\rho_0 = 2 \times 10^{-20}\mathrm{g\,cm^{-3}}$, the Jeans mass of this gas is equal to $M_J \simeq 27M_\odot$.

2.6 Gravitational Instability of Thin Disk

Disks are common in the Universe. Spiral and barred spiral galaxies have disks where stars are formed. In more small scale, gas and dust disks are often found around protostars. Moreover, the disk may become a proto-planetary disk. It is valuable to study how the self-gravity works in such thin structures. Here, we assume a thin disk extending in x- and y-directions whose surface density is equal to $\sigma = \int_{-\infty}^{\infty}\rho dz$, in other word the density is written using the Dirac's delta function $\delta(z)$ as

$$\rho(x, y, z) = \sigma(x, y)\delta(z). \tag{2.55}$$

Integrating along the z-direction basic equations (2.45), (2.46), and (2.47), the linearized basic equations for the thin disk are as follows:

$$\frac{\partial\delta\sigma}{\partial t} + \sigma_0\frac{\partial\delta u}{\partial x} = 0, \tag{2.56}$$

$$\sigma_0\frac{\partial\delta u}{\partial t} = -c_{is}^2\frac{\partial\delta\sigma}{\partial x} - \sigma_0\frac{\partial\delta\phi}{\partial x}, \tag{2.57}$$

$$\frac{\partial^2 \delta\phi}{\partial x^2} + \frac{\partial^2 \delta\phi}{\partial z^2} = 4\pi G \delta\sigma \delta(z), \tag{2.58}$$

where we assumed $\sigma = \sigma_0 + \delta\sigma$, $u = \delta u$, $\phi = \phi_0 + \delta\phi$ and took the first order terms (those contain only one δ).

Outside the disk, the rhs of equation (2.58) is equal to zero. It reduces to the Laplace equation

$$\frac{\partial^2 \delta\phi}{\partial x^2} + \frac{\partial^2 \delta\phi}{\partial z^2} = 0. \tag{2.59}$$

Taking a plane wave of

$$\delta X(x,t) = \delta A \exp(i\omega t - ikx), \tag{2.60}$$

equation (2.59) is reduced to

$$\frac{\partial^2 \delta\phi}{\partial z^2} - k^2 \delta\phi = 0. \tag{2.61}$$

This has a solution which does not diverge at the infinity $z = \pm\infty$ as

$$\delta\phi = \delta\phi(z=0)\exp(-k|z|). \tag{2.62}$$

On the other hand, integrating equation (2.58) from $z = -0$ to $z = +0$ or in other word, applying the Gauss' theorem to the region containing the $z = 0$ surface, it is shown that the gravity $\delta g_z = -\partial\delta\phi/\partial z$ has a jump crossing the $z = 0$ surface as

$$\left.\frac{\partial \delta\phi}{\partial z}\right|_{z=+0} - \left.\frac{\partial \delta\phi}{\partial z}\right|_{z=-0} = 4\pi G \delta\sigma. \tag{2.63}$$

Equations (2.62) and (2.63) lead a final form of the potential as

$$\delta\phi = -\frac{2\pi G \delta\sigma}{k} \exp(-k|z|). \tag{2.64}$$

Putting this to equations (2.57), and using equations (2.56) and (2.57), we obtain the dispersion relation for the gravitational instability in a thin disk as

$$\omega^2 = c_{is}^2 k^2 - 2\pi G \sigma_0 k. \tag{2.65}$$

This reduces to the dispersion relation of the sound wave for the short wave $k \gg 2\pi G\sigma_0/c_{is}^2$. While for a longer wave than $\lambda_{cr} = c_{is}^2/G\sigma_0$, an exponential growth of $\delta\sigma$ is expected. The dispersion relation is shown in Fig.2.2.

2.7 Super- and Subsonic Flow

Flow whose velocity is faster than the sound speed is called supersonic, while that slower than the sound speed is called subsonic. The subsonic and supersonic flows are completely different.

2.7.1 Flow in the Laval Nozzle

Consider a tube whose cross-section, $S(x)$, changes gradually, which is called Laval nozzle. Assuming the flow is steady $\partial/\partial t = 0$ and is essentially one-dimensional, the continuity equation (2.1) is rewritten as

$$\rho u S = \text{constant}, \tag{2.66}$$

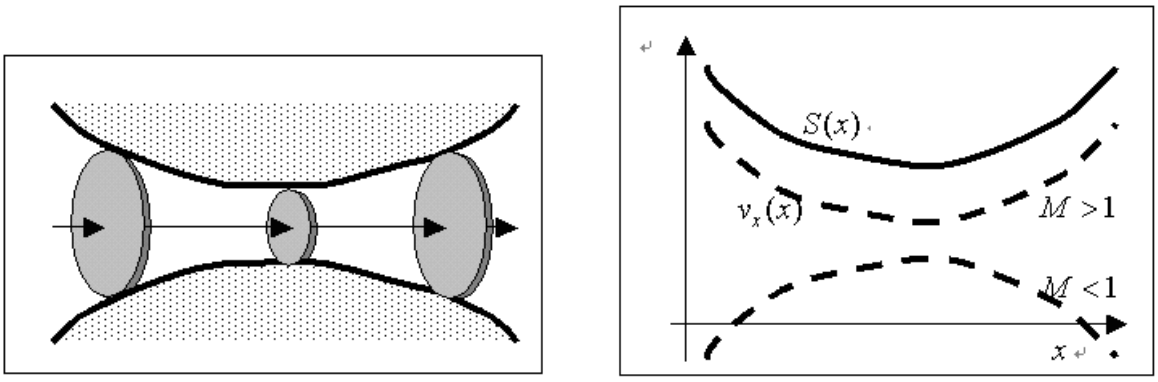

Figure 2.4: *Left:* Explanation of Laval nozzle. *Right:* The relation between the cross-section $S(x)$ and the flow velocity v_x.

or

$$\frac{1}{\rho}\frac{\partial \rho}{\partial x} + \frac{1}{u}\frac{\partial u}{\partial x} + \frac{1}{S}\frac{\partial S}{\partial x} = 0. \tag{2.67}$$

Equation of motion (2.2) becomes

$$u\frac{\partial u}{\partial x} = -\frac{1}{\rho}\frac{\partial p}{\partial x} = -\frac{c_s^2}{\rho}\frac{\partial \rho}{\partial x}, \tag{2.68}$$

where we used the relationship of

$$\frac{\partial p}{\partial x} = \left(\frac{\partial p}{\partial \rho}\right)_s \frac{\partial \rho}{\partial x} = c_s^2 \frac{\partial \rho}{\partial x}. \tag{2.69}$$

When the flow is isothermal, use the isothermal sound speed c_{is}^2 instead of the adiabatic one. From equations (2.67) and (2.68), we obtain

$$\left(\frac{u^2}{c_s^2} - 1\right)\frac{1}{u}\frac{\partial u}{\partial x} = \frac{1}{S}\frac{\partial S}{\partial x}, \tag{2.70}$$

where the factor $\mathcal{M} = u/c_s$ is called **the Mach number**. For supersonic flow $\mathcal{M} > 1$, while $\mathcal{M} < 1$ for subsonic flow.

In the supersonic regime $\mathcal{M} > 1$, the factor in the parenthesis of the lhs of equation (2.69) is positive. This leads to the fact that the velocity increases ($du/dx > 0$) as long as the cross-section increases ($dS/dx > 0$). On the other hand, in the subsonic regime, the velocity decreases ($du/dx < 0$) while the cross-section increases ($dS/dx > 0$). See right panel of 2.4.

If $\mathcal{M} = 1$ at the point of minimum cross-section (throat), two curves for $\mathcal{M} < 1$ and $\mathcal{M} > 1$ have an intersection. In this case, gas can be accelerated through the Laval nozzle. First, a subsonic flow is accelerated to the sonic speed at the throat of the nozzle. After passing the throat, the gas follows the path of a supersonic flow, where the velocity is accelerated as long as the cross-section increases.

2.7.2 Steady State Flow under an Influence of External Fields

Consider the flow under the force exerted on the gas whose strength varies spatially. Let $g(x)$ represent the force working per unit mass. Assuming the cross-section is constant

$$\rho u = \text{constant}, \tag{2.71}$$

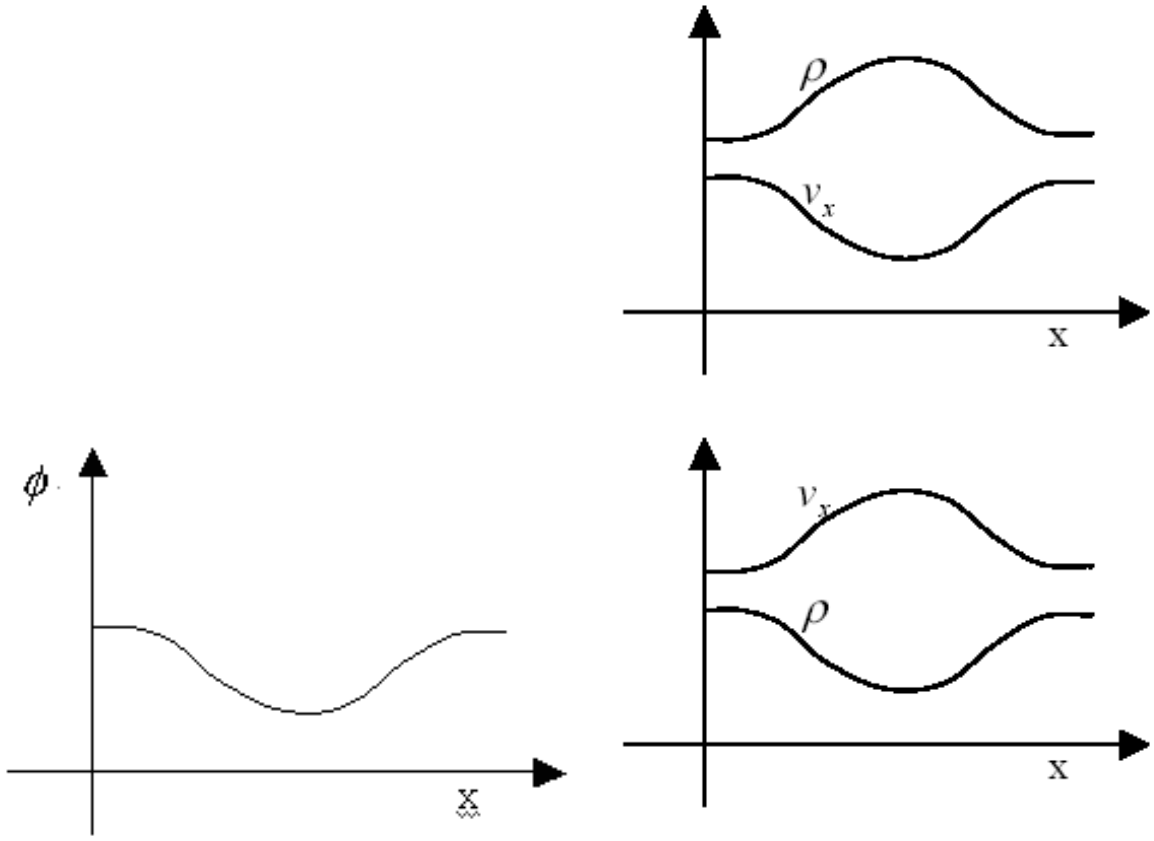

Figure 2.5: *Left:* External field potential. *Right:* Velocity and density variations. Gas flows in the external field whose potential is shown in the left panel. The upper panel represents a subsonic flow. The lower panel does a supersonic flow.

immediately we have

$$\frac{1}{\rho}\frac{\partial \rho}{\partial x} + \frac{1}{u}\frac{\partial u}{\partial x} = 0. \tag{2.72}$$

On the other hand, the equation motion is

$$u\frac{\partial u}{\partial x} = -\frac{c_s^2}{\rho}\frac{\partial \rho}{\partial x} + g(x), \tag{2.73}$$

From equations (2.72) and (2.73), we obtain

$$\left(\frac{u^2}{c_s^2} - 1\right)\frac{1}{u}\frac{\partial u}{\partial x} = \frac{g(x)}{c_s^2}. \tag{2.74}$$

Consider an external field whose potential is shown in Fig.2.5(*Left*). (1) For subsonic flow, the factor in the parenthesis is negative. Before the potential minimum, since $g(x) > 0$, u is decelerated. On th other hand, after the potential minimum, u is accelerated owing to $g(x) < 0$. Using equation (2.71), this leads to a density distribution in which density peaks near the potential minimum. (2) For supersonic flow, the factor is positive. In the region of $g(x) > 0$, u is accelerated. After passing the potential minimum, u is decelerated. The velocity and the density distribution is shown in Fig.2.5(right-lower panel).

The density distribution of the subsonic flow in an external potential is similar to that of hydrostatic one. That is, considering the hydrostatic state in an external potential, the gas density peaks at the potential minimum. On the other hand, The density distribution of the supersonic flow looks like that made by ballistic particles which are moving freely in the potential. Owing to the conservation of the total energy (kinetic + potential energies), the velocity peaks at the density minimum. And the condition of mass conservation leads to the distribution in which the density decreases near the potential minimum.

2.7.3 Stellar Wind — Parker Wind Theory

Stellar winds are observed around various type of stars. Early type (massive) stars have large luminosities; the photon absorbed by the bound-bound transition transfers its outward momentum to the gas. This line-driven mechanism seems to work around the early type stars. On the other hand, acceleration mechanism of less massive stars are thought to be related to the coronal activity or dust driven mechanism (dusts absorb the emission and obtain outward momentum from the emission).

Here, we will see the identical mechanism in §2.7.1 and §2.7.2 works to accelerate the wind from a star. Consider a steady state and ignore $\partial/\partial t = 0$. The continuity equation (2.1) gives

$$r^2 \rho u = \text{const}, \tag{2.75}$$

where we used

$$\text{div}\rho\mathbf{v} = \frac{1}{r^2}\frac{\partial}{\partial r}\left(r^2 \rho u\right). \tag{2.76}$$

This leads to

$$\frac{2}{r} + \frac{1}{r}\frac{\partial \rho}{\partial r} + \frac{1}{u}\frac{\partial u}{\partial r} = 0. \tag{2.77}$$

The equation of motion (2.2) is as follows:

$$u\frac{\partial u}{\partial r} = -\frac{c_s^2}{\rho}\frac{\partial \rho}{\partial r} - \frac{GM_*}{r^2}, \tag{2.78}$$

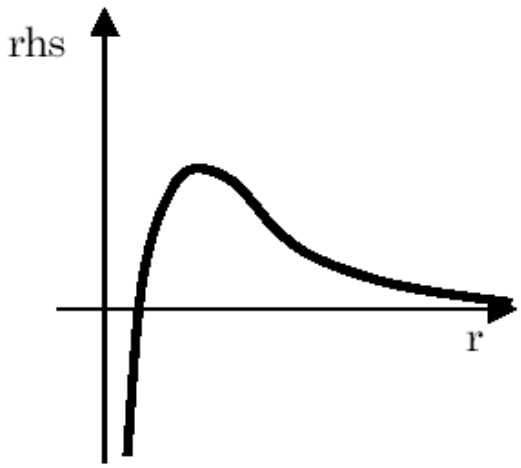

Figure 2.6: Right-hand side of equation (2.79) is plotted against the distance from the center r.

where we used $g = -GM_*/r^2$ (M_* means the mass of the central star). From these two equations (2.77) and (2.78) we obtain

$$\left(\mathcal{M}^2 - 1\right)\frac{1}{u}\frac{\partial u}{\partial r} = \frac{2}{r} - \frac{GM_*}{c_s^2}\frac{1}{r^2}, \tag{2.79}$$

where $\mathcal{M}$ represents the Mach number of the radial velocity. Take notice that this is similar to equations (2.70) and (2.74). That is, the fact that the rhs of equation (2.79) is positive corresponds to increasing the cross-section $dS/dx > 0$. On the contrary, when the rhs is negative, the fluid acts as the cross-section S is decreasing.

For simplicity, we assume the gas is isothermal. The rhs of equation (2.79) varies shown in Figure 2.6. Therefore, near to the star, the flow acts as the cross-section of nozzle is decreasing and far from the star it does as the cross-section is increasing. This is the same situation that the gas flows through the Laval nozzle.

Using a normalized distance $x \equiv r/(GM_*/2c_{is}^2)$, equation (2.79) becomes

$$\left(M^2 - 1\right)\frac{1}{\mathcal{M}}\frac{\partial \mathcal{M}}{\partial x} = \frac{2}{x} - \frac{2}{x^2}. \tag{2.80}$$

This is rewritten as

$$\frac{d}{dx}\left(\frac{\mathcal{M}^2}{2} - \log\mathcal{M} - 2\log x - \frac{2}{x}\right) = 0, \tag{2.81}$$

we obtain the solution of equation (2.80) as

$$\mathcal{M}^2 - 2\log\mathcal{M} = 4\log x + \frac{4}{x} + C. \tag{2.82}$$

This gives how the Mach number $\mathcal{M}$ varies changing x. To explore this, we define two functions:

$$f(\mathcal{M}) = 2\mathcal{M}^2 - 2\log\mathcal{M} \tag{2.83}$$

is a function only depending on $\mathcal{M}$ and

$$g(x) = 4\log x + \frac{4}{x} + C \tag{2.84}$$

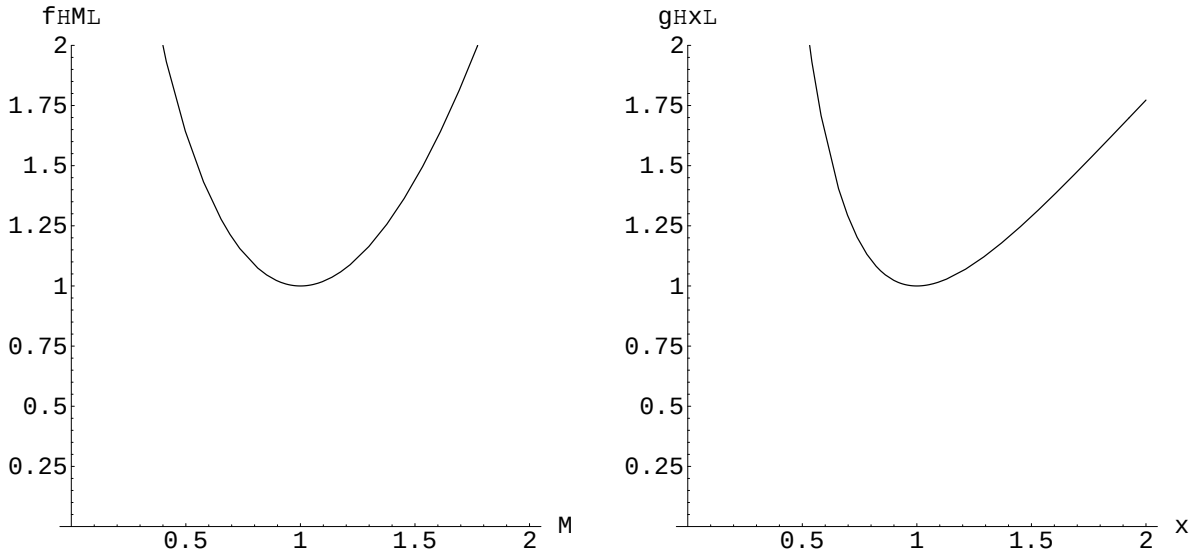

Figure 2.7: $f(\mathcal{M})$ (*left*) and $g(x)$ for $C = -3$ (*right*)

is a function only depending on x.

Since the minima of $f(\mathcal{M})$ and $g(x)$ are respectively 1 and $C + 4$, the permitted region in $(x, \mathcal{M})$ changes for values of C.

1. If $C = -3$, for all values of $x > 0$ there exist $\mathcal{M}$ which satisfies $f(\mathcal{M}) = g(x)$. This corresponds to the two curves which pass through a critical X-point of $(x, \mathcal{M}) = (1, 1)$ in Figure 2.8.

2. If $C < -3$, the minimum of $g(x)$ is smaller than that of $f(\mathcal{M})$. In this case, for x where $g(x) < 1 = \min(f(\mathcal{M}))$, there is no solution. Thus, $f(\mathcal{M}) = g(x)$ has solutions for $x < x_1$ and $x > x_2$, where $x_1 < x_2$, and $g(x_1) = g(x_2) = 1$. This corresponds to the curves running perpendicularly in Figure 2.8.

3. If $C > -3$, the minimum of $f(\mathcal{M})$ is smaller than that of $g(x)$. In this case, $f(\mathcal{M}) = g(x)$ has solutions for $\mathcal{M} < \mathcal{M}_1$ and $\mathcal{M} > \mathcal{M}_2$, where $\mathcal{M}_1 < \mathcal{M}_2$, and $f(\mathcal{M}_1) = f(\mathcal{M}_2) = C + 4$. This corresponds to curves running horizontally in Figure 2.8.

Out of the two solutions of $C = -3$, a wind solution is one with increasing $\mathcal{M}$ while departing from the star. This shows us the outflow speed is slow near the star but it is accelerated and a supersonic wind blows after passing the critical point. Since the equations are unchanged even if we replace u with $-u$, the above solution is valid for an accreting flow $u < 0$. Considering such a flow, the solution running from the lower-right corner to the upper-left corner represents the accretion flow, in which the inflow velocity is accelerated reaching the star and finally accretes on the star surface with a supersonic speed.

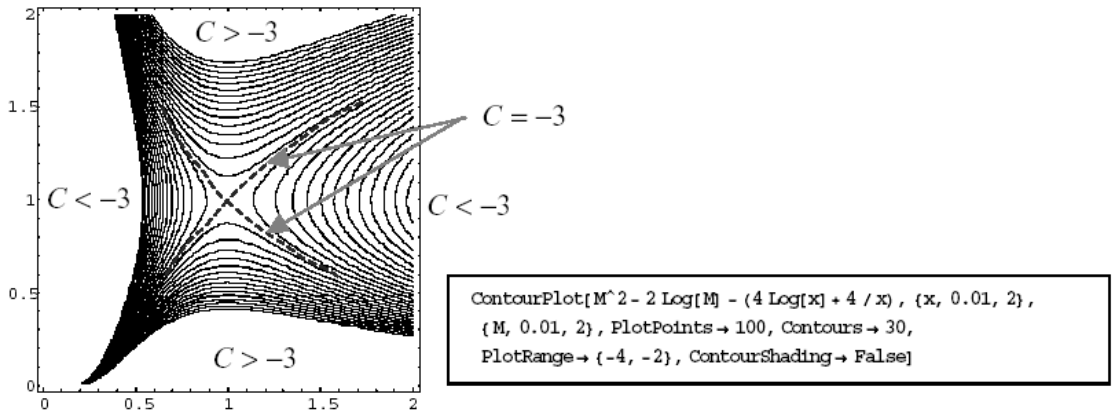

Figure 2.8: $\mathcal{M}$ vs x (the x-axis is the normalized distance from the center $x \equiv r/(GM_*/2c_{is}^2)$ and the y-axis is the Mach number $\mathcal{M}$.)

Chapter 3

Galactic Scale Star Formation

3.1 Schmidt Law

Schmidt (1959) speculated that the star formation rate is proportional to a power of the surface density of the interstellar medium

$$\dot{\Sigma}_{\rm SF} \propto \Sigma_{\rm gas}^{n}, \tag{3.1}$$

where the power n seems between 1 and 2 around the solar vicinity. If $n = 2$, the star formation rate is thought to be determined by the collision rate of interstellar clouds. At that time Schmidt showed us $n \simeq 2$. On the other hand, if the gas passing through the galactic arms forms stars, the star formation rate seems proportional to the gas surface density and the arm-to-arm period. Thus this predicts $n = 1$.

3.1.1 Global Star Formation

The star formation rate is estimated by the intensity of Hα emission (Kennicutt, Tamblyn, & Congdon 1994) as

$$\mathrm{SFR}(M_\odot \mathrm{yr}^{-1}) = \frac{L(\mathrm{H}\alpha)}{1.26 \times 10^{41} \mathrm{erg\ s}^{-1}}, \tag{3.2}$$

which is used for normal galaxies. While in **the starburst galaxies** which show much larger star formation rate than the normal galaxies, FIR luminosity seems a better indicator of star formation rate

$$\mathrm{SFR}(M_\odot \mathrm{yr}^{-1}) = \frac{L(\mathrm{FIR})}{2.2 \times 10^{43} \mathrm{erg\ s}^{-1}} = \frac{L(\mathrm{FIR})}{5.8 \times 10^{9} L_\odot}. \tag{3.3}$$

Kennicutt (1998) summarized the relation between SFRs and the surface gas densities [Fig.3.1 (left)] for 61 normal spiral and 36 infrared-selected starburst galaxies. As seen in Fig.3.1, the star formation rate averaged over a galaxy ($\Sigma_{\rm SFR}(M_\odot\ \mathrm{yr}^{-1}\,\mathrm{kpc}^{-2})$), which is called the global star formation rate, is well correlated to the average gas surface density $\Sigma_{\rm gas}(M_\odot\ \mathrm{pc}^{-2})$. He gave the power of the global Schmidt law as $n = 1.4 \pm 0.15$. That is,

$$\Sigma_{\rm SFR} \simeq (1.5 \pm 0.7) \times 10^{-4} \left(\frac{\Sigma_{\rm gas}}{1 M_\odot\ \mathrm{kpc}^{-2}} \right)^{1.4 \pm 0.15} M_\odot\ \mathrm{yr}^{-1}\,\mathrm{pc}^{-2}. \tag{3.4}$$

The fact that the power is not far from 3/2 seems to be explained as follows: Star formation rate should be proportional to the gas density ($\Sigma_{\rm gas}$) but it should also be inversely proportional to the time scale of forming stars in respective gas clouds, which is essentially the free-fall time scale.

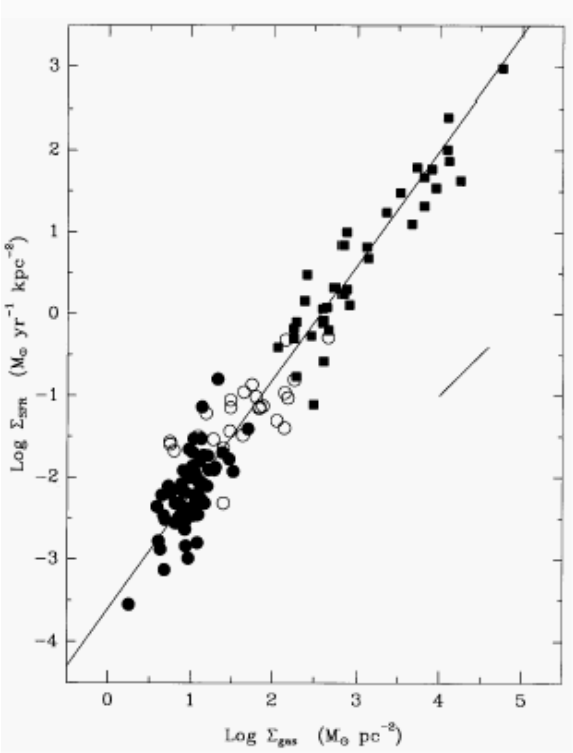

FIG. 6.—Composite star formation law for the normal disk (*filled circles*) and starburst (*squares*) samples. Open circles show the SFRs and gas densities for the centers of the normal disk galaxies. The line is a least-squares fit with index $N = 1.40$. The short, diagonal line shows the effect of changing the scaling radius by a factor of 2.

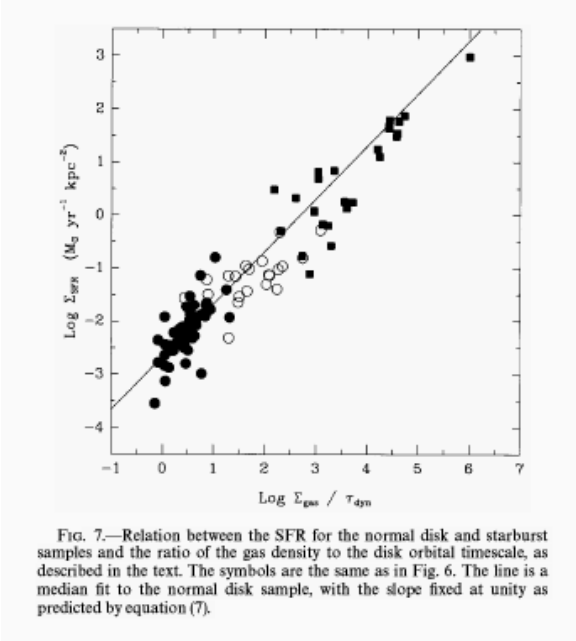

FIG. 7.—Relation between the SFR for the normal disk and starburst samples and the ratio of the gas density to the disk orbital timescale, as described in the text. The symbols are the same as in Fig. 6. The line is a median fit to the normal disk sample, with the slope fixed at unity as predicted by equation (7).

Figure 3.1: Taken from Figs.6 and 7 of Kennicutt (1998). Left: The x-axis means the total (HI+H_2) gas density and the y-axis does the global star formation rate. Right: The x-axis means the total (HI+H_2) gas density divided by the orbital time-scale. The y-axis is the same.

Remember the fact that the free-fall time given in equation (2.26) is proportional to $\tau_{\rm ff} \propto 1/(G\rho)^{1/2}$. Therefore

$$\rho_{\rm SFR} \propto \rho_{\rm gas} \times (G\rho_{\rm gas})^{1/2} \propto \rho_{\rm gas}^{3/2}, \tag{3.5}$$

where $\rho_{\rm gas}$ and $\rho_{\rm SFR}$ are the volume densities of gas and star formation.

He found another correlation between the quantity of gas surface density divided by the orbital period of galactic rotation and the star formation rate [Fig.3.1 (right)]. Although the actual slope is equal to 0.9 instead of 1, the correlation in Fig.3.1(right) is well expressed as

$$\Sigma_{\rm SFR} \simeq 0.017 \Sigma_{\rm gas} \Omega_{\rm gas} = 0.21 \frac{\Sigma_{\rm gas}}{\tau_{\rm arm-to-arm}}, \tag{3.6}$$

where $\Omega_{\rm gas}$ represents the angular speed of galactic rotation. This means that 21 % of the gas mass is processed to form stars per orbit. These two correlations [eqs (3.4) and (3.6)] implicitly ask another relation of $\Omega_{\rm gas} \propto \Sigma_{\rm gas}^{1/2}$.

3.1.2 Local Star Formation Rate

In Figure 3.2 (left), the correlation between star formation rate and gas density is plotted for specific galaxies (NGC 4254 and NGC 2841). This shows us that Hα surface brightness (star formation

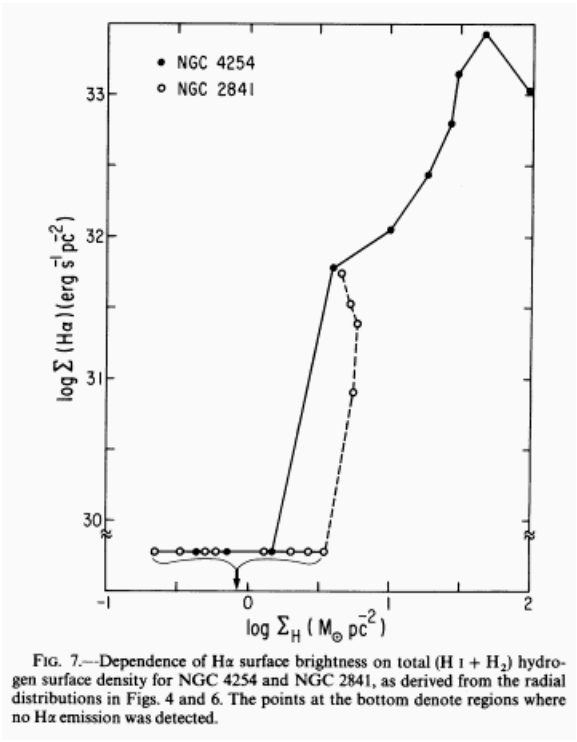

FIG. 7.—Dependence of Hα surface brightness on total (H I + H_2) hydrogen surface density for NGC 4254 and NGC 2841, as derived from the radial distributions in Figs. 4 and 6. The points at the bottom denote regions where no Hα emission was detected.

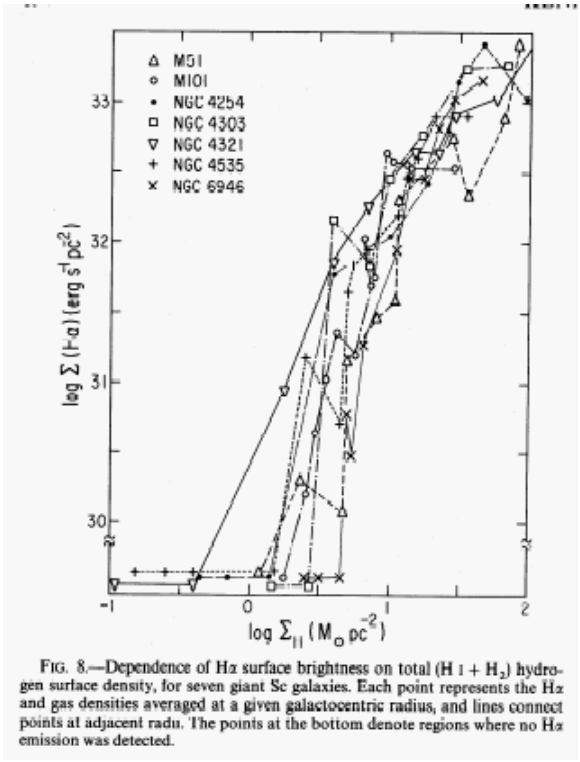

FIG. 8.—Dependence of Hα surface brightness on total (H I + H_2) hydrogen surface density, for seven giant Sc galaxies. Each point represents the Hα and gas densities averaged at a given galactocentric radius, and lines connect points at adjacent radii. The points at the bottom denote regions where no Hα emission was detected.

Figure 3.2: Distributions of $\Sigma_{\rm SF}$ and $\Sigma_{\rm gas}$. (*Left*:) Relation between $\Sigma_{\rm SF}$ and $\Sigma_{\rm gas}$ for an Sc galaxy NGC 4254 and an Sb galaxy NGC 2841. (*Right*:) Relation between $\Sigma_{\rm SF}$ and $\Sigma_{\rm gas}$ for various galaxies. These are taken from Figs.7 and 8 of Kennicutt (1989).

rate) and the gas column density are well correlated each other. Figure 3.2 (left) also indicates that there seems a critical gas density below which star formation is not observed. The value of this threshold column density is approximately $\simeq 4 M_\odot {\rm pc}^{-2}$ for both galaxies in Figure 3.2 (left). The same correlation is seen in other spiral galaxies [Fig.3.2(right)]. Fitting the correlation with a power-law, he obtained

$$\Sigma_{\rm SFR} \propto \Sigma_{\rm gas}^{1.3\pm0.3}, \tag{3.7}$$

for the region active in star formation. Take notice that this power is very close to that of the global Schmidt law [eq.(3.4)] The threshold surface gas density ranges from 1 $M_\odot {\rm pc}^{-2}$ to $10 M_\odot {\rm pc}^{-2}$ ($10^{20} - 10^{21} {\rm H\,cm}^{-2}$). Therefore, theory of star formation must explain (1) the Schmidt law (clear correlation between star formation rate and the gas surface density) above the threshold column density and (2) the fact that there is no evidence for star formation in the gas deficient region below the threshold column density.

3.2 Gravitational Instability of Rotating Thin Disk

Here, we will derive the dispersion relation for the gravitational instability of a rotating thin disk. We will see the spatial variation of Toomre's Q parameter, which determines the stability of the rotating disk, explains the nonlinearity of star formation rate, that is, there is a threshold density and no stars are formed in the low density region.

Use the cylindrical coordinate (R, Z, ϕ) and the basic equations for thin disk in §2.6. In linear analysis, we assume $\Sigma(R,\phi) = \Sigma_0(R) + \delta\Sigma(R,\phi)$, $u(R,\phi) = 0 + \delta u(R,\phi)$, $v(R,\phi) = v_0(R) + \delta v(R,\phi)$, where u and v represent the radial and azimuthal component of the velocity. Linearized continuity equation is

$$\frac{\partial \delta\Sigma}{\partial t} + \frac{1}{R}\frac{\partial}{\partial R}(R\Sigma_0\delta u) + \Omega\frac{\partial \delta\Sigma}{\partial \phi} + \frac{\Sigma_0}{R}\frac{\partial \delta v}{\partial \phi} = 0, \tag{3.8}$$

where $\Omega = v_0/R$.

Linearized equations of motion are

$$\left(\frac{\partial}{\partial t} + \Omega\frac{\partial}{\partial \phi}\right)\delta u - 2\Omega\delta v = -\frac{\partial}{\partial R}(\delta\Phi + \delta h), \tag{3.9}$$

and

$$\left(\frac{\partial}{\partial t} + \Omega\frac{\partial}{\partial \phi}\right)\delta v + \frac{\kappa^2}{2\Omega}\delta u = -\frac{1}{R}\frac{\partial}{\partial \phi}(\delta\Phi + \delta h), \tag{3.10}$$

where h is a specific enthalpy as $dh = dp/\Sigma$ and

$$\kappa^2 = 4\Omega^2 + R\frac{d\Omega^2}{dR} \tag{3.11}$$

is **the epicyclic frequency**.

We assume any solution of equations (3.8), (3.9) and(3.10) can be written as a sum of terms of the form

$$\delta u = u_a \exp[i(m\phi - \omega t)], \tag{3.12}$$
$$\delta v = v_a \exp[i(m\phi - \omega t)], \tag{3.13}$$
$$\delta\Sigma = \Sigma_a \exp[i(m\phi - \omega t)], \tag{3.14}$$
$$\delta h = h_a \exp[i(m\phi - \omega t)], \tag{3.15}$$
$$\delta\Phi = \Phi_a \exp[i(m\phi - \omega t)]. \tag{3.16}$$

Using the equation of state of $p = K\Sigma^\gamma$,

$$h_a = c_s^2\Sigma_a/\Sigma_0. \tag{3.17}$$

Using equations (3.12)-(3.16), equations (3.8), (3.9), and (3.10) are rewritten as

$$i(m\Omega - \omega)\Sigma_a + \frac{1}{R}\frac{\partial}{\partial R}(R\Sigma_0 u_a) + im\frac{\Sigma_0 v_a}{R} = 0, \tag{3.18}$$

$$u_a[\kappa^2 - (m\Omega - \omega)^2] = -i\left[(m\Omega - \omega)\frac{d}{dR}(\Phi_a + h_a) + 2m\Omega\frac{(\Phi_a + h_a)}{R}\right], \tag{3.19}$$

and

$$v_a[\kappa^2 - (m\Omega - \omega)^2] = \left[\frac{\kappa^2}{2\Omega}\frac{d}{dR}(\Phi_a + h_a) + m(m\Omega - \omega)\frac{(\Phi_a + h_a)}{R}\right], \tag{3.20}$$

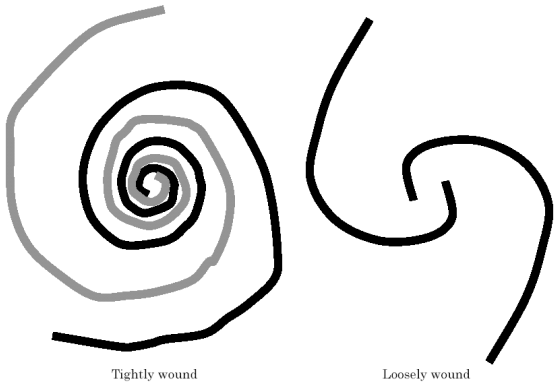

Figure 3.3: Tightly wound (left) vs loosely wound (right) spirals.

3.2.1 Tightly Wound Spirals

We assume the wave driven by the self-gravity has a form of tightly-wound spiral [Fig.3.3(left)]. When we move radially, the density $\delta\Sigma$ varies rapidly. While, it changes its amplitude slowly in the azimuthal direction. In a mathematical expression, if we write the density perturbation $\delta\Sigma$ as

$$\delta\Sigma = A(R,t)\exp[im\phi + i\,f(R,t)], \tag{3.21}$$

where the amplitude of spiral $A(R,t)$ is a slowly varing function of R, a **tightly wound spiral** means the shape function varies fast (the radial wavenumber $k \simeq df/dR$ is large enough). We consider the gravitational force from the vicinity of (R_0, ϕ_0), since the $\delta\Sigma$ oscillates and cancels even if we integrate over large region. Thus,

$$\delta\Sigma(R,\phi,t) \simeq \Sigma_a \exp[ik(R_0,t)(R-R_0)], \tag{3.22}$$

where

$$\Sigma_a = A(R_0,t)\exp[im\phi_0 + f(R_0,t)]. \tag{3.23}$$

Notice that the density perturbation [eq.(3.22)] is similar to that studied in §2.6. The potential should be expressed in a similar form to equation (2.64) as

$$\delta\Phi \simeq -\frac{2\pi G\Sigma_a}{|k|}\exp[ik(R_0,t)(R-R_0)], \tag{3.24}$$

which simply means

$$\Phi_a = -\frac{2\pi G\Sigma_a}{|k|}. \tag{3.25}$$

If we set $R = R_0$, we obtain our final result for the potential due to the surface density perturbation

$$\delta\Phi(R,\phi,t) \simeq -\frac{2\pi G}{|k|}A(R,t)\exp[im\phi + f(R,t)]. \tag{3.26}$$

Differentiating this equation with R and ignoring the term $dA(R,t)/dR$ compared to that of $df(R,t)/dR = k$, we obtain

$$\delta\Sigma(R,\phi,t) = i\frac{\mathrm{sign}(k)}{2\pi G}\frac{d\delta\Phi(R,\phi,t)}{dR}, \tag{3.27}$$

Table 3.1: Epicyclic frequency vs rotation law.

Rotation	κ
Rigid-body rotation Ω =const.	2Ω
Flat rotation v_ϕ =const.	$\sqrt{2}\Omega$
Kepler rotation $v_\phi \propto r^{-1/2}$	Ω

Neglecting the terms $\propto 1/R$ compared to the terms containing $\partial/\partial R$, equations (3.18), (3.19), and (3.20) are rewritten as

$$i(m\Omega - \omega)\Sigma_a + ik\Sigma_0 u_a = 0, \tag{3.28}$$

$$u_a[\kappa^2 - (m\Omega - \omega)^2] = (m\Omega - \omega)k(\Phi_a + h_a), \tag{3.29}$$

and

$$v_a[\kappa^2 - (m\Omega - \omega)^2] = i\frac{\kappa^2}{2\Omega}k(\Phi_a + h_a), \tag{3.30}$$

Using these equations [(3.28), (3.29), and (3.30)], $\Phi_a = -2\pi G\Sigma_a/|k|$, and $h_a = c_s^2\Sigma_a/\Sigma_0$, we obtain the dispersion relation for the self-gravitating instability of the rotating gaseous thin disk

$$(m\Omega - \omega)^2 = k^2c_s^2 - 2\pi G\Sigma_0|k| + \kappa^2. \tag{3.31}$$

Generally speaking, the epicyclic frequency depends on the rotation law but is in the range of $\Omega \lesssim \kappa \lesssim 2\Omega$ (see Table 3.1 for κ for typical rotation laws). It is shown that the system is stabilized due to the the epicyclic frequency compared with a nonrotating thin disk [eq.(3.38)].

3.2.2 Toomre's Q Value

Consider the case of $m = 0$ axisymmetric perturbations. Equation (3.31) becomes

$$\omega^2 = k^2c_s^2 - 2\pi G\Sigma_0|k| + \kappa^2 = c_s^2\left(k - \frac{\pi G\Sigma_0}{c_s^2}\right)^2 + \kappa^2 - \left(\frac{\pi G\Sigma_0}{c_s}\right)^2. \tag{3.32}$$

If $\omega^2 > 0$ the system is stable against the axisymmetric perturbation, while if $\omega^2 < 0$ the system is unstable. Defining

$$Q = \frac{\kappa c_s}{\pi G\Sigma_0}, \tag{3.33}$$

if $Q > 1$, $\omega^2 > 0$ for all wavenumbers k. On the other hand, if $Q < 1$, ω^2 becomes negative for some wavenumbers $k_1 < k < k_2$. Therefore, the Toomre's Q number gives us a criterion whether the system is unstable or not for the axisymmetric perturbation. [Recommendation for a reference book of this section: Binney & Tremaine (1988).]

The condition is expressed as

$$\Sigma_0 > \Sigma_{\rm cr} = \frac{\kappa c_s}{\pi G} \quad (Q < 1). \tag{3.34}$$

Kennicutt plotted $\Sigma_0/\Sigma_{\rm cr}$ against the normalized radius as $R/R_{\rm HII}$ for various galaxies, where $R_{\rm HII}$ represents the maximum distance of HII regions from the center (Fig.3.4). Since $\Sigma_0/\Sigma_{\rm cr} = Q$, Figure shows that HII regions are observed mainly in the region with $Q < 1$ but those are seldom seen in the outer low-density $Q > 1$ region. This seems the gravitational instability plays an important role.

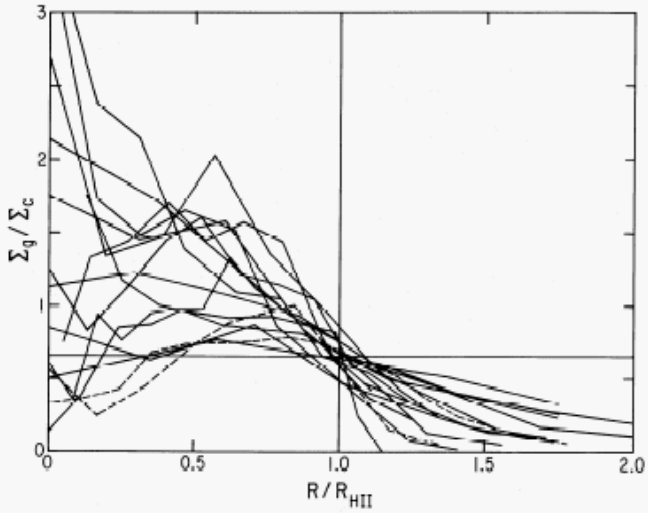

FIG. 11.—Radial dependence of the ratio of gas surface density to the critical density for gravitational stability (eq. [4]), for the galaxies with active star-forming disks. The radial coordinate is normalized to the radius of the H II region disk. The horizontal line indicates the value for the stability parameter ($\alpha = 0.67$) which best fits the observed star formation thresholds. Dashed lines denote M33 and NGC 2403.

Figure 3.4: $\Sigma_0/\Sigma_{\rm cr}$ vs $R/R_{\rm HII}$. $R_{\rm HII}$ represents the maximum distance of HII regions from the center. The sound speed is assumed constant $c_s = 6{\rm km\,s^{-1}}$. Taken from Fig.11 of Kennicutt (1989).

The above discussion is for the gaseous disk. The Toomre's Q value is also defined for stellar system as

$$Q = \frac{\sigma_R \kappa}{3.36 G \Sigma_0}, \tag{3.35}$$

where σ_R represents the radial velocity dispersion.

For non-axisymmetric waves, even if $1 \lesssim Q \lesssim 2$ the instability grows. To explain this, **the swing amplification** mechanism is proposed (Toomre 1981). If there is a leading spiral perturbation in the disk with $1 \lesssim Q \lesssim 2$, the wave unwinds and finally becomes a trailing spiral pattern. At the same time, the amplitude of the wave (perturbations) is amplified (see Fig.3.5).

3.3 Spiral Structure

Fig.3.6 shows the B- (left) and I-band images of M51. B light which originates from the massive early type stars. Although the image taken in B-band shows a number of spiral arms, that of I-band shows clearly two arms. The I-band light seems to come from mainly less-massive long-lived stars, while the $B-$band light is essentially coming from the massive short-lived stars which are formed in the spiral arm. On the contrary, the less-massive stars are not necessarily born in the spiral arm. This suggests that there are two kinds of spiral patterns: one is made by stars (mainly less-massive) and the other is the gaseous spiral arm where massive stars are born and contribute to the B-band image.

In this section, first, we will briefly describe the **density wave theory** which explains the former spiral pattern in stellar component. You will find the amplitude of the spiral pattern in stellar component is not so large. However, the response of gaseous components (HI and H_2 gas) to the spiral density wave potential with small amplitude is much more nonlinear than that of stellar component and a high-contrast spiral pattern appears in gaseous component .

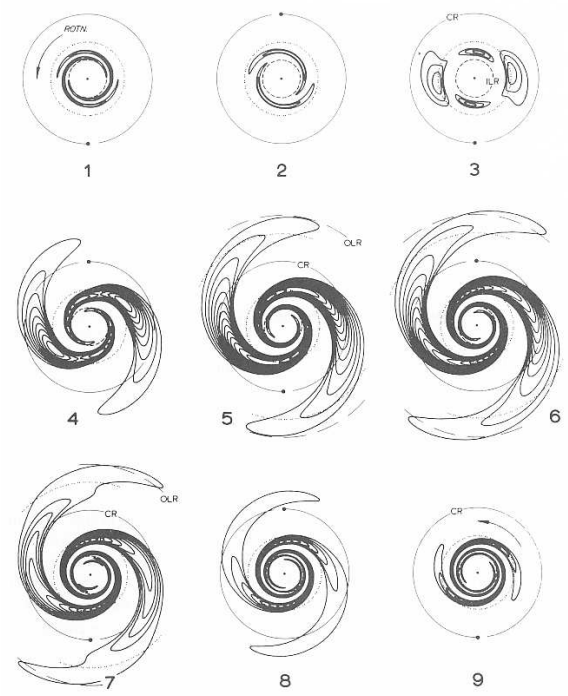

Figure 6-17. Evolution of a packet of leading waves in a stellar Mestel disk with $Q = 1.5$ and $f = 1$. Contours represent fixed fractional excess surface densities; since the calculations are based on linear perturbation theory, the amplitude normalization is arbitrary. Contours in regions of depleted surface density are not shown to minimize confusion. The time interval between diagrams is one-half of a rotation period at corotation. From Toomre (1981), by permission of Cambridge University Press.

Figure 3.5: Numerical simulation of the swing amplification mechanism. The number attached each panel shows the time sequence. This is obtained by the time-dependent linear analysis. First, perturbation with leading spiral pattern is added to the Mestel disk with $Q = 1.5$. The leading spiral gradually unwinds and become a trailing spiral. Loosely wound spiral pattern winds gradually and the last panel shows a tightly wound leading spiral pattern. The final amplitude is ~ 100 times larger than that of the initial state.

3.4 Density Wave Theory

We have derived the dispersion relation of the gravitational instability in the rotating thin disk as

$$(m\Omega - \omega)^2 = k^2 c_s^2 - 2\pi G\Sigma_0 |k| + \kappa^2, \tag{3.36}$$

where m represents the number of spiral arms. Although the stability of the stellar system is a little different, we assume this is valid for the stellar system after c_s is replaced to the velocity dispersion. Since

$$(m\Omega - \omega)^2 = k^2 c_s^2 - 2\pi G\Sigma_0 |k| + \kappa^2 = c_s^2 \left(k - \frac{\pi G\Sigma_0}{c_s^2} \right)^2 + \kappa^2 - \left(\frac{\pi G\Sigma_0}{c_s} \right)^2, \tag{3.37}$$

we obtain

$$|k| = k_{\rm T} \frac{2}{Q^2} \left[1 \pm \sqrt{1 - Q^2(1-\nu^2)} \right], \tag{3.38}$$

where $\Omega_{\rm P} = \omega/m$ is a pattern speed, $\nu = m(\Omega_{\rm P} - \Omega)/\kappa$ is the normalized frequency, $k_{\rm T} = \kappa^2/2\pi G\Sigma_0$ is the Toomre's critical wavenumber for a cold ($c_s = 0$) system. $\nu = \pm 1$, which leads to $|k| = 0$,

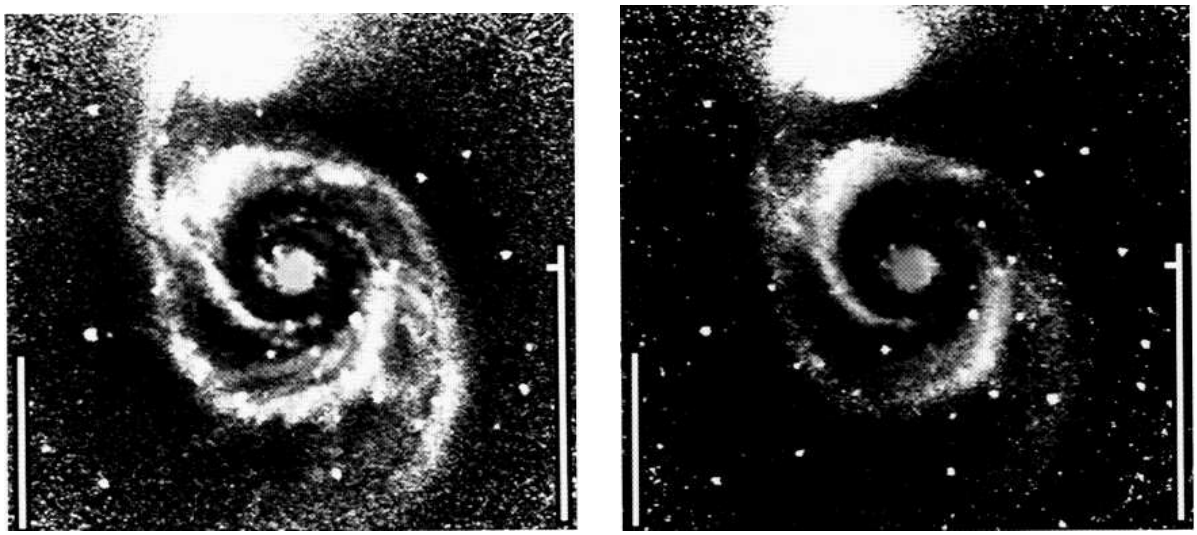

Figure 3.6: B- (left), and I-band (right) images of M51. Taken from Fig. 3 of Elmegreen et al. (1989).

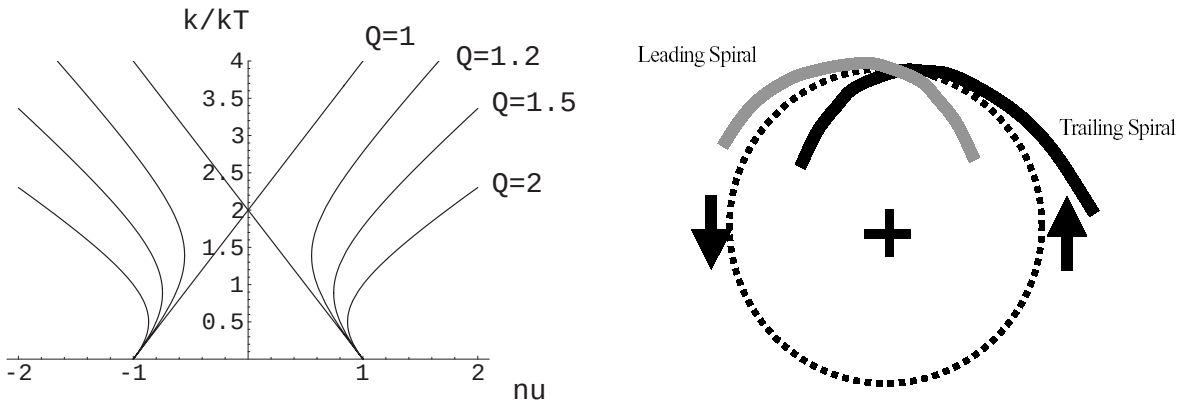

Figure 3.7: (*Left:*) A plot of the dispersion relation eq.(3.38). x- and y-axes are ν and $k/k_{\rm T}$. Respective lines are for $Q = 1$ (straight lines), $Q = 1.2$, $Q = 1.5$, and $Q = 2$. The trailing part $k > 0$ is only plotted. Points $\nu = -1$, $\nu = 0$, and $\nu = 1$ correspond respectively to Inner Lindbrad Resonance (ILR), Corotation Resonance (CR), and Outer Lindbrad Resonance (OLR). The relation is symmetric against the x-axis and the curve of $k < 0$ represents the leading wave. (*Right:*) Leading vs trailing spiral.

represents **the Lindbrad resonance** and is rewriten as

$$\Omega_{\rm P} = \frac{\omega}{m} = \Omega \pm \frac{\kappa}{2}. \tag{3.39}$$

Assuming $m = 2$, the resonance when $\Omega_{\rm P} = \Omega + \kappa/2$ is called outer Lindbrad resonance while that of $\Omega_{\rm P} = \Omega - \kappa/2$ is called inner Lindbrad resonance. $\nu = 0$ means **the co-rotation resonance** $\Omega_{\rm P} = \Omega$.

Writing down equation (3.38) [Fig.3.7(left)], it is shown that, in the case of $Q = 1$, the wavenumber exists for all ν. Since $\nu = -1$, 0, and $+1$ correspond to the points of ILR, CR, and OLR and these three resonance points appear in accordance with the radial distance, the x-axis of Figure 3.7(left) seems to correspond to the radial distance from the center. In the case of $Q > 1$, it is shown that a forbidden region appears around the co-rotation resonance point. Waves cannot propagate into the region. Figure 3.7(left) shows that the $k/k_{\rm T}$ has two possible wavenumbers in the permitted region. The waves with larger k and smaller k are called short waves and long waves.

Consider a wave expressed by $\Sigma \propto \exp[im\phi + ikr]$. If $k < 0$, moving from a point (R_0, ϕ_0) in the direction $\Delta\phi > 0$ and $\Delta r > 0$ the phase difference between the two points $[m(\phi_0 + \Delta\phi) + k(R_0 + \Delta r)] - [m\phi_0 + kR_0]$ can be equal to zero. That is, in the case of $k < 0$ the wave is leading. On the other hand, if $k > 0$, moving in the direction $\Delta\phi < 0$ and $\Delta r > 0$ the phase will be unchanged. In this case the wave pattern is trailing. Since the dispersion relation is symmetric for $k > 0$ and $k < 0$, there are two waves, trailing waves and leading waves. Therefore there are four waves: a short trailing wave, a long trailing wave, a short leading wave, and a long leading wave.

Group Velocity

The wave transfers the energy with the group velocity. Whether the group velocity is positive or negative is quite important considering the energy transfer. Using the dispersion relation, equation (3.37), The group velocity

$$v_g(R) = \frac{d\omega}{dk} = {\rm sign}(k)\frac{|k|c_s^2 - \pi G\Sigma_0}{\omega - m\Omega}. \tag{3.40}$$

For a region $R > R_{\rm CR}$, $\omega - m\Omega > 0$ or $\nu > 0$. On the other hand, for a region $R < R_{\rm CR}$, $\omega - m\Omega < 0$ or $\nu < 0$. Consider first the trailing wave. In the region $R > R_{\rm CR}$, long-waves propagate inwardly to the CR, since $|k|c_s^2 < \pi G\Sigma_0$ for long-waves and $\nu > 0$. Short-waves propagate outwardly from the CR, since $|k|c_s^2 > \pi G\Sigma_0$ for short-waves and $\nu > 0$. In the region $R < R_{\rm CR}$, long-waves propagate outwardly to the CR since $|k|c_s^2 < \pi G\Sigma_0$ and $\nu < 0$. Short-waves propagate inwardly from the CR, since $|k|c_s^2 > \pi G\Sigma_0$ and $\nu < 0$. As a result, it is concluded that the long-wave propagates toward the CR and the short-wave does away from the CR. As for the leading wave, the short-wave propagates toward the CR and the long-wave does away from the CR.

Assuming that the wave packet is made near the Lindblad resonance points, (1) the long-trailing waves propagate toward the co-rotation resonance points; (2) they are reflected by the Q-barrier; (3) they change their character to short-waves and propagate away from the co-rotation resonance points; and finally (4) the waves are absorbed at the center or propagate away to the infinity. (1) the short-leading waves propagate toward the co-rotation resonance points; (2) they are reflected by the Q-barrier; (3) they change their character to long-waves and propagate away from the co-rotation resonance points; and finally (4) they reach the Lindblad resonance points and the energy may be converted to the long-trailing waves there.

The wave obtains its energy at the resonance points. The density wave transfer the energy to the co-rotation points. Therefore, the density wave theory predicts the galactic stellar disk has spiral density pattern between the inner Lindblad resonance points and the outer Lindblad resonance point if $Q \gtrsim 1$.

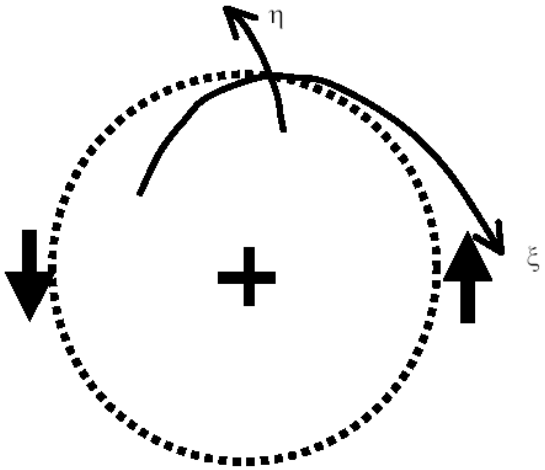

Figure 3.8: Spiral coordinate. Along a curve of constant η, $r \propto \exp(\theta \tan i)$.

3.5 Galactic Shock

In the preceding section, we have seen that a spiral pattern of density perturbation is made by the gravitational instability in the stellar system with $Q \gtrsim 1$. This forms a grand design spiral observed in the I-band images which represent the mass distribution which consists essentially in less-massive stars. The amplitude of the pattern is smaller than that observed in B-band images. In this section we will see how the distribution early type stars is explained. [Recommendation for a reference book of this section: Spitzer (1978).]

Gas flowing through a spiral gravitational potential, even if its amplitude is relatively small, acts rather nonlinearly. Consider the gravitational potential in the sum of an axisymmetric term, $\Phi_0(R)$ and a spiral term $\Phi_1(R)$. The spiral gravitational field is rotating with a pattern speed $\Omega_{\rm P}$. We use a reference frame rotating with $\Omega_{\rm P}$. $\mathbf{u} = (u, v)$, where u and v are radial (R) and azimuthal (ϕ) component of the flow velocity. Consider the reference system rotating with the angular rotation speed $\Omega_{\rm P}$. We assume the variables with suffix 0 represent those without the spiral potential Φ_1 and variables with suffix 1 are used to express the difference between before and after Φ_1 is added. $u = u_0 + u_1 = 0 + u_1$, $v = v_0 + v_1$, and

$$v_0 = R(\Omega - \Omega_{\rm P}) = R\left[\left(\frac{1}{R}\frac{\partial \Phi_0}{\partial R}\right)^{1/2} - \Omega_{\rm P}\right], \tag{3.41}$$

where Ω means the circular rotation speed. The equation of motion in the r-direction is

$$\frac{\partial u}{\partial t} + u\frac{\partial u}{\partial r} + \frac{v}{r}\frac{\partial u}{\partial \theta} - \frac{v_1^2}{r} = -\frac{c_s^2}{\Sigma}\frac{\partial \Sigma}{\partial r} - \frac{\partial \Phi_1}{\partial r} + 2\Omega v_1, \tag{3.42}$$

and that in the ϕ direction is

$$\frac{\partial v}{\partial t} + u\left(\frac{\partial v_1}{\partial r} + \frac{v_1}{r}\right) + \frac{v}{r}\frac{\partial v_1}{\partial \phi} = -\frac{c_s^2}{\Sigma r}\frac{\partial \Sigma}{\partial \phi} - \frac{1}{r}\frac{\partial \Phi_1}{\partial \phi} - \frac{\kappa^2}{2\Omega}u, \tag{3.43}$$

and the continuity equation is

$$\frac{\partial \Sigma R u}{\partial R} + \frac{\partial \Sigma v}{\partial \phi} = 0. \tag{3.44}$$

As seen in Figure 3.8, we introduce the spiral coordinate (η, ξ) in which ξ-axis is parallel to the spiral pattern which has a pitch angle i and η-axis is perpendicular to the ξ-axis.

$$
\begin{aligned}
r d\eta &= dr\cos i + r d\phi \sin i, && (3.45)\\
r d\xi &= -dr\sin i + r d\phi \cos i. && (3.46)\\
v_\eta &= u\cos i + v\sin i, && (3.47)\\
v_\xi &= -u\sin i + v\cos i && (3.48)
\end{aligned}
$$

Assuming that $i \ll 1$ (tightly wound spiral), equations (3.44) (3.42) and (3.43) become

$$\frac{\partial v_\eta}{\partial t} + v_\eta \frac{\partial v_\eta}{\partial \eta} = -\frac{c_s^2}{\Sigma}\frac{\partial \Sigma}{\partial \eta} - \frac{\partial \Phi_1}{\partial \eta} + 2\Omega(v_\xi - v_{\xi 0}), \tag{3.49}$$

$$\frac{\partial v_\xi}{\partial t} + v_\eta \frac{\partial v_\xi}{\partial \eta} = -\frac{\kappa^2}{2\Omega}(v_\eta - v_{\eta 0}), \tag{3.50}$$

$$\frac{\partial \Sigma}{\partial t} + \frac{\partial \Sigma v_\eta}{\partial \eta} = 0. \tag{3.51}$$

Similar to §2.7 we look for a steady state solution. Equation (3.51) becomes

$$\frac{d\Sigma}{d\eta} = -\frac{\Sigma}{v_\eta}\frac{dv_\eta}{d\eta}. \tag{3.52}$$

Using this, equation (3.49) reduces to

$$\left(v_\eta^2 - c_s^2\right)\frac{dv_\eta}{d\eta} = 2\Omega(v_\xi - v_{\xi 0}) - \frac{d\Phi_1}{d\eta}. \tag{3.53}$$

Equation (3.50) becomes

$$v_\eta \frac{dv_\xi}{d\eta} = -\frac{\kappa^2}{2\Omega}(v_\eta - v_{\eta 0}), \tag{3.54}$$

In these equations we used following quantities:

$$
\begin{aligned}
v_\eta &= v_{\eta 0} + v_{\eta 1}, && (3.55)\\
v_\xi &= v_{\xi 0} + v_{\xi 1}, && (3.56)\\
v_{\eta 0} &= v_0 \sin i, && (3.57)\\
v_{\xi 0} &= v_0 \cos i, && (3.58)
\end{aligned}
$$

v_0 is given in equation (3.41).

Equations (3.52), (3.53), and (3.54) are solved under the periodic boundary condition: $X(\eta =$ right end$) = X(\eta =$ left end$)$. Since equation (3.53) is similar to the equations in §2.7, you may think the solution seems like Figure 2.5. However, it contains a term which expresses the effect of Coliois force $2\Omega(v_\xi - v_{\xi 0})$, the flow becomes much complicated.

Taking care of the point that a shock front exists for a range of parameters, the solution of the above equations are shown in Figure 3.9. Numerical hydrodynamical calculations which solve equations (3.49), (3.50), and (3.51) was done and steady state solutions are obtained (Woodward 1975). It is shown that $F \leq 0.7\%$, the velocity (v_η: velocity perpendicular to the wave) does not show any discontinuity. In contrast, for $F > 2\%$, a shock wave appears. Steady state solution is obtained from the ordinary differential equations (3.52) (3.53), and (3.54) by Shu, Milione, &

Roberts (1973). Inside the CR, $v_0 > 0$ (Gas has a faster rotation speed than the spiral pattern). As long as $v_\eta > c_s$ there is no shock. Increasing the amplitude of the spiral force F, an amplitude of the variation in v_η increases and finally v_η becomes subsonic partially. When the flow changes its nature from supersonic to subsonic, it is accompanied with a shock. (An inverse process, that is, changing from subsonic to supersonic is not accompanied with a shock.)

In the outer galaxy (still inside CR) since $\Omega - \Omega_{\rm P}$ decreases with the the distance from the galactic center, $v_{\eta 0} = R(\Omega - \Omega_{\rm P}) \sin i$ decreases. In this region, $v_{\eta 0} < c_{is}$ and the flow is subsonic if there is no spiral gravitational force, $F = 0$. In such a circumstance, increasing F amplifies the variation in v_η and v_η finally reaches the sound speed. Transonic flow shows again a shock.

Summary of this section is:

1. There exists a spiral density pattern of the stellar component if the Toomre's Q parameter is $1 \lesssim Q \lesssim 2$.
2. This is driven by the self-gravity of the rotating thin disk.
3. If the amplitude of the non-axisymmetric force is as large as $\sim 1\%$ of the axisymmetric one, interstellar gas whose sound speed is as large as $c_{is} \sim 8 {\rm km\,s^{-1}}$ forms the galactic shock. This is observed when the flow is transonic.
4. The amplitude of the **gas** density fluctuation is much larger than that in the stellar density.
5. If stars are formed preferentially in the postshock region of the spiral arm, we expect clear spiral arms made by early-type stars, which are massive and short-lived, as seen in the B band images of spiral galaxies.

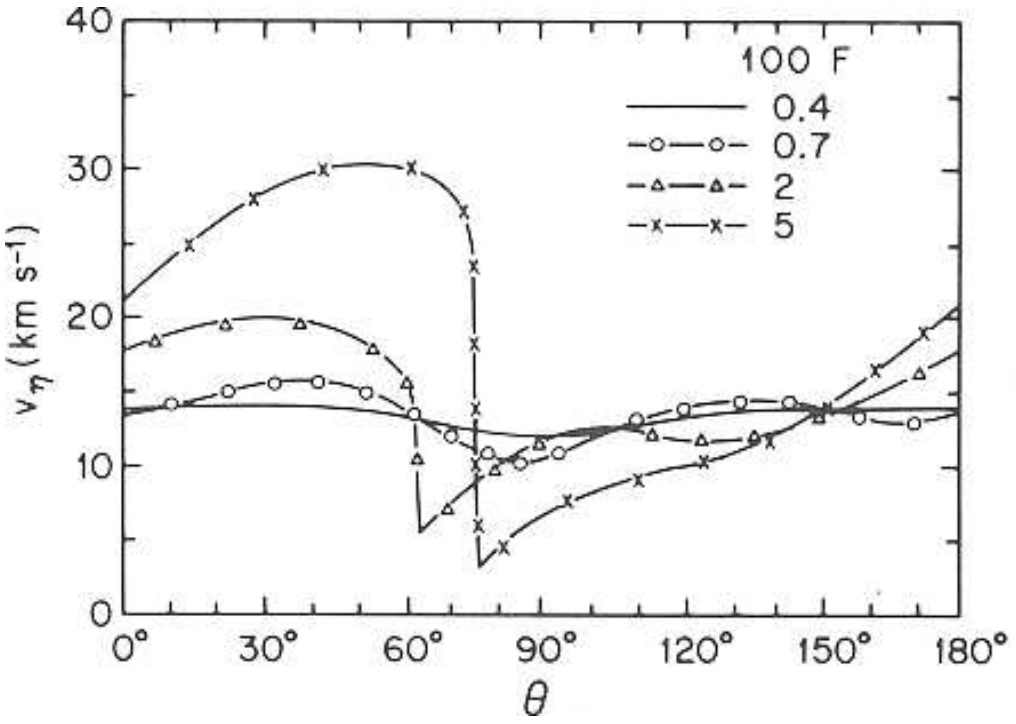

Figure 3.9: Galactic shocks. The velocity perpendicular to the spiral wave front is plotted against the phase of the spiral wave. The spiral potential takes its minimum at $\theta = 90$. $c_s = 8.6\mathrm{km\,s^{-1}}$, $i = 6.7$ deg, $R = 10\mathrm{kpc}$, $R\Omega = 250\mathrm{km\,s^{-1}}$, $R\kappa = 313\mathrm{km\,s^{-1}}$, $R\Omega_\mathrm{P} = 135\mathrm{km\,s^{-1}}$ The amplitude of spiral gravity force is taken F =0.4%, 0.7%, 2%, and 5% of the axisymmetric force $\partial\Phi_0/\partial R$. Taken from Fig.13.3 of Spizer (1978) [originally Woodward (1975)].

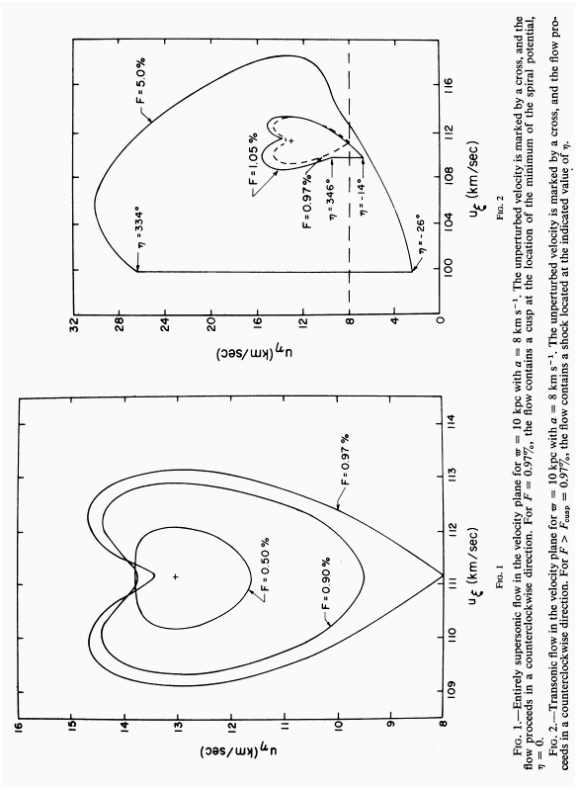

FIG. 1.—Entirely supersonic flow in the velocity plane for $\varpi = 10$ kpc with $a = 8$ km s^{-1}. The unperturbed velocity is marked by a cross, and the flow proceeds in a counterclockwise direction. For $F = 0.97\%$, the flow contains a cusp at the location of the minimum of the spiral potential, $\eta = 0$.

FIG. 2.—Transonic flow in the velocity plane for $\varpi = 10$ kpc with $a = 8$ km s^{-1}. The unperturbed velocity is marked by a cross, and the flow proceeds in a counterclockwise direction. For $F > F_{cusp} = 0.97\%$, the flow contains a shock located at the indicated value of η.

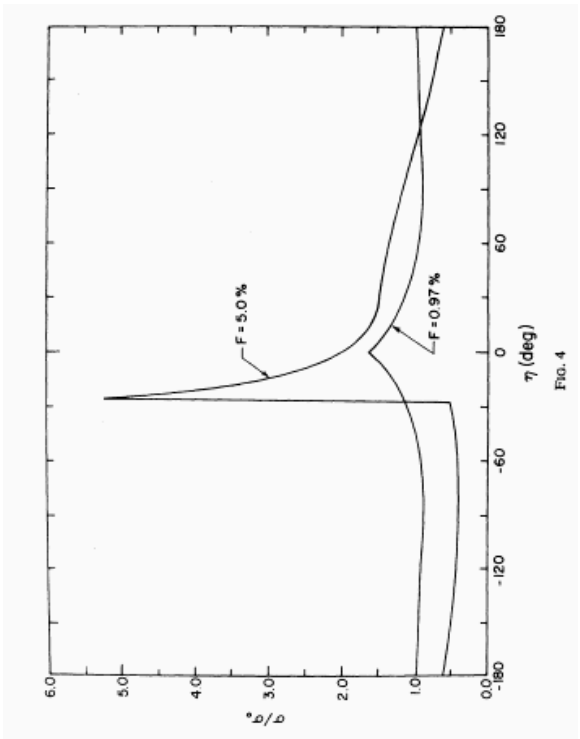

FIG. 4

Figure 3.10: Galactic shock. (*Left:*) v_η vs v_ξ plot. Increasing F from 0.5% to 0.9%, the variation in v_η increases. And at $F = 0.97\%$, the minimum speed reaches the sound speed $8\mathrm{km\,s^{-1}}$. Further increasing F, a subsonic region appears ($v_\eta < c_{is}$ for $F = 1.05\%$ and 5%) . When flow changes its nature from supersonic to subsonic, a shock appears. $R = 10\mathrm{kpc}$, $c_s = 8\mathrm{km\,s^{-1}}$, $i = 6.7$ deg. Other parameters are the same as Fig.3.9. (*Right:*) Comparison of two density distributions: $F = 0.97$and $F = 5\%$ (shock). Taken from Shu, Milione, & Roberts (1973).

Chapter 4

Local Star Formation Process

4.1 Hydrostatic Balance

Consider a hydrostatic balance of isothermal cloud. By the gas density, ρ, the isothermal sound speed, $c_{\rm is}$, and the gravitational potential, Φ, the force balance is written as

$$-\frac{c_{\rm is}^2}{\rho}\frac{d\rho}{dr} - \frac{d\Phi}{dr} = 0, \tag{4.1}$$

and the gravity is calculated from a density distribution as

$$-\frac{d\Phi}{dr} = -\frac{GM_r}{r^2} = -\frac{4\pi G}{r^2}\int_0^r \rho r^2 dr, \tag{4.2}$$

for a spherical symmetric cloud, and the expression for a cylindrical cloud is

$$-\frac{d\Phi}{dr} = -\frac{G\lambda_r}{r} = -\frac{2\pi G}{r}\int_0^r \rho r dr, \tag{4.3}$$

where λ represents the mass per unit length within a cylinder of radius being r.

For the spherical symmetric case, the equation becomes the Lane-Emden equation with the polytropic index of ∞. This has no analytic solutions. However, the numerical integration gives us a solution shown in Figure 4.1 (left). Only in a limiting case with the infinite central density, the solution is expressed as

$$\rho(r) = \frac{c_{\rm is}^2}{2\pi G} r^{-2}. \tag{4.4}$$

Increasing the central density, the solution reaches the above Singular Isothermal Sphere (SIS) solution.

On the other hand, a cylindrical cloud has an analytic solution (Ostriker 1964) as

$$\rho(r) = \rho_c \left(1 + \frac{r^2}{8H^2}\right)^{-2}, \tag{4.5}$$

where

$$H^2 = c_{\rm is}^2/4\pi G\rho_c. \tag{4.6}$$

Far from the cloud symmetric axis, the distribution of equation (4.5) gives

$$\rho(r) \propto r^{-4}, \tag{4.7}$$

while the spherical symmetric cloud has

$$\rho(r) \propto r^{-2} \tag{4.8}$$

distribution.

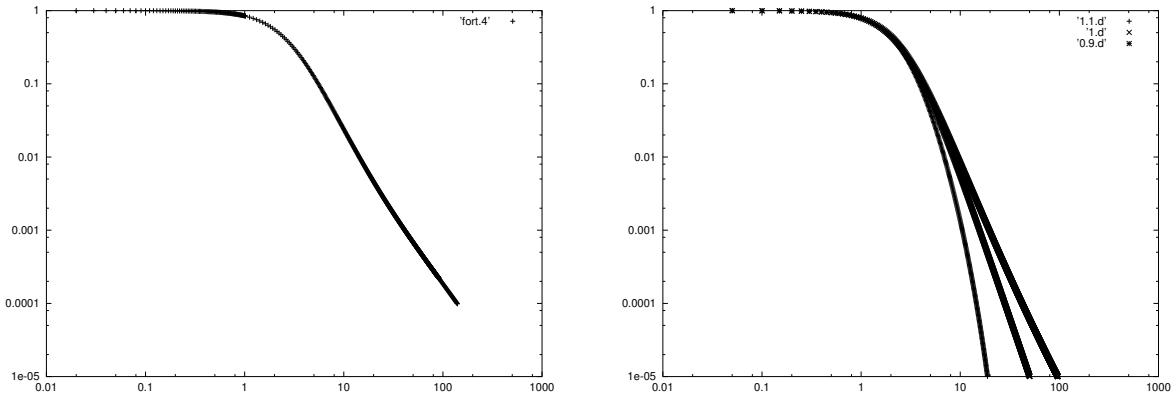

Figure 4.1: Radial density distribution. A spherical cloud (left) and a cylindrical cloud (right). In the right panel, solutions for polytropic gases with $\Gamma = 1.1$ (relatively compact) and $\Gamma = 0.9$ (relatively extended) are plotted as well as the isothermal one.

4.1.1 Bonnor-Ebert Mass

In the preceding section [Fig.4.1 (left)], we have seen the radial density distribution of a hydrostatic configuration of an isothermal gas. Consider a circumstance that such kind of cloud is immersed in a low-density medium with a pressure p_0. To establish a pressure equilibrium, the pressure at the surface $c_{\rm is}^2\rho(R)$ must equal to p_0. This means that the density at the surface is constant $\rho(R) = p_0/c_{\rm is}^2$.

Figure 4.2 (left) shows three models of density distribution, $\rho_c = \rho(r = 0) = 10\rho_s$, $10^2\rho_s$, and $10^3\rho_s$. It should be noticed that the cloud size (radius) is a decreasing function of the central density ρ_c. The mass of the cloud is obtained by integrating the distribution, which is illustrated against the central-to-surface density ratio ρ_c/ρ_s in Figure 4.2 (right). The y-axis represents a normalized mass as $m = M/[4\pi\rho_s(c_{\rm is}/\sqrt{4\pi G\rho_s})^3]$. The maximum value of $m = 4.026$ means

$$M_{\rm max} \simeq 1.14\frac{c_{\rm is}^2}{G^{3/2}p_0^{1/2}}. \tag{4.9}$$

This is the maximum mass which is supported against the self-gravity by the thermal pressure with an isothermal sound speed of $c_{\rm is}$, when the cloud is immersed in the pressure p_0. This is called Bonnor-Ebert mass [Bonnor (1956), Ebert (1955)]. It is to be noticed that the critical state $M = M_{\rm max}$ is achieved when the density contrast is rather low $\rho_c \simeq 16\rho_s$.

(to be finished) Another important result from Figure4.2 (right) is the stability of an isothermal cloud. Any clouds on the part of $\partial m/\partial\rho_c < 0$ are unstable. This is because (1) if the ambient pressure increases suddenly, a cloud on the part of $\partial m/\partial\rho_c > 0$ will raise the central density

4.1.2 Equilibria of Cylindrical Cloud

In Figure 4.1 (right) we plotted the structure for a polytropic cloud. Inner structure is not dependent of Γ, it is clear the slope of the outer envelope is related to Γ.

1. In the case of the spherically symmetric, consider a polytrope ($p \propto \rho^\Gamma$) with $\Gamma < 6/5$ (at least the envelope of $\Gamma = 6/5$ cloud extends to ∞.), in which gas extends to ∞. if $\rho \propto r^{-p}$, the mass inside of r is proportional to $M_r \propto r^{3-p}$. Thus, the gravity per unit volume at a radius r, $GM\rho/r^2$, is proportional to $GM\rho/r^2 \propto r^{1-2p}$. On the other hand the pressure force is

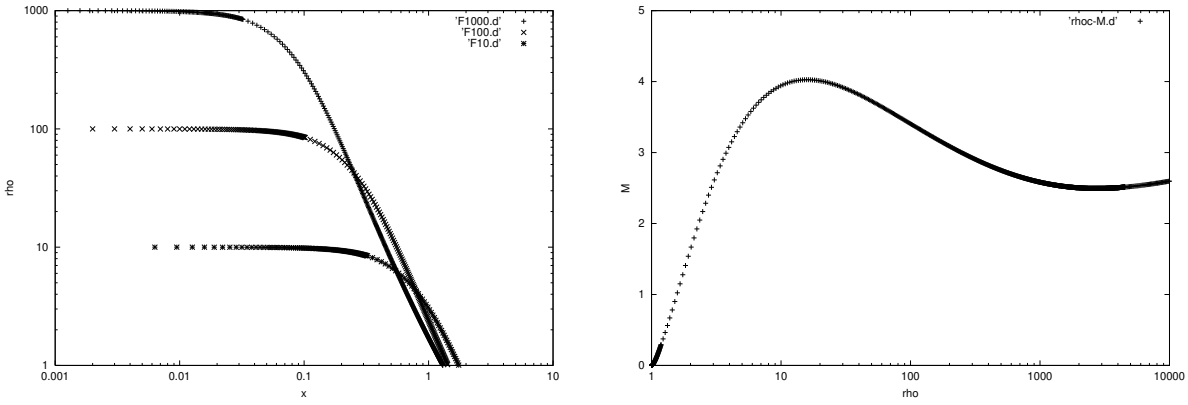

Figure 4.2: (Left:) radial density distribution. Each curve has different ρ_c. It is shown that the radius increases with decreasing ρ_c. A spherical cloud (left) and a cylindrical cloud (right).

$|(\partial p/\partial r)| = (\partial p/\partial \rho)|(\partial \rho/\partial r)| \propto (r^{-p})^{\Gamma-1} r^{-p-1} \propto r^{-p\Gamma-1}$. The two powers become the same, only if $p = 2/(2-\Gamma)$.

2. In the case of cylindrical cloud, with $\Gamma \leq 1$ the mass per unit length $\lambda \propto r^{2-p}$. The gravity at r, $G\lambda\rho/r \propto r^{1-2p}$. Note that the power is the same as the spherical case. Since the power of the pressure force should be the same as the spherical case, the resultant p should be the same $p = 2/(2-\Gamma)$.

The case of $\Gamma = 0.9$, an envelope extending to a large radius indicates the power-law distribution much shallower than that of the isothermal $\Gamma = 1$ one.

4.2 Virial Analysis

Hydrodynamic equation of motion using the Eulerian derivative is

$$\rho\left(\frac{d\mathbf{u}}{dt}\right) = -\nabla p - \rho\nabla\Phi. \tag{4.10}$$

Multiplying the position vector $\mathbf{r}$ and integrate over a volume of a cloud, we obtain the Virial relation as

$$\frac{1}{2}\frac{d^2 I}{dt^2} = 2(T - T_0) + W, \tag{4.11}$$

where

$$I = \int \rho r^2 dV, \tag{4.12}$$

is an inertia of the cloud,

$$T = \int \left(\frac{3}{2}p_{\rm th} + \frac{1}{2}\rho v^2\right) dV = \frac{3}{2}\bar{P}V_{\rm cl}, \tag{4.13}$$

is a term corresponding to the thermal pressure plus turbulent pressure,

$$T_0 = \int_S P_{\rm th}\mathbf{r}\cdot\mathbf{n}dS = \frac{3}{2}P_0 V_{\rm cl} \tag{4.14}$$

comes from a surface pressure, and

$$W = -\int \rho \mathbf{r} \cdot \nabla \Phi dV = -\frac{3}{5}\frac{GM^2}{R} \tag{4.15}$$

is a gravitational energy. To derive the last expression in each equation, we have assumed the cloud is spherical and uniform. Here we use a standard notation as the radius R, the volume $V_{\rm cl} = 4\pi R^3/3$, the average pressure $\bar{P}$, and the mass M.

To obtain a condition of mechanical equilibrium, we assume $d^2I/dt^2 = 0$. Equation (4.11) becomes

$$4\pi\bar{p}R^3 - 4\pi p_0 R^3 - \frac{3}{5}\frac{GM^2}{R} = 0. \tag{4.16}$$

Assuming the gas is isothermal $p = c_{\rm is}^2\rho$, the average pressure is written as

$$\bar{p} = c_{\rm is}^2\bar{\rho} = c_{\rm is}^2\frac{3M}{4\pi R^3}. \tag{4.17}$$

Using equation (4.17) to eliminate $\bar{p}$ from equation (4.11), the external pressure is related to the mass and the radius as

$$p_0 = \frac{3c_{\rm is}^2 M}{4\pi R^3} - \frac{3GM^2}{20\pi R^4}. \tag{4.18}$$

Keeping M constant and increasing R from zero, p_0 increases first, but it takes a maximum, $p_{0,\rm max} = 3.15c_{\rm is}^8/(G^3M^2)$, and finally declines. This indicates that the surface pressure must be smaller than $p_{0,\rm max}$ for the cloud to be in an equilibrium. In other words, keeping p_0 and changing R, it is shown that M has a maximum value. The maximum mass is equal to

$$M_{\rm max} = 1.77\frac{c_{\rm is}^4}{G^{3/2}p_0^{1/2}}, \tag{4.19}$$

which corresponding to the Bonnor-Ebert mass, although the numerical factors are slightly different.

4.2.1 Magnatohydrostatic Clouds

Consider here the effect of the magnetic field. In the magnetized medium, the Lorentz force

$$\mathbf{F} = \frac{1}{4\pi}(\nabla \times \mathbf{B}) \times \mathbf{B} = -\frac{1}{8\pi}\nabla \mathbf{B^2} + \frac{1}{4\pi}(\mathbf{B} \cdot \nabla)\mathbf{B} \tag{4.20}$$

works in the ionized medium. The first term of equation (4.20), which is called the **magnetic pressure**, has an effect to support the cloud against the self-gravity.

The virial analysis is also applicable to the magnetohydrostatic clouds. The terms related to the magnetic fields are

$$\begin{aligned} M &= \int \frac{B^2}{8\pi}dV + \int_S (\mathbf{r}\cdot\mathbf{B})\mathbf{B}\cdot\mathbf{n}dS - \int_S \frac{B^2}{8\pi}\mathbf{r}\cdot\mathbf{n}dS \\ &\simeq \int \frac{B^2 - B_0^2}{8\pi}dV \simeq \frac{1}{6\pi^2}\left(\frac{\Phi_B^2}{R} - \frac{\Phi_B^2}{R_0}\right), \end{aligned} \tag{4.21}$$

where Φ_B represents a magnetic flux and it is assumed to be conserved if we change the radius, R, that is $\Phi_B = \pi B_0 R_0^2 = \pi B R^2$. Equation (4.16) becomes

$$4\pi\bar{p}R^3 - 4\pi p_0 R^3 - \frac{3}{5}\frac{GM^2}{R} + \frac{1}{6\pi^2}\frac{\Phi_B^2}{R} = 0, \tag{4.22}$$

where we ignored the term $\frac{1}{6\pi^2}\frac{\Phi_B^2}{R_0}$. The last two terms are rewritten as

$$\frac{3}{5}\frac{G}{R}\left(M^2 - M_\Phi^2\right), \tag{4.23}$$

where M_Φ is defined as $3GM_\Phi^2/5 = \Phi_B^2/6\pi^2$.

This shows the effects of the magnetic fields:

1. B-fields effectively reduce the gravitational mass as $M^2 - M_\Phi^2 = M^2 - 5\Phi_B^2/(18\pi^2 G)$. This plays a part to support a cloud.

2. However, even a cloud contracts (decreasing its radius from R_0 to R), the ratio of the gravitational to the magnetic terms keeps constant since these two terms are proportional to $\propto R^{-1}$. Thus, if the magnetic term does not work initially, the gravitational term continues to predominate over the magnetic term.

If $M < M_\Phi$, a sum of last two terms in equation (4.22) is positive. Since the second term of rhs of equation (4.18) is positive, there is one R which satisfies equation (4.22) irrespective of the external pressure p_0. While, if $M > M_\Phi$, there is a maximum allowable p_0. Therefore, $M = M_\Phi$ gives a criterion whether the magnetic fields work to support the cloud or not. More realistic calculation [Mouschovias (1976), Tomisaka et al (1988)] gives us a criterion

$$G^{1/2}\frac{dm}{d\Phi_B} = \frac{G^{1/2}\sigma}{B} = 0.17 \simeq \frac{1}{2\pi}, \tag{4.24}$$

where σ and B means the column density and the magnetic flux density. A cloud with a mass

$$M > \frac{\Phi_B}{2\pi G^{1/2}} \tag{4.25}$$

is sometimes called magnetically supercritical, while that with

$$M < \frac{\Phi_B}{2\pi G^{1/2}} \tag{4.26}$$

is subcritical.

More precisely speaking, the criterion showed in equations (4.25) and (4.26) should be applied for a cloud which has a much larger mass than the Bonnor-Ebert mass. That is, even without magnetic fields, the cloud less-massive than the Bonnor-Ebert mass has a hydrostatic configuration shown in Figure 4.2 (left). The cloud with central density of $\rho_c = 10$ has a stable density distribution. To fit the numerical results, Tomisaka et al (1988) obtained an expression for the critical mass when the cloud has a mass-to-flux ratio $dm/d\Phi_B$, the isothermal sound speed c_{is}, and the external pressure p_0 as

$$M_{cr} = 1.3\left\{1 - \left[\frac{1/2\pi}{G^{1/2}dm/d\Phi_B|_{r=0}}\right]^2\right\}^{-3/2}\frac{c_s^4}{p_0^{1/2}G^{3/2}}. \tag{4.27}$$

This shows that the critical mass is a decreasing function of the mass-to-flux ratio or increasing function of the magnetic flux. And the critical mass becomes much larger than the Bonnor-Ebert mass $\simeq c_s^4/(p_0^{1/2}G^{3/2})$ only when the mass-to-flux ratio at the center of the cloud is reaching $1/2\pi$ at which the term in the curry bracket goes to zero. Hereafter, we call here the cloud/cloud core with mass larger than the critical mass $M_{\rm cr}$ a supercritical cloud/cloud core. The cloud/cloud core less-massive than the critical mass is subcritical.

4.3 Evolution of Cloud/Cloud Cores

We have seen there is a critical mass above which the cloud has no (magneto)hydrostatic configuration but below which the cloud has at least an equilibrium state. This gives us an idea that there are two kind of clouds/cloud cores: that with a mass larger than the critical mass which has to collapse dynamically and that with a mass smaller than the critical mass which is in an equilibrium state. In the density range of $10^4\mathrm{cm}^{-3} \lesssim n \lesssim 10^{10}\mathrm{cm}^{-3}$, the interstellar gas is essentially isothermal. In this region a major cooling agent is dusts; that is, the dust is heated by the collision of molecules. the excess energy liberated at the collision increases the dust temperature. Finally the thermal emission from the dust cools down the dust again. By this process, the thermal energy of the gas is reduced. Therefore, we consider the cloud/cloud core is isothermal and study the collapse of the isothermal cloud.

4.3.1 Subcritical Cloud vs Supercritical Cloud

Since the supercritical cloud has no hydrostatic configuration, it must evolve in a dynamical way. On the other hand, since the subcritical cloud is in a static state, it evolves in much longer time-scale of the free-fall time. Such cloud evolves by the effect of the ambipolar diffusion.

Ambipolar Diffusion

In the molecular cloud $10^4\mathrm{cm}^{-3} \lesssim n \lesssim 10^{10}\mathrm{cm}^{-3}$, the ionization fraction is low. In such an interstellar medium, the neutral molecules, a major component of the gas, are coupled with the magnetic field indirectly via ionized ions. The ionized ions are affected by the Lorentz force. At the same time, if the neutral molecules drift across the magnetic field lines and the ions, the ions collide with neutral molecules and obtain momentum from the neutral molecule. This force acts as the drag force. The force balance for the ions is written down as

$$F_{\mathrm{Lorentzforce}} = F_{\mathrm{drag}}, \tag{4.28}$$

and that for the molecules is

$$F_{\mathrm{gravity}} = F_{\mathrm{drag}} + F_{\mathrm{pressure}}, \tag{4.29}$$

where we ignored the gravity and the pressure force for the ions which are much weaker than the Lorentz force. Eliminating the mutual drag force, these reduce to an ordinary force balance as the gravity is counter-balanced by the sum of the Lorentz force and the thermal pressure force. In this sense, even the cloud with low ionization fraction is supported by the Lorentz force, if the cloud is subcritical. However, for the drag force to play a role, the neutral have to drift against the ionized component and thus the magnetic field lines. This means that the neutral molecules are convected to the central part of the cloud. This increases the mass-to-flux ratio at the center $dm/d\Phi_B|_{r=0}$. Equation 4.27 indicates that the critical mass decreases with increasing the mass-to-flux at the center. If the critical mass becomes smaller than the cloud mass, the cloud becomes **supercritical** and the cloud has no hydrostatic configuration. The cloud begins dynamical collapse. F.Shu considers this is a major evolutional path to initiate star formation in a subcritical cloud/cloud core. Since the hydrostatic state with high density contrast between the center and the surface has a characteristic power-law density distribution as $\propto r^{-2}$, the final state of the subcritical cloud driven by the ambipolar diffusion is considered to have a density distribution similar to the singular isothermal sphere (SIS).

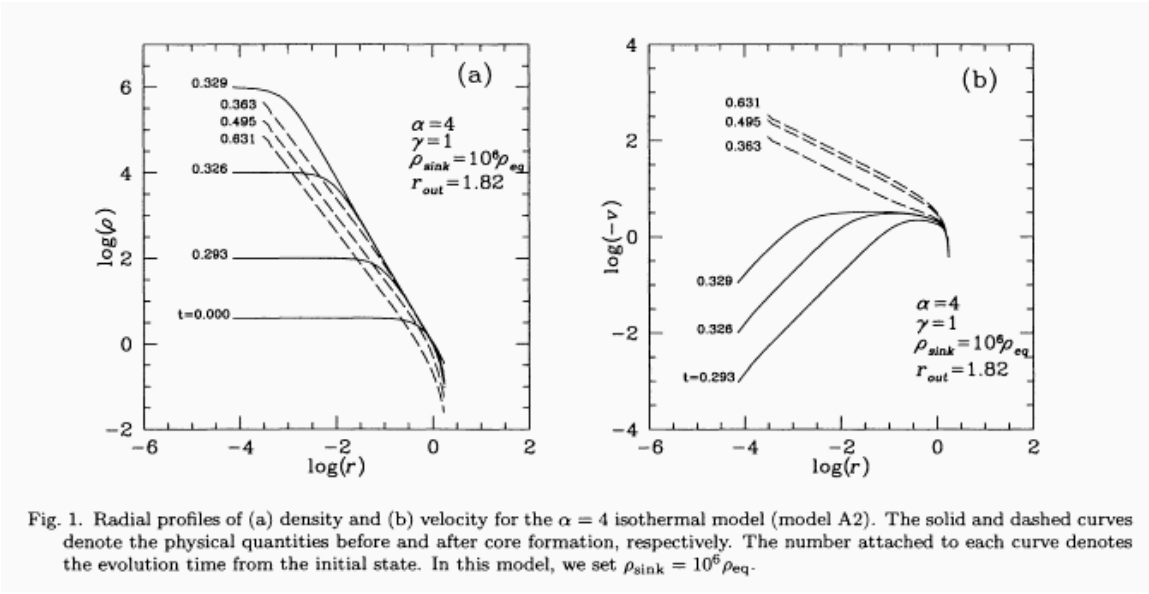

Fig. 1. Radial profiles of (a) density and (b) velocity for the $\alpha = 4$ isothermal model (model A2). The solid and dashed curves denote the physical quantities before and after core formation, respectively. The number attached to each curve denotes the evolution time from the initial state. In this model, we set $\rho_{\rm sink} = 10^6 \rho_{\rm eq}$.

Figure 4.3: Evolution of isothermal clouds massive than the Bonnor-Ebert mass. Density (*left*) and velocity (*right*) distributions are illustrated. Solid lines show the cores of the preprotostellar phase (prestellar core) and dashed lines show those of protostellar phase (protostellar core). The evolution of the protostellar phase is studied by the sink-cell method, where we assume the gas that entered in the sink-cells is removed from finite-difference grids and add to the point mass sitting at the center of the sink-cells which corresponds to a protostar.

Dynamical Collapse

In 1969, Larson (1969) and Penston (1969) found a self-similar solution which is suited for the dynamical contraction. Figure 4.3 is a radial density distribution for a spherical collapse of an isothermal cloud, where the cloud has a four-times larger mass than that of the Bonnor-Ebert mass. Although the figure is taken from a recent numerical study by Ogino et al (1999), a similar solution was obtained in Larson (1969). We can see that the solution has several characteristic points as

1. The cloud evolves in a self-similar way. That is, the spatial distribution of the density (left) at $t = 0.326$ is well fitted by that at $t = 0.293$ after shifting in the $-x$ and the $+y$ directions. As for the infall velocity spatial distribution, only a shift in the $-x$ direction is needed.

2. The density distribution in the envelope, which is fitted by $\propto r^{-2}$, is almost unchanged. Only the central part of the cloud (high-density region) contracts.

3. The time before the core formation epoch (the core formation time t_0 is defined as the time at which the central density increases greatly) is a good indicator to know how high the central density is. That is, reading from the figure, at $t - t_0 = 0.003$ ($t = 0.326$) the central density reaches $\rho_c \simeq 10^4$ and at $t - t_0 = 0.036$ ($t = 0.293$) the density is equal to $\rho_c \simeq 10^2$. This shows the maximum (central) density is approximately proportional to $(t - t_0)^2$, which is reasonable from the description of the free-fall time $\propto \rho^{-1/2}$.

The basic equations of spherical symmetric isothermal flow are

$$\frac{\partial \rho}{\partial t} + \frac{1}{r^2}\frac{\partial}{\partial r}(r^2 \rho v) = 0, \tag{4.30}$$

$$\frac{\partial v}{\partial t} + v\frac{\partial v}{\partial r} + \frac{c_{\rm is}^2}{\rho}\frac{\partial \rho}{\partial r} + \frac{GM}{r^2} = 0, \tag{4.31}$$

$$M(r,t) = M(0,t) + \int_0^r 4\pi r'^2 \rho(r',t) dr', \tag{4.32}$$

where $M(r,t)$ represents the mass included in the radius r and $M(0,t)$ denotes the mass of the protostar. A self-similar solution which has a form

$$\rho(r,t) = \frac{\Omega(\xi)}{4\pi G(t-t_0)^2}, \tag{4.33}$$

$$v(r,t) = c_{\rm is} V(\xi), \tag{4.34}$$

$$M(r,t) = \frac{c_{\rm is}^3 |t-t_0|}{G} m(\xi) \tag{4.35}$$

$$\xi = \frac{r}{c_{rmis}|t-t_0|}, \tag{4.36}$$

should be found, where Ω and V are functions only on ξ. Since

$$\frac{\partial}{\partial t} = \frac{d}{d\xi}\frac{\partial \xi}{\partial t} = \frac{r}{c_{\rm is}|t-t_0|^2}, \tag{4.37}$$

and

$$\frac{\partial}{\partial r} = \frac{d}{d\xi}\frac{\partial \xi}{\partial r} = \frac{1}{c_{\rm is}|t-t_0|}, \tag{4.38}$$

the basic equations for the spherical symmetric model yield

$$m = (\xi - V)\xi^2 \Omega, \tag{4.39}$$

$$\left[(\xi - V)^2 - 1\right]\frac{dV}{d\xi} = \left[\Omega(\xi - V) - \frac{2}{\xi}\right](\xi - V), \tag{4.40}$$

$$\frac{(\xi - V)^2 - 1}{\Omega}\frac{d\Omega}{d\xi} = \left[\Omega - \frac{2}{\xi}(\xi - V)\right](\xi - V), \tag{4.41}$$

Equations (4.40) and (4.41) have a singular point at which $(\xi - V)^2 - 1 = 0$ or $V = \xi \pm 1$. Since the point of ξ =const moves with $c_{\rm is}$, the flow velocity relative to this ξ =const is equal to $v - c_{\rm is}\xi = (V - \xi)c_{\rm is}$. Thus the singular point ξ_* at which $V = \xi \pm 1$ corresponds to a sonic point. Therefore, since the flow has to pass the sonic point smoothly, the rhs of equations (4.40) and (4.41) have to be equal to zero at the singular point ξ_*. This gives at the sonic pont $\pm\xi_* > 0$,

$$\Omega - \frac{2(\xi - V)}{\xi} = \Omega(\xi - V) - \frac{2}{\xi} = 0, \tag{4.42}$$

which leads to

$$V_* = \xi_* \mp 1, \tag{4.43}$$

$$\Omega_* = \pm\frac{2}{\xi_*}. \tag{4.44}$$

These equations (4.39), (4.40) and (4.41) have an analytic solution

$$V(\xi) = 0, \quad \Omega = \frac{2}{\xi^2}, \quad m = 2\xi, \quad -\infty < \xi < \infty \tag{4.45}$$

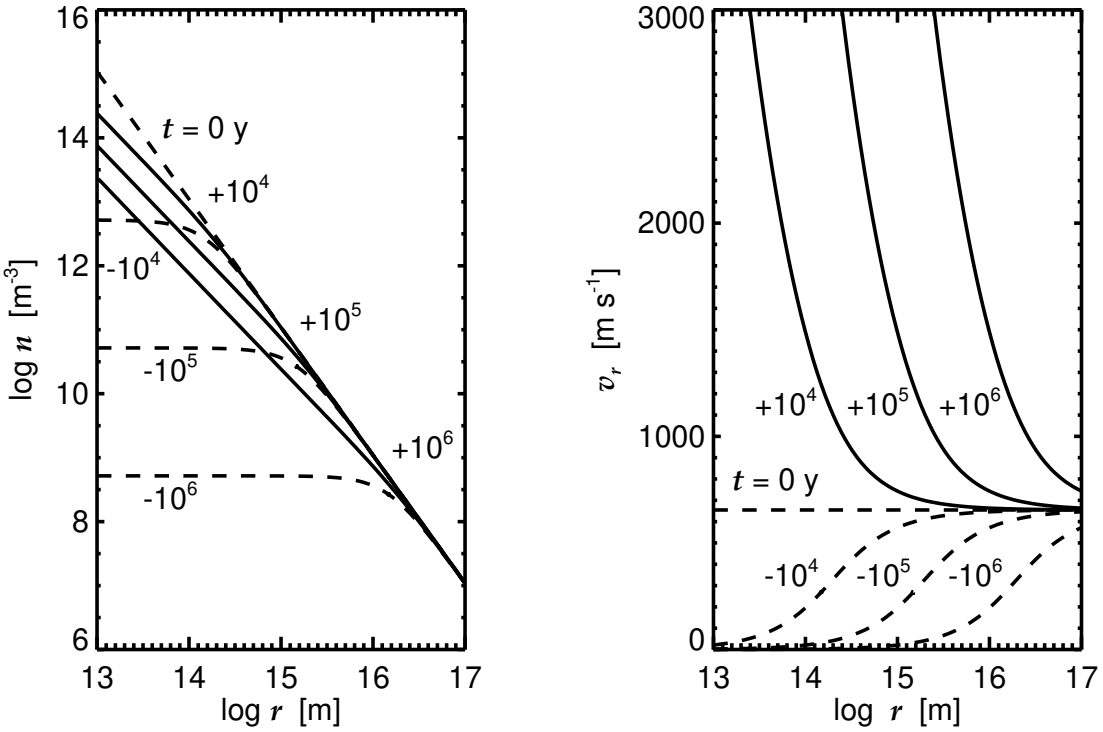

Figure 4.4: A self-similar solution indicating a dynamical collapse of isothermal spherical cloud (Larson-Penston solution). Spatial distribution of the density and inflow velocity which are expected from the self-similar solution are plotted. Dashed lines show the evolution prestellar core and solid lines show that of protostellar core. Taken from Hanawa (1999).

This is a solution which agrees with the Chandrasekhar's SIS. Generally, solutions are obtained only by numerical integration. $|\xi \to \infty|$ the solution have to converge to an asymptotic form of

$$V(\xi) = V_\infty - \frac{A-2}{\xi} + \frac{V_\infty}{\xi^2} + \frac{4V_\infty + (A-2)(A-6)}{6\xi^2} + \mathcal{O}(\xi^{-4}), \tag{4.46}$$

$$\Omega(\xi) = \frac{A}{\xi^2} - \frac{\Omega_\infty(A-2)}{2\xi^2} + \mathcal{O}(\xi^{-6}), \tag{4.47}$$

This shows that for sufficiently large radius the gas flows with a constant inflow velocity $V_\infty c_{\rm is}$.

This has a solution in which the density and the infall velocity should be regular with reaching the center ($\xi \ll 1$). Such kind of solution is plotted in Figure 4.4 (left). In Figure 4.4 (right) a time evolution is shown expected from the self-similar solution. This shows that

$$\rho \quad \begin{cases} \simeq \rho_{\rm c} & \text{(in the central region)} \\ \propto r^{-2} & \text{(in the outer envelope)} \end{cases} \tag{4.48}$$

$$v \quad \begin{cases} \propto r & \text{(in the central region)} \\ \simeq 3.28 c_{\rm is} & \text{(in the outer envelope)} \end{cases} \tag{4.49}$$

Reaching the outer boundary the numerical solution differs from the self-similar solution. For example, v is reduced to zero in the numerical simulations, while it reaches a finite value 3.28 in the self-similar

solution. And as for the density distribution, ρ drops near the outer boundary in the numerical simulations while it decreases proportional to $\propto r^{-2}$. However, in the region except for the vicinity of the outer boundary the self-similar solution expresses well the dynamical collapse of the spherical isothermal cloud. This solution gives the evolution of a pre-protostellar core formed in a supercritical cloud/cloud core.

Inside-out Collapse Solution

In 1977 Shu found another self-similar solution which is realized after a central protostar with infinitesimal mass is formed in the singular isothermal sphere solution. The gas begins to accrete to the protostar. Outside the region where the accretion occurs, the initial SIS is kept unchanged, since the SIS is a hydrostatic solution. And the front of accretion expands radially outward in time. Since the inflow region expand outwardly, he called it **the inside-out collapse solution**. In Figure **??**, the evolution is shown for density and inflow velocity. This solution gives the evolution of a protostellar core formed in a subcritical cloud/cloud core.

Using equations (4.46) and (4.47) and assuming the inflow velocity should reduce at large radius, we obtain

$$V(\xi) = -\frac{A-2}{\xi} - \frac{(A-2)(A-6)}{6\xi^3} + \cdots, \tag{4.50}$$

$$\Omega(\xi) = \frac{A}{\xi^2} - \frac{A(A-2)}{2\xi^4} + \cdots. \tag{4.51}$$

Since $\xi \to \infty$ means $t \to t_0$ (if r is finite), $\Omega(\xi) \to A/\xi^2$ means that

$$\rho(r, t_0) = \frac{Ac_{\rm is}^2}{4\pi G r^2}. \tag{4.52}$$

Comparing with the SIS, when $A = 2$ this gives the SIS and when $A > 2$ this gives a density distribution in which the pressure is inefficient and the cloud is contracting. The solution with $A > 2$ is obtained by a procedure as (1) at a sufficiently large radius ξ_1, calculate $V(\xi_1)$ and $\Omega(\xi_1)$. (2) from these values, integrate equations (4.40) and (4.41) inwardly. Figure 4.5 show the solution of this type. The solution with $A > 2$ inflow speed is accelerated towards the center. Decreasing A ($A \to 2$), it is shown that an outer part $\xi \gtrsim 1$ reaches $V \to 0$. For $A = 2^{+1}$ [1], the solution reaches the singular line $V = -\xi + 1$ at $\xi = 1$ ($V = 0$). Since $V = 0$ and $\Omega = 2$ at $\xi = 1$, this solution with $A = 2^+$ converges to the SIS at $\xi = 1$. This means that if there is an infinitesimally small amount of excess mass at the center of SIS, the accretion begins from the center while outside a radius the cloud is left static. The inner part of the solution $\xi \lesssim 1$, V and Ω are well expressed as $V \propto \xi^{1/2}$ and $\Omega \propto \xi^{3/2}$.

The power-law distributions of $V \propto \xi^{1/2}$ and $\Omega \propto \xi^{3/2}$ are explained as follows: Conservation of the total energy of an inflowing gas shell is expressed as

$$\frac{v^2}{2} - \frac{GM_r}{r} = -\frac{GM_{r_0}}{r_0}, \tag{4.53}$$

where r_0 denotes the initial radius of a gas shell and $M_{r_0} = M_r$ represents the mass inside the gas shell. Neglecting GM_{r_0}/r_0 compared with the term GM_r/r, this gives

$$v \simeq \left(\frac{2GM_r}{r}\right)^{1/2} \propto r^{-1/2}, \tag{4.54}$$

[1] This means $A = 2 + \epsilon$ and $\epsilon > 0$ and $\to 0$

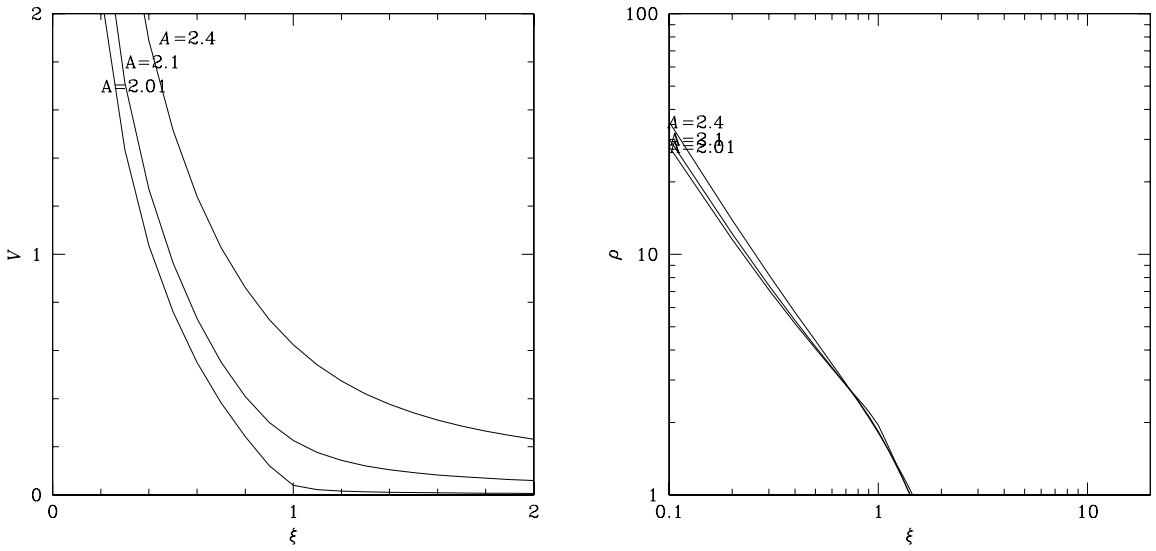

Figure 4.5: Self-similar solution which shows the inside-out collapse. (*Left*:) Infall velocity ($-V = -v/c_{\rm is}$) is plotted against the similarity variable $\xi \equiv r/c_{\rm is}(t-t_0)$. Three curves correspond to models $A = 2.4$, 2.1, and 2.01. (*Right*:) Density ($\Omega = 4\pi G\rho(t-t_0)^2$) is plotted against the similarity variable $\xi \equiv r/c_{\rm is}(t-t_0)$.

where we assumed a major part of M_r comes from the mass of a protostar M_*, that is, $M_r = M_* + \int_0^r \rho 4\pi r^2 dr \simeq M_*$ Since the average density inside the radius r $\bar{\rho}(<r) = \int_0^r \rho 4\pi r^2 dr / \int_0^r 4\pi r^2 dr = \rho(r)$, the time necessary for a gas shell to reach the center is proportional to $\propto \bar{\rho}(<r)^{-1/2} = \rho(r)^{-1/2} \propto r^1 \propto (t-t_0)^1$, where we used a fact that the front of accretion expands with a constant speed $c_s$is. This means that the time necessary for the gas shell to travel from the radius of the accretion wave front to the center is proportional to $t - t_0$. Since the mass of the shell which begins accretion in a unit time is equal to $\rho(r)4\pi r^2 c_{\rm is}$ and is constant irrespective of $t - t_0$. These two facts indicate that the mass accretion rate is constant in time. That is,

$$\dot{M} = 4\pi r^2 \rho v = \text{const.} \tag{4.55}$$

Using this equation, equation 4.54 indicates that the spatial density distribution is expressed by a power-law as

$$\rho(r) \propto r^{-3/2}, \tag{4.56}$$

which is valid for the region except for the vicinity of the front of the accretion.

4.3.2 Protostellar Evolution of Supercritical Clouds

What is a protostellar core formed in a supercritical cloud/cloud core? Is this different from the inside-out solution of Shu (1977)? A solution which corresponds to the protostellar core is obtained by Hunter (1977) and Whitworth and Summers (1985). This is a solution with $t > t_0$ in equation 4.36. The asymptotic behaviors of the density and infall velocity reaching the center are different from that of the Larson-Penston self-similar solution for a prestellar collapse. That is,

$$\Omega \quad \begin{cases} \rightarrow \text{finite} & (\text{LP}) \\ \rightarrow \text{infinite} & (\text{Inside}-\text{out}) \end{cases} \tag{4.57}$$

$$V \quad \begin{cases} \rightarrow \text{finite} & (\text{LP}) \\ \rightarrow \text{infinite} & (\text{Inside} - \text{out}) \end{cases} \tag{4.58}$$

Using the boundary conditions suitable for the inside-out type solution, another self-similar solution is obtained. In Figure 4.4 (right), such kind of solution is also plotted.

Take notice that the solutions of $t < t_0$ (prestellar) and $t > t_0$ (protostellar) agree with each other at $t = t_0$. Even if the boundary conditions at the center for the **similarity variables**, V and Ω, are completely different, the difference between the two is small in the physical variable v and ρ. Therefore, the evolution of a supercritical core is thought to be expressed by the Larson-Penston self-similar solution extended to the protostellar core phase by Hunter (1977) and Whitworth and Summers (1985).

Assume that we observe a protostellar core and obtain their density and infall velocity spatial distributions. Can we distinguish which solution is appropriate the Shu's inside-out solution or the extended Larson-Penston solution? This seems hard, because the structure of density and velocity distributions are similar after the protostar is formed: the density and velocity show almost similar power-law as $\rho \propto r^{-3/2}$ and $v \propto r^{-1/2}$ irrespective of the inside-out solution or the extended Larson-Penston solution. The region where the infall velocity is accelerated toward the center (accretion-dominated region) is expanding after the protostar is formed. Therefore, to distinguish between the two solutions becomes harder and harder after the protostar is formed. The difference would be large and we would have a definite answer which solution is appropriate to describe the cloud collapse, if we can observe a very young protostellar core or a preprotostellar core which shows dynamical collapse. However, since the timescale of such a phase is much shorter than the evolved protostellar phase or a younger preprotostellar core, the number of such kind of objects would be small ($\tau_{\rm ff} \propto \rho^{-1/2}$). Therefore, we are looking for such objects just before or after the protostar formation.

4.4 Accretion Rate

Using equation 2.26, the necessary time for a mass-shell at R to reach the center (free-fall time) is expressed as

$$T(R) \equiv \left(\frac{R^3}{2GM(R)} \right)^{1/2} \frac{\pi}{2} \tag{4.59}$$

Consider two shells whose initial radii are R and $R + \Delta R$. The time difference for these two shells to reach the center $\Delta T(R)$ can be written down using equation (4.59) as

$$\Delta T(R) = \frac{\pi R^{1/2}}{2^{3/2}(GM(R))^{1/2}} \left[\frac{3}{2} - \frac{R}{2M(R)} \frac{dM(R)}{dR} \right] \Delta R. \tag{4.60}$$

Mass in the shell between R and $R + \Delta R$, $\Delta M \equiv M(R + \Delta R) - M(R) = dM/dR \Delta R$, accretes on the central object in $\Delta T(R)$. Thus, mass accretion rate for a pressure-free cloud is expressed as $\Delta M / \Delta T$. This leads to the expression as

$$\frac{dM}{dT}(R) = \frac{2^{3/2}}{\pi} \frac{G^{1/2} M(R)^{3/2}}{R^{3/2}} \frac{\frac{R}{M(R)} \frac{dM(R)}{dR}}{\frac{3}{2} - \frac{R}{2M(R)} \frac{dM(R)}{dR}}. \tag{4.61}$$

This gives time variation of the accretion rate. Consider two clouds with the same density distribution $\partial \log \rho / \partial r$ but different absolute value. Since these two clouds have the same $\partial \log M(R) / \partial \log R$,

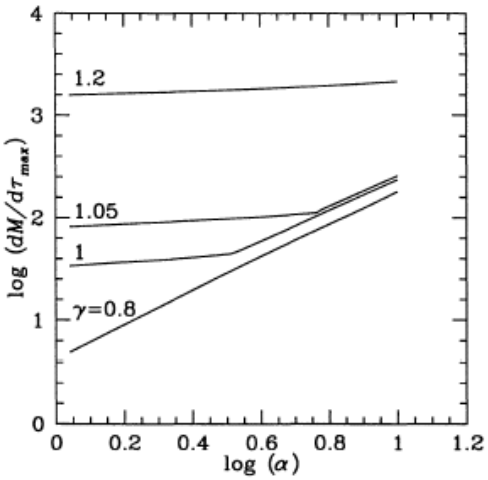

Fig. 8. Maximum of mass-accretion rate as a function of α for the models with various γ. The unit of the mass-accretion rate is taken to be c_s^3/G, which is equal to $1.6 \times 10^{-6}\, M_\odot\ \mathrm{yr}^{-1}$ for $c_s = 0.19\ \mathrm{km\ s}^{-1}$ ($T = 10$ K). The unit of time is taken to be $1/\sqrt{G\rho_{\mathrm{eq}}}$, which is equal to 6.3×10^5 yr for $\rho_{\mathrm{eq}} = 10^4\ \mathrm{cm}^{-3}$. The number attached with each line denotes the value of γ. For each line, we calculated many models with different α, i.e., $\alpha = 1.1, 1.5, 2, 2.5, \ldots, 10$.

Figure 4.6: Mass accretion rate against the typical density of the cloud.

the mass accretion rate depends only on $M(R)/R$, and is expressed as

$$\frac{dM}{dT}(R) \propto M(R)^{3/2}. \tag{4.62}$$

This indicates that the accretion rate is proportional to $\rho^{3/2}$, while the time scale is to $\rho^{-1/2}$. This is confirmed by hydrodynamical simulations of spherical symmetric isothermal clouds (Ogino et al.1999). When the initial density distribution is the SIS as $\rho \propto r^{-2}$, the mass included inside R_0 is proportional to radius $M(R) \propto R$. In this case, equation (4.61) gives a constant accretion rate in time. In Figure 4.6 we plot the mass accretion rate against the cloud density. α represents the cloud density relative to that of a hydrostatic Bonnor-Ebert sphere. This shows clearly that the mass accretion rate is proportional to $\alpha^{3/2}$ for massive clouds $\alpha > 4$. This is natural since the assumption of pressure-less is valid only for a massive cloud in which the gravity force is predominant against the pressure force.

References

[1] Alves, J., Lada, C.J., & Lada, E.A., 2001, *Internal Structure of a Cold Dark Molecular Cloud Inferred from Extinction of background Starlight*, Nature, 409, 159

[2] Alves, J., Lada, C.J., Lada, E.A., Kenyon, S.J., & Phelps, R. 1998, *Dust Extinction and Molecular Cloud Structure: L977*, ApJ, 506, 292

[3] André, P. 1994, *Observations of Protostars and Protostellar Stages* in "The Cold Universe," eds. T. Montmerle, C.J.Lada, I.F.Mirabel, & J.Tran Thanh Van, Editions Frontières, p.179

[4] Binney, J., & Tremaine, S. 1988, *Galactic Dynamics*, Princeton Univ. Pr. Chapter 6.

[5] Bonnor W. B., 1956, *Boyle's Law and gravitational instability*, MNRAS, 116, 351

[6] Ebert R., 1955, *er die Verdichtung von H I-Gebieten. Mit 5 Textabbildungen*, Z. Astrophys., 37, 217

[7] Elmegreen, B.G.; Seiden, P.E. & Elmegreen, D.M. 1989, *Spiral Arm Amplitude Variations and Pattern Speeds in the Grand Design Galaxies M51, M81, and M100*, ApJ, 343, 602

[8] Fiege, J.D., & Pudritz, R.E. 2001, *Helical fields and filamentary molecular clouds - I*, MNRAS, 311, 85

[9] Fridlund, C.V.M., & Liseau, R. 1998, it Two Jets from the Protostellar System L1551 IRS5, ApJL, 499, 75

[10] Gordon, M.A., & Burton, W.B. 1976, *Carbon monoxide in the Galaxy. I - The Radial Distribution of CO, H2, and Nucleons*, ApJ, 208, 346

[11] Hanawa, T. 1999, , *Star Formation*, in "Active Universe" in Japanese (Shokabo, Tokyo) ed. by K. Shibata, J. Fukue, R. Matsumoto, & S. Mineshige

[12] Hartmann, L. 1998, *Accretion Processes in Star Formation*, (Cambridge U.Pr.).

[13] Heithausen, A., Bensch, F., Stutzki, J., Falgarone, E., & Panis, J.F., 1998, *The IRAM key project: small-scale structure of pre-star forming regions Combined mass spectra and scaling laws*, AAp, 331, L65

[14] Hirano, N., Kameya, O., Nakayama, M., & Takakubo, K. 1988, *Bipolar outflow in B335*, ApJL, 327, L69

[15] Honma, M., Sofue, Y., & Arimoto, N. 1995, *The Molecular Front in Galaxies. II. Galactic-scale Gas Phase Transition of HI and H_2*, AAp, 304, 1

[16] Itoh, Y. et al., 2000, *A Pair of Twisted Jets of Ionized Iron from L 1551 IRS 5* PASJ, 52, 81

[17] Kennicutt, R.C. 1998, *The Global Schmidt Law in Star-forming Galaxies*, ApJ, 498, 541

[18] Kennicutt, R.C., Tamblyn, P., & Congdon, C.W. 1994, *Past and Future Star Formation in Disk Galaxies*, ApJ, 435, 22

[19] Kramer, C., Stutzki, J., Rohrig, R., & Corneliussen, U. 1998, *Clump Mass Spectra of Molecular Clouds*, AAp, 329, 249

[20] Lada, C.J., 1999, *The Formation of Low Mass Stars*, in "The Origin of Stars and Planetary Systems" ed. C.J. Lada & N.D. Kylafis, (Kluwer) p.143

[21] Loren, R. B., 1989, *The cobwebs of Ophiuchus. I - Strands of ^{13}CO - The mass distribution* , ApJ, 338, 902

[22] Mizuno, A., Onishi, T., Hayashi, M., Ohashi, N., Sunada, K., Hasegawa, T., & Fukui, Y. 1994, *Molecular Cloud Condensation as a Tracer of Low Mass Star Formation* Nature, 368, 719

[23] Mizuno, A. et al. 1995, *Overall Distribution of Dense Molecular Gas and Star Formation in the Taurus Cloud Complex*, ApJL, 445, L161

[24] Mouschovias, T. C. 1976, *Nonhomologous contraction and equilibria of self-gravitating, magnetic interstellar clouds embedded in an intercloud medium: Star formation. II - Results*, ApJ, 207, 141

[25] Motte1, F., & André, P. 2001, *The Circumstellar Environment of Low-mass Protostars: A Millimeter Continuum Mapping Survey*, AAp, 365, 440

[26] Motte, F., André, P., Ward-Thompson, D.,& Bontemps, S. 2001, *A SCUBA survey of the NGC 2068/2071 protoclusters*, AAp, 372, L41

[27] Myers, P.C. 1978, *A compilation of Interstellar Gas Properties*, ApJ, 225, 380

[28] Ogino, S., Tomisaka, K., & Nakamura, F. 1999, *Gravitational Collapse of Spherical Interstellar Clouds* PASJ, 51, 637.

[29] Ohashi, N., Hayashi, M., Ho, P.T.P., Momose, & M., Hirano, N. 1996, *Possible Infall in the Gas Disk around L1551 IRS 5*, ApJ, 466, 957

[30] Ohashi, N. Lee, S. W., Wilner, D. J. & Hayashi, M. 1999, *CS Imaging of the Starless Core L1544: an Envelope with Infall and Rotation*, ApJL, 518, L410

[31] Onishi, T., Mizuno, A., Kawamura, A., Ogawa, H., Fukui, Y. 1996, *A $C^{18}O$ Survey of Dense Cloud Cores in Taurus: Core Properties*, ApJ, 468, 815

[32] Reipurth, B., Yu, K.C., Rodríguez, L.F., Heathcote, S., & Bally, J. 1999, *Multiplicity of the HH 111 Jet Source: it Hubble Space Telescope NICMOS Images and VLA Maps*, AAp, 352, L83

[33] Schmidt, M. 1959, *The Rate of Star Formation*, ApJ, 129, 243

[34] Shu, F.H., Milione, V., & Roberts, W.W.,Jr. 1973, *Nonlinear Gaseous Density Waves and Galactic Shocks*, ApJ, 183, 819

[35] Saito, M., Sunada, K., Kawabe, R., Kitamura, Y., & Hirano, N. 1999, *he Initial Conditions for Formation of Low-Mass Stars: Kinematics and Density Structure of the Protostellar Envelope in B335*, ApJ, 518, 334

[36] Spitzer, L.Lr. 1978, *Physical Processes in the Interstellar Medium*, Wiley, Cahper 13.

[37] Stahler, S.W. 1983, *The Birthline for Low-mass Stars*, ApJ, 274, 822

[38] Stutzki, J. & Guesten, R., 1990, *High spatial resolution isotopic CO and CS observations of M17 SW - The clumpy structure of the molecular cloud core*, ApJ, 356, 513

[39] Tamura, M., Hough, J.H., Hayashi, S.S., 1995, *Millimeter Polarimetry of Young Stellar Objects: Low-Mass Protostars and T Tauri Stars*, ApJ, 448, 346

[40] Tomisaka, K., Ikeuchi, S., & Nakamura, T., 1988, *Equilibria and evolutions of magnetized, rotating, isothermal clouds. II - The extreme case: Nonrotating cloud*, ApJ, 335, 293

[41] Toomre, A. 1981, *What amplifies the spirals*, in "The structure and evolution of normal galaxies" Cambridge U.Pr., 1981, pp.111-136

[42] Ward-Thompson, D., Kirk, J.M., Crutcher, R.M., Greaves, J.S., Holland, W.S., André, P. 2000, *First Observations of the Magnetic Field Geometry in Prestellar Cores*, ApJL, 537, L135

[43] Zhou, S. 1995, *Line formation in Collapsing Cloud Cores with Rotation and Applications to B335 and IRAS 16293-2422*, ApJ, 442, 685

[44] Zhou, S., Evans, N.J.,II, Koempe, C., & Walmsley, C.M. 1993, *Evidence for Protostellar Collapse in B335*, ApJ, 404, 232

Appendix A

Basic Equation of Fluid Dynamics

A.1 What is fluid?

Gas and liquid change their shape according to the shape of the container. This is a definition of **fluid**. Stress tensor

A.2 Equation of Motion

Newton's second law of mechanics as

$$m\frac{d\mathbf{v}}{dt} = F, \tag{A.1}$$

where m, $\mathbf{v}$, and F represent the mass, the velocity of a particle and force working on the particle. In fluid dynamics, using the mass density ρ and the force working on the unit volume f equation (A.1) is rewritten as

$$\rho\frac{d\mathbf{v}}{dt} = \mathbf{f}. \tag{A.2}$$

Which kind of force works in a fluid? Gas pressure force does work in any fluids. Beside this, if there is the gravity, $\rho\mathbf{g}$ should be included in $\mathbf{f}$. If the electric currents is running in the fluid and the magnetic fields exist, the Lorentz force $\mathbf{j}\times\mathbf{B}$ should be added.

To write down the expression of the gas pressure force, consider a fluid element between x and $x + \Delta x$. Pressure force exerting on the surface S at x is $p(x)S$, while that on the opposite side is $-p(x+\Delta x)S$. The net pressure force working on the volume of $S\Delta x$ is equal to $(p(x) - p(x+\Delta x))S$, which is approximated as $-\partial p/\partial x \Delta x S + O(\Delta x^2)$. Thus, the pressure force working on the unit volume is written $-\partial p/\partial x$. Equation (A.2) can be rewritten as

$$\rho\frac{d\mathbf{v}}{dt} = -\nabla p + \rho\mathbf{g}. \tag{A.3}$$

A.3 Lagrangian and Euler Equation

The time derivative appearing in equation (A.1) expresses how the velocity of a **specific particle** changes. Therefore, that appearing in equation (A.3) is also expressing the same meaning, that is, the position of the gas element concerning in equation (A.3) moves and the positions at t and $t + \Delta t$ are generally different. However, considering the velocity field in the space, the time derivative of the velocity should be calculated staying at a point x.

These two time derivative are different each other and should be distinguished. The former time derivative is called **Lagrangian time derivative** and is expressed using d/dt. On the other hand, the latter is called **Eulerian time derivative** and is expressed using $\partial/\partial t$. These two are related with each other. Consider a function F whose independent variables are time t and position $\mathbf{x}$, that is $F(\mathbf{x}, t)$. The difference $\frac{dF}{dt}\Delta t$, using the Lagrangian time derivative of F, represents the the difference of $F(t + \Delta t)$ from $F(t)$ focusing on a specific fluid element, whose positions are different owing to its motion. The element at the position of $\mathbf{x}_0$ at the epoch t_0 moves to $\mathbf{x}_0 + \mathbf{v_0}\Delta t$ in time span of Δt. Thus the difference is expressed as

$$\begin{aligned} \frac{dF}{dt}\Delta t &= F(\mathbf{x}_0 + \mathbf{v_0}\Delta t, t_0 + \Delta t) - F(\mathbf{x}_0, t_0), \\ &\simeq \left(\frac{\partial F}{\partial \mathbf{x}}\right)_t \Big|_{\mathbf{x}_0, t_0} \cdot \mathbf{v_0}\Delta t + \left(\frac{\partial F}{\partial t}\right)_x \Big|_{\mathbf{x}_0, t_0} \Delta t, \end{aligned} \tag{A.4}$$

where we used the Taylor expansion of F. The difference regarding to the Eulerian derivative is written down as

$$\frac{\partial F}{\partial t}\Delta t = F(\mathbf{x}_0, t_0 + \Delta t) - F(\mathbf{x}_0, t_0), \tag{A.5}$$

and this is equal to the second term of the rhs of equation (A.4). Comparing equations (A.4) and (A.5), the Lagrangian derivative contains an extra term besides the Eulerian derivative. That is, the Lagrangian derivative is expressed by the Eulerian derivative as

$$\frac{d}{dt} = \frac{\partial}{\partial t} + \mathbf{v} \cdot \frac{\partial}{\partial \mathbf{x}} = \frac{\partial}{\partial t} + \mathbf{v} \cdot \mathrm{grad}. \tag{A.6}$$

Applying the above expression on equation of motion based on the Lagrangian derivative (A.3), we obtain the Eulerian equation motion:

$$\rho\left(\frac{\partial \mathbf{v}}{\partial t} + \mathbf{v} \cdot \nabla \mathbf{v}\right) = -\nabla p + \rho \mathbf{g}. \tag{A.7}$$

A.4 Continuity Equation

Another basic equation comes from the mass conservation. This is often called the continuity equation, which relates the change of the volume to its density. Consider a fluid element whose volume is equal to ΔV. The mass contained in the volume is constant. Thus

$$\frac{d\rho\Delta V}{dt} = \frac{d\rho}{dt}\Delta V + \frac{d\Delta V}{dt}\rho = 0. \tag{A.8}$$

The variation of the volume $\frac{d\Delta V}{dt}$ is rewritten as

$$\frac{d\Delta V}{dt} = \int_{\partial \Delta V} \mathbf{v} \cdot d\mathbf{S} = \int_{\Delta V} \mathrm{div}\mathbf{v} dV, \tag{A.9}$$

where $\partial \Delta V$ represents the surface of the fluid element ΔV. From equations (A.8) and (A.9), we obtain the mass continuity equation for Lagrangian time derivative as

$$\frac{d\rho}{dt} + \rho \mathrm{div}\mathbf{v} = 0. \tag{A.10}$$

Using equation (A.6) this is rewritten to Eulerian form as

$$\frac{\partial \rho}{\partial t} + \mathrm{div}(\rho \mathbf{v}) = 0. \tag{A.11}$$

Basic equations using the Lagrangian derivative are equations (A.3) and (A.10), while those of the Euler derivative are equations (A.7) and (A.11).

A.5 Energy Equation

The above basic equations (A.3) and (A.10) or equations (A.7) and (A.11) contain three dependent variables ρ, p, and $\mathbf{v}$. The number of the variables, 3, is larger than the number of equations, 2. Therefore, an extra equation is needed to close the basic equations.

A.5.1 Polytropic Relation

If the pressure of the fluid, p, is expressed only by the density, ρ,

$$p = P(\rho), \tag{A.12}$$

the number of dependent variables is reduced to two and the above equations are sufficient to describe the dynamics of the fluid. Occasionally, the presure is assumed proportional to the power of ρ as

$$p = K\rho^{\Gamma}, \tag{A.13}$$

where Γ is a constant. This assumption is called **polytropic relation**.

The fact should be reminded that the validity of the assumption comes from the physical condition of the system. In the case that the temperature of the gas is kept constant owing to the cooling and heating process, the gas pressure is proportional to the density

$$p = c_{is}^2\rho, \tag{A.14}$$

where $c_{is} = (kT/\mu m_p)^{1/2}$ (k: Boltzmann constant, μ average molecular weight, and m_p is the proton mass) represents the isothermal sound speed and is constant.

Another example is the isentropic fluid, in which the entropy is kept constant. In this case the pressure is proportional to ρ^{γ}, as

$$p = c_s^2\rho^{\gamma}, \tag{A.15}$$

where γ is the specific heat ratio $= c_p/c_v$ and $c_s = (\gamma kT/\mu m_p)^{1/2}$ represents the adiabatic sound speed and is constant. In these cases the polytropic replations of equations (A.14) and (A.15) plays a role as the third equation of basic equations of hydrodynamics.

A.5.2 Energy Equation from the First Law of Theromodynamics

In more general cases, the last equation comes from the first law of the thermal physics,

$$\Delta Q = dU + pdV. \tag{A.16}$$

where U and V represent the internal energy and the volume and ΔQ is the heat added or subtracted from the system. Using the total energy per unit volume

$$\epsilon = \frac{1}{2}\rho v^2 + \frac{U}{V} \tag{A.17}$$

the above equation gives the equation for total energy:

$$\frac{\partial \epsilon}{\partial t} + \mathrm{div}(\epsilon + p)\mathbf{v} = \rho\mathbf{v}\cdot\mathbf{g}. \tag{A.18}$$

Since the total energy per unit volume is expressed using the basic physical quantities as

$$\epsilon = \frac{1}{2}\rho v^2 + \frac{1}{\gamma - 1}p, \tag{A.19}$$

equation (A.18) is the final basic equation for hydrodynamics. Equations (A.7), (A.11), and (A.18) are basic equations hydrodynamics using the Eulerian time derivative.

A.6 Shock Wave

A.6.1 Rankine-Hugoniot Relation

Passing through a shock front moving with a speed V_s, the physical variables ρ, p, and u change abruptly. Since the basic equations of hydrodynamics is unchanged after chosing the system moving V_s, the continuity equation

$$\frac{\partial \rho}{\partial t} + \frac{\partial \rho u}{\partial x} = 0 \tag{A.20}$$

gives an equation for a steady state as

$$\frac{\partial \rho u}{\partial x} = 0, \tag{A.21}$$

from which we obtain the jump condition,

$$\rho_1 u_1 = \rho_2 u_2, \tag{A.22}$$

after we integrate over a region overlapping the shock front. Here, the quatities with suffix 1 are for preshock and those with suffix 2 are for postshock.

Equation of motion for steady state

$$\rho u \frac{\partial u}{\partial x} = -\frac{\partial p}{\partial x}, \tag{A.23}$$

gives

$$p_1 + \rho_1 u_1^2 = p_2 + \rho_2 u_2^2, \tag{A.24}$$

where we used equation(A.22).

Isotharmal shock

In the case of the gas is isothermal $p = c_{is}^2 \rho$, equation (A.24) becomes

$$\rho_1 \left(c_{is}^2 + u_1^2 \right) = \rho_2 \left(c_{is}^2 + u_2^2 \right). \tag{A.25}$$

Eliminating ρ from equations (A.22) and (A.25), we obtain

$$\left(u_1 u_2 - c_s^2 \right) (u_1 - u_2) = 0, \tag{A.26}$$

which means

$$u_1 u_2 = c_s^2. \tag{A.27}$$

From equation (A.22),

$$\frac{\rho_2}{\rho_1} = \frac{u_1}{u_2} = \frac{u_1^2}{c_s^2}. \tag{A.28}$$

This indicates the postshock velocity $u_1 \gg c_s$ the ratio of the postshock density to the preshock density becomes large.